DYNAMICS AND CONTROL OF A SMALL-SCALE MOBILE BOOM CRANE

A Thesis
Presented to
The Academic Faculty

by

Ehsan A. Maleki

In Partial Fulfillment
of the Requirements for the Degree
Master of Science in the
School of Mechanical Engineering

Georgia Institute of Technology
December, 2010

DYNAMICS AND CONTROL OF A SMALL-SCALE MOBILE BOOM CRANE

Approved by:

Dr. William Singhose, Advisor
School of Mechanical Engineering
Georgia Institute of Technology

Dr. Aldo Ferri
School of Mechanical Engineering
Georgia Institute of Technology

Dr. Mark Costello
School of Aerospace Engineering
Georgia Institute of Technology

Date Approved: June 29, 2010

ACKNOWLEDGEMENTS

I would like to thank my advisor, Dr. William Singhose, for his constant support and encouragement. His words of wisdom and contagious enthusiasm have helped me greatly. I would also like to thank my committee members, Dr. Aldo Ferri and Dr. Mark Costello for their support of this work. I would also like to thank Siemens Energy and Automation for their financial support of this thesis.

I would like to thank my parents, Flora and Hossein, for sacrificing their own lives to give me the numerous opportunities that I've had in my life. Without their love and support, I would not be where I am today. I would also like to thank my wife, Ta, for her unending love and encouragement.

Finally, I would like to thank God for giving me everything that I have.

TABLE OF CONTENTS

LIST OF TABLES

LIST OF FIGURES

SUMMARY

Cranes are a vital component of the worldwide economy. They can be seen in manufacturing plants, construction sites, shipyards, and many other material-handling and heavy-lifting applications. However, all cranes share the same limiting weakness; the payload oscillates when the crane moves. Payload oscillation not only decreases accuracy and throughput, but it can also lead to unsafe and dangerous conditions for the workers and the surrounding environment.

Boom cranes are one of the most dynamically complicated types of cranes because they possess rotational joints as opposed to the linear tracks of bridge and gantry cranes. In addition, if the boom crane is placed on a mobile base, additional complexity is added to the system. However, mobile boom cranes have huge potential benefits as they can be quickly transported from one location to another. Furthermore, if they utilize their mobile base during lifting operations, then they can have an extremely large workspace.

Although the majority of work on crane oscillation has focused on feedback control, there are fundamental problems with using feedback on cranes. A few of these include the difficulty in measuring the payload and its states, constantly varying payload dynamics, and conflict with the human operator, who also acts as a feedback controller. Given these challenges, a command-generation approach is taken to control the payload oscillation. Input shaping is one such command-generation technique that modifies the original reference command by convolving it with a series of impulses. The shaped command produced by the convolution can then move the crane without inducing payload oscillation. Input shaping can accommodate parameter uncertainties, nonlinearities, multiple modes of vibration, and has been shown to be

compatible with human operators.

This thesis focuses on three aspects of mobile boom cranes: 1) dynamic analysis, 2) input-shaping control, and 3) experimental testing. A majority of the thesis focuses on analyzing and describing the complicated dynamics of mobile boom cranes. Then, various input-shaping controllers are designed and tested, including two-mode shapers for double-pendulum dynamics.

In order to experimentally verify the simulation results, a small-scale mobile boom crane has been constructed. The details of the mobile boom crane and its important features are presented and discussed. Details of the software used to control the crane are also presented. Then, several different experimental protocols are introduced and the results presented. In addition, a set of operator performance studies that analyze human operators maneuvering the mobile boom crane through an obstacle course is presented.

CHAPTER I

INTRODUCTION

Cranes are used extensively throughout the world in a variety of applications. They are one of the primary machines used for heavy-lifting and material-handling in factories, construction sites, shipyards, etc. There are three basic types of cranes: bridge cranes, tower cranes, and boom cranes. Bridge cranes, such as the one shown in Figure 1.1, are very common in factories and shipyards. These cranes are capable of moving along two straight paths and hoisting the payload up and down, allowing them to position the payload anywhere in their workspace. When bridge cranes are mounted on a mobile platform, such as wheels, they are often called gantry cranes. When the bridge is cantilevered out over ships to unload them, they are called container cranes.

Figure 1.1: Bridge Crane

Figure 1.2: Tower Crane

Figure 1.3: Boom Crane (courtesy of Andorr Machinery)

Tower cranes, such as the one shown in Figure 1.2, are dynamically more complex than bridge cranes because they possess a rotational joint. Boom cranes like the one shown in Figure 1.3, however, are even more dynamically complicated because they possess two rotational joints. They cannot move the payload in a straight line by simply actuating one motion axis.

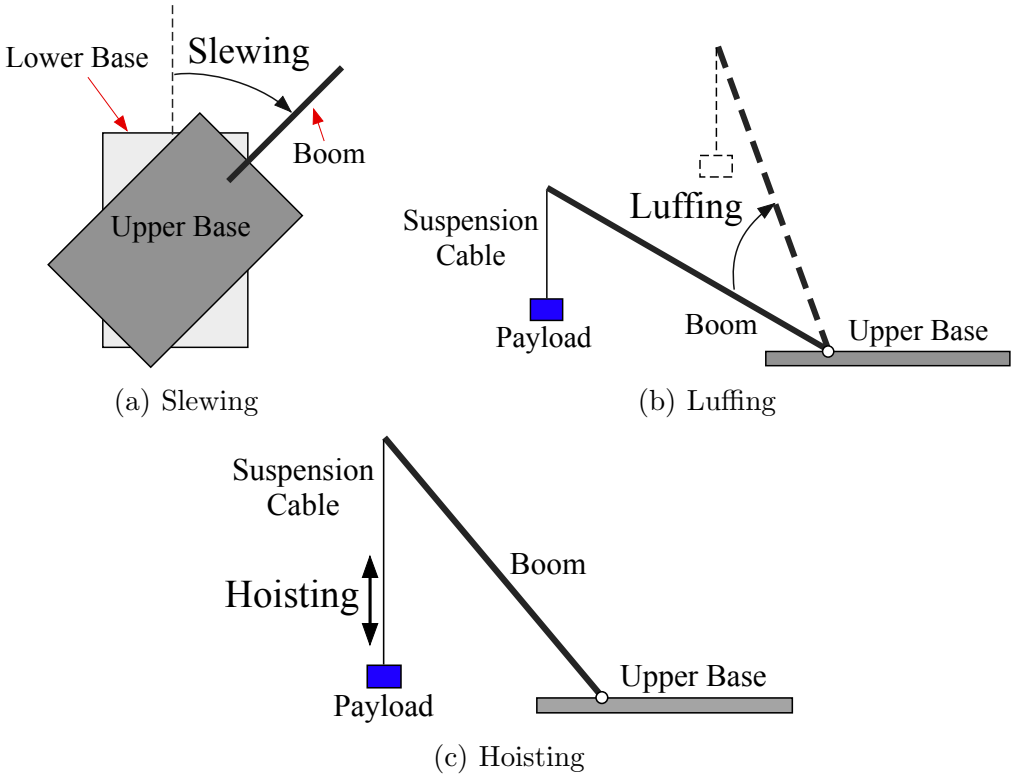

(a) Slewing

(b) Luffing

(c) Hoisting

Figure 1.4: Boom Crane Motion Axes

Boom cranes can move the payload by actuating any one of their three axes: slewing, luffing, and hoisting. Slewing is the rotation of the upper base of the crane about the lower base. This is demonstrated in Figure 1.4(a). Luffing is the rotation of the boom in a vertical plane that is perpendicular to the upper slewing base. The luffing motion is demonstrated in Figure 1.4(b). The hoisting motion is similar in all cranes where the suspension cable is hoisted up or down to move the payload upward or downward. The hoisting motion is illustrated in Figure 1.4(c).

Cranes are an integral part of every modern economy; however, the flexible nature of their physical structure degrades their effectiveness, safety, and throughput. Payload oscillation induced by both intentional motions of the crane and by external disturbances is a major limitation. These oscillations make positioning payloads and navigating cluttered workspaces very challenging.

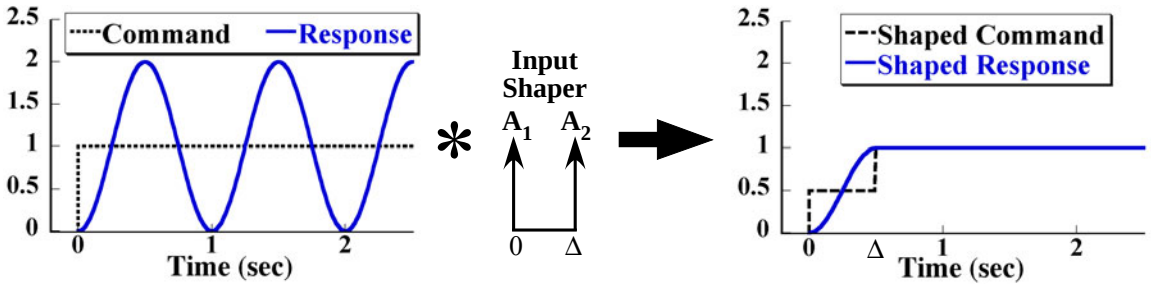

Figure 1.5: The Input-Shaping Process

Numerous researchers have proposed using feedback control to limit crane payload oscillation. Unfortunately, a fundamental conflict exists between computerized feedback control and human operators. Crane operators *are* feedback controllers; they continually adjust the input command to achieve a desired response. Any additional computer-based feedback control can conflict with the actions of the human operator. A second significant challenge of using feedback control on cranes is the difficulty of measuring the motion of the payload. For feedback to perform well, accurate measurements of the states of the payload are required. When faced with the implementation of such sensors on real machines with varying payloads, locations, disturbances, and operating environments, the sensing task can be very challenging.

On the other hand, input shaping [21,34,38,39,44,48] is a control method that is highly compatible with human operators [14,16] and can significantly reduce motion-induced oscillations. Input shaping is implemented by convolving a sequence of impulses, called the input shaper, with the desired reference command. This process is shown in Figure 1.5. The convolution is performed by simply multiplying the reference command by the amplitude of the first impulse and then adding it to the reference command multiplied by the amplitude of the second impulse and shifted in time by Δ. The original command, represented by the dotted line labeled "command," results in an oscillatory response, represented by the solid line labeled "response." The shaped command, however, eliminates the unwanted oscillatory dynamics of the response. Input shaping has been successfully applied to bridge [3, 14, 16, 27, 40, 41, 45, 47],

tower [5, 6, 17, 19, 50], boom [26, 32] and container cranes [12].

In addition to payload oscillation, lack of mobility is another limiting factor of crane performance. Most cranes have no base mobility once erected. This limits their workspace and can increase construction costs because multiple cranes must be deployed at large work sites, or one crane must be rebuilt several times at various locations. A crane that is able to move itself can provide a more effective solution. Additionally, base mobility can add crane functionality. For example, a rapidly deployable crane with a mobile base could greatly aid first responders at disaster sites or be used in de-mining operations [10]. However, the issue of safety and stability becomes more important when there is a mobile base [9, 33].

A crane with base mobility presents significant control challenges. Base motion, from ground disturbances and/or purposeful motion, will excite payload oscillation. However, there are also additional opportunities for control. The crane is redundantly actuated; multiple combinations of actuation can move the payload from one location to another. This presents the opportunity to use a combination of actuation that provides both rapid motion and low payload oscillation.

1.1 Thesis Contributions

This thesis makes significant contributions to the understanding of the complicated dynamics and input-shaping control of mobile boom cranes. The main contributions are:

1. Single-pendulum and double-pendulum dynamic models of a mobile boom crane.
2. Detailed study of the dynamics of mobile boom cranes.
3. Design, application, and verification of the effectiveness of input shaping on a highly nonlinear machine.
4. Experimental verification of important dynamic effects using a small-scale mobile boom crane.

1.2 Thesis Outline

Chapter II presents the physical structure and the user interfaces of the small-scale mobile boom crane. Then, it derives single-pendulum and double-pendulum dynamic models of the crane.

Chapter III presents two different methods for controlling the payload oscillation inherent to cranes. The work done in literature using feedback control is briefly discussed. Then, the challenges with feedback control are highlighted and an effective command-shaping method is presented.

Chapter IV studies the dynamics of the various mobile boom crane motions in detail. These include slewing, luffing, simultaneous slewing and luffing, driving, and double-pendulum dynamics. Numerical and experimental analyses are presented. The chapter concludes with an operator performance study on a small-scale mobile boom crane.

Chapter V presents a small-step control mode designed to accommodate short motions as efficiently as possible. The effectiveness of the step mode is experimentally verified.

Finally, Chapter VI provides concluding remarks and future work.

CHAPTER II

SMALL-SCALE MOBILE BOOM CRANE

This chapter presents the physical structure of the small-scale mobile boom crane used for the experiments in this thesis. Then, the user interfaces of the boom crane are presented. Finally, single and double-pendulum models of a mobile boom crane are derived.

2.1 Physical Structure

To provide a platform for research on mobile boom cranes and applications of payload-oscillation control algorithms, the small-scale mobile boom crane shown in Figure 2.1 was constructed [22–26].

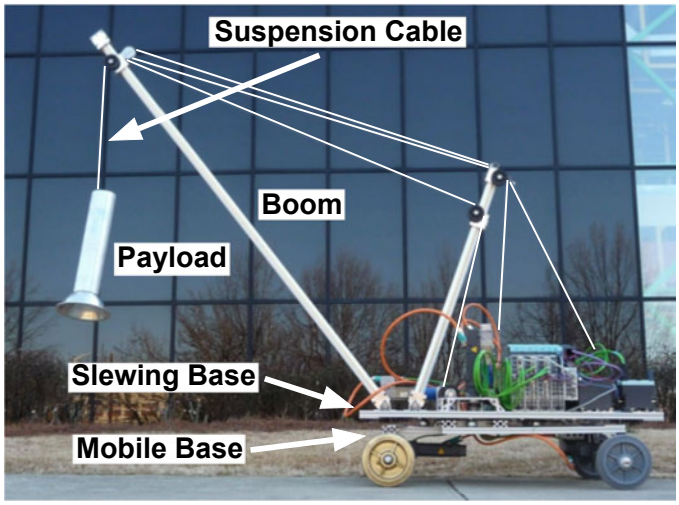

Figure 2.1: Small-Scale Mobile Boom Crane

The body of the crane is approximately 115 x 50 cm. It has two bases: the mobile base and the slewing base. Mobility of the mobile base is provided by two Siemens servomotors. The driving motor is located near the back of the crane and is connected to the back wheel axle using a timing belt and one-to-one pulleys. The steering motor

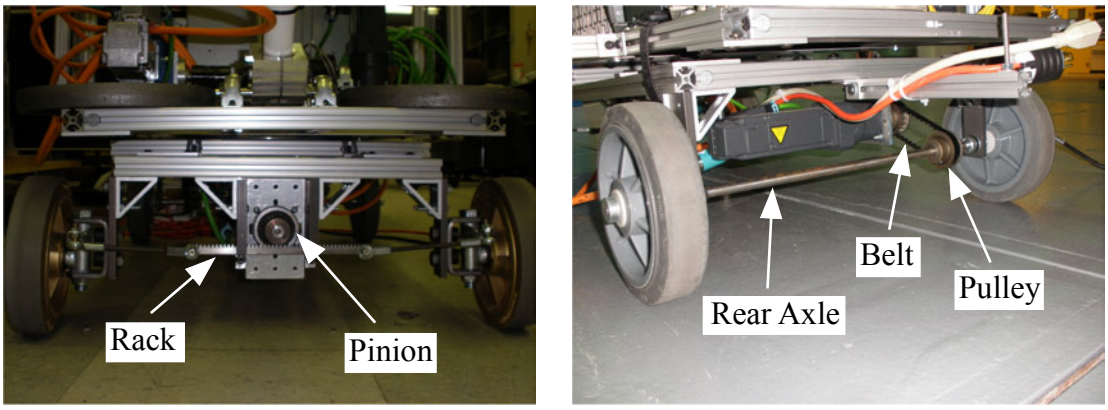

(a) Front (b) Rear

Figure 2.2: Close-up View of Mobile Base

is located near the front of the crane and controls steering via a rack-and-pinion. A close-up view of the mobile base is shown in Figure 2.2.

The slewing base can rotate with respect to the mobile base and is capable of 300° slewing rotation. The slewing rotation is supported by a turntable bearing and 4 ball transfers placed between the mobile and slewing bases. Optimizing the slewing motion was challenging for several reasons: *i)* the slewing base carries much of the heavy hardware and *ii)* the weight supported by slewing base is unevenly distributed due to spatial constraints. Two different methods were designed to improve the rotation of the slewing base. Figure 2.3(a) shows the first setup, which uses one-to-one bevel gears. Figure 2.3(b) shows the second setup, which utilizes a belt-drive system. Both setups were used in different experiments presented in this thesis.

The boom, which is attached to the top of the slewing base, is 200 cm long. The payload is moved in and out by moving the boom inward or outward, a motion called luffing. The luffing angle is controlled via a cable attached to a motor. The suspension cable length is controlled via a hoisting motor.

A Siemens SIMATIC VS732-2 digital camera is mounted at the tip of the boom and records the swing deflection of the hook. The camera is shown in Figure 2.4. The camera is connected using a four bar mechanism, which allows the camera to rotate

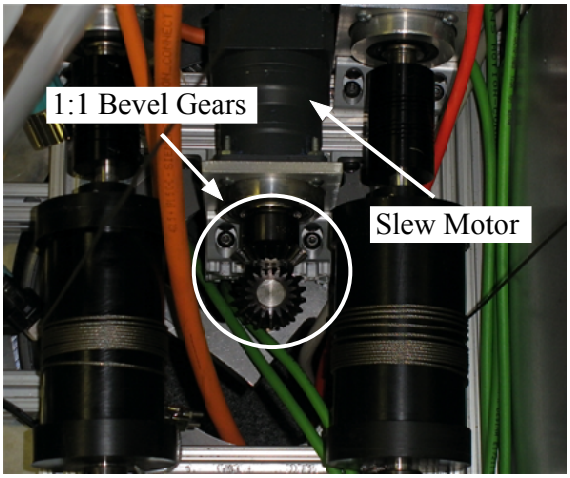

(a) Bevel Gear System

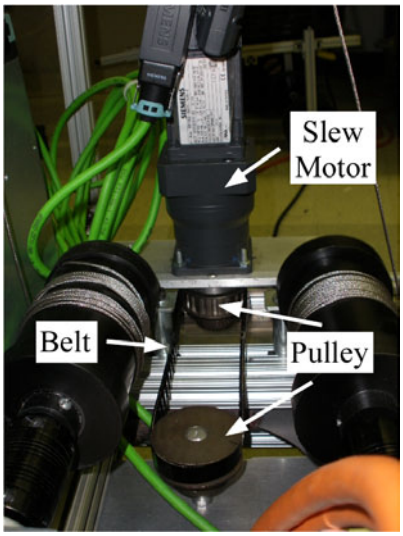

(b) Belt-Drive System

Figure 2.3: Slewing Actuation

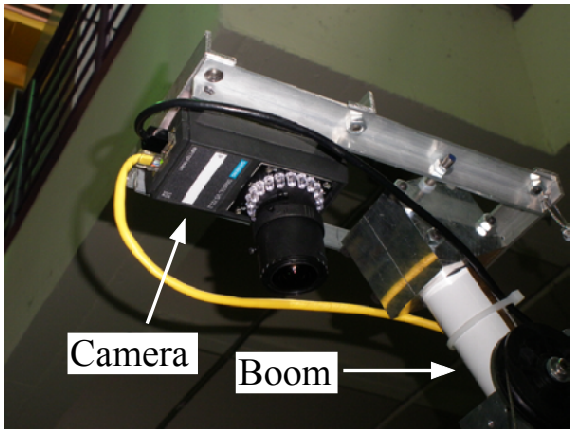

Figure 2.4: Siemens SIMATIC Camera

with respect to the boom, thereby keeping the hook in the camera field-of-view for a large range of suspension cable lengths and luffing angles. Figure 2.5 shows a sketch of the camera four-bar mechanism. If links 1 and 3 and links 2 and 4 have equal lengths, then the camera will remain parallel to the ground as the luffing angle, γ, varies.

Notice that the hook drifts horizontally across the camera field-of-view as the luffing angle and suspension cable length change. This occurs because the hook is not attached directly below the camera. There is a finite horizontal offset (δ) between

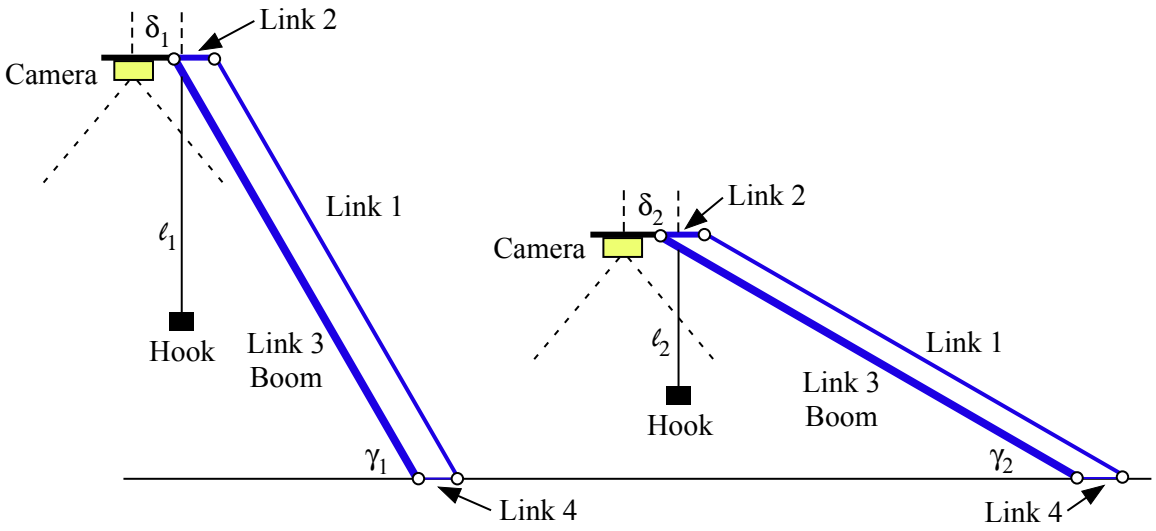

Figure 2.5: Four-bar Mechanism for Camera at Tip of Boom

them. The value of this offset increases as the luffing angle decreases. To account for the drift when obtaining the hook displacement, a lookup table was generated. The lookup table contains the no-swing hook positions (in the camera field-of-view) for various luffing angles and suspension cable lengths. The hook swing deflection at a given luffing angle and suspension cable length is found relative to its corresponding no-swing reference point from the lookup table.

All actuation of the crane is done by Siemens synchronous, AC servomotors. The motors are controlled via Siemens SINAMICS motor drives with Proportional-Integral controllers. The crane is controlled by a Programmable Logic Controller (PLC) through a wireless connection. Figure 2.6 shows a close-up of the electronic components of the boom crane.

All necessary components of the crane, such as electronics and drives, are mounted either directly on the crane or attached to an optional trailer, as shown in Figure 2.7. In Figure 2.7, the trailer is carrying the transformer box, which produces the 480V AC power supply required by the drives.

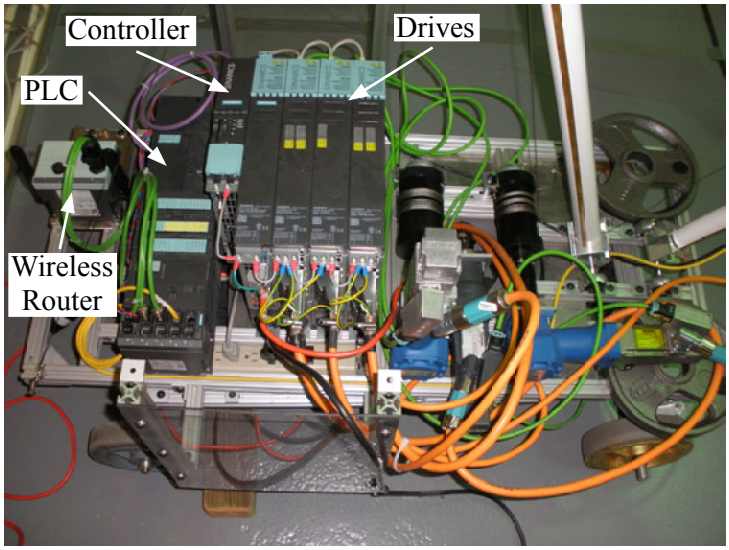

Figure 2.6: Top View of Boom Crane - Electronics

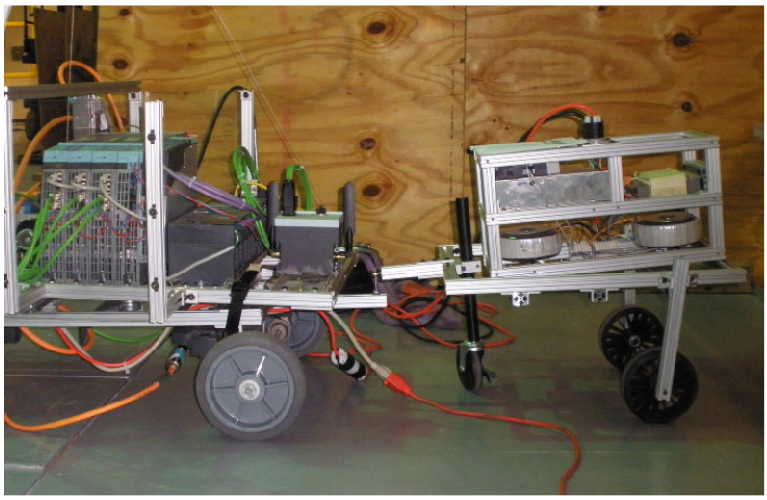

Figure 2.7: Optional Trailer

2.2 User Interfaces

Most crane controllers must be capable of controlling three independent axes, which allow the payload to be positioned anywhere in the three-dimensional workspace. A push-button pendant, shown in Figure 2.8, is a typical crane controller. The pendant has a total of six buttons that control the two directions of the three motion axes, as well as on/off and emergency stop buttons. The pendant usually hangs down below the crane, so the operator must walk with the pendant. There is not a direct physical

Figure 2.8: Push-Button Pendant

connection between a button push and the actual motion of the crane. As a result, the operator must develop a mental map between a button push and the crane motions.

A mobile boom crane adds further complexity to the crane controller as the operator must not only manipulate the crane motions, but he/she must also be able to handle driving and steering of the mobile base. This section presents two different methods of controlling the small-scale mobile boom crane: *i)* a Graphical User Interface (GUI) on a laptop, and *ii)* a Siemens touchscreen mobile panel.

2.2.1 Graphical User Interface on a Laptop

The Graphical User Interface (GUI) is shown in Figure 2.9. The GUI runs on a laptop computer. The right side of the screen contains two input fields. The top field provides buttons that move the crane motions (slewing, luffing, and hoisting) and the bottom-field buttons control the mobile base (driving and steering). The center of the screen provides the on/off button as well as numerical information about the orientation of the crane, such as the slewing angle, the luffing angle, and the suspension cable length. The left side of the screen provides a side view and a top view of the crane. The orientation of the crane in both of these views is updated in real time. The hook is also visible in the top view, and its position varies in real time as well.

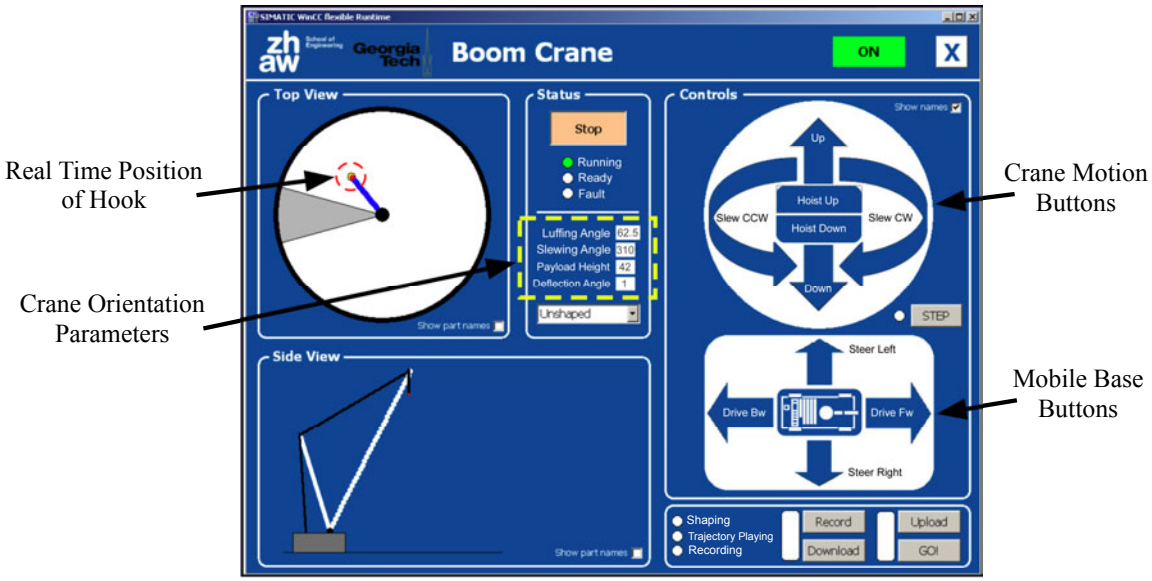

Figure 2.9: Laptop Graphical User Interface

2.2.2 Siemens Touchscreen Mobile Panel

Figure 2.10 shows the Siemens touchscreen mobile panel used for control of the mobile boom crane. The panel is a Siemens Mobile Panel 277 IWLAN. It has a 7.5 TFT-Touch display with a resolution of 640x480 pixels. It has 18 LED functions keys, two illuminated push-buttons, one hand-wheel, and one key-operated switch with three positions. The panel also has 6 MB of internal user memory and PROFINET

Figure 2.10: Siemens Touchscreen Mobile Panel

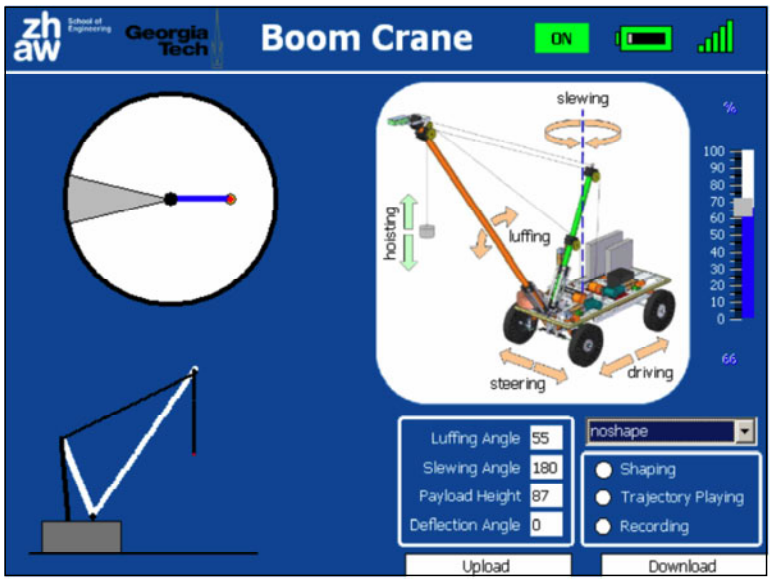

Figure 2.11: Graphical User Interface 1 on Mobile Panel

and USB interfaces. Programming the panel is performed with the Siemens WinCC Flexible software package. The mobile panel was connected to the mobile boom crane through an existing wireless router mounted on the crane.

Two different GUI's were designed for the mobile panel. The first GUI, shown in Figure 2.11, utilizes the hand wheel. The display is used to show the operator information about the mobile boom crane. On the left hand side of the screen are side and top views of the mobile boom crane. These are especially useful if the operator's view of the crane is limited. There is also an additional section that provides numerical values of important crane parameters, such as the luffing angle, the slewing angle, the suspension cable length, and the hook deflection angle.

In order to provide the operator with a better physical understanding of how each motion axis controls the crane, a three-dimensional image of the crane is provided in the top right of the screen. The motion of each axis is clearly labeled on this figure. The operator clicks on the desired axis label (for example, steering, driving, etc.) to select that axis for motion. The selected axis is highlighted to show that it is active. Once the operator has selected an axis, the hand wheel can be turned in

either direction to move the crane. For fast maneuvering, the operator can select and move more than one axis at a time. All axes selected are controlled by turning the hand wheel.

Two methods were designed to translate the hand wheel input to system motion. The first method uses the scroll bar on the right side of Figure 2.11 to select the move time associated with one click of the hand wheel. Smaller percentages equal smaller move times and are intended for small movements. Larger percentages equal longer move time and are intended for longer movements. The value of the move time is 50 ms when the scrollbar is set to 0% and 450 ms when the scrollbar is set to 100%.

The second option leaves the selection of the move time to the PLC. The PLC automatically detects whether the operator wants to do a step-by-step motion or a longer motion. The detection is carried out as a function of the system related time delays and the standard cycle time of the PLC. If the user does not carry out more than one click within a cycle time, then the program defines this as a step-by-step motion. Using this method, the operator can turn the hand wheel rapidly to move the payload close to the desired position, and then turn the hand wheel slowly to position it more precisely.

The second GUI is shown in Figure 2.12. This interface uses the function keys (F1-F10) to operate the crane. Although pushing buttons eliminates the physical connection between the interface and the actual motions of the crane, this design makes performing multi-axis motions much simpler.

For each motion axis, there are two corresponding buttons, one for each direction. Buttons for opposing directions of a motion axis are placed across from each other on the screen. The center of the display is again used to show the operator information about the orientation of the mobile boom crane.

Two different strap designs were built to hold the panel in front of the operator. These straps are shown in Figure 2.13. The major difference between the two strap

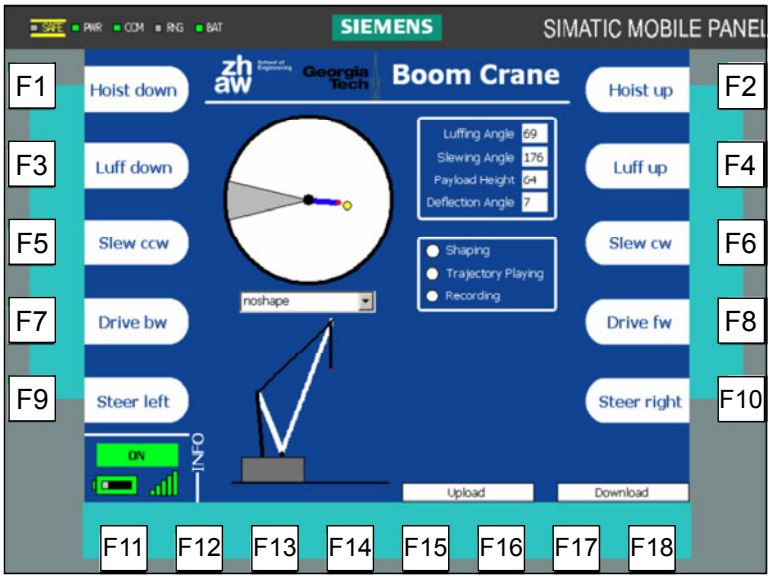

Figure 2.12: Graphical User Interface 2 on Mobile Panel

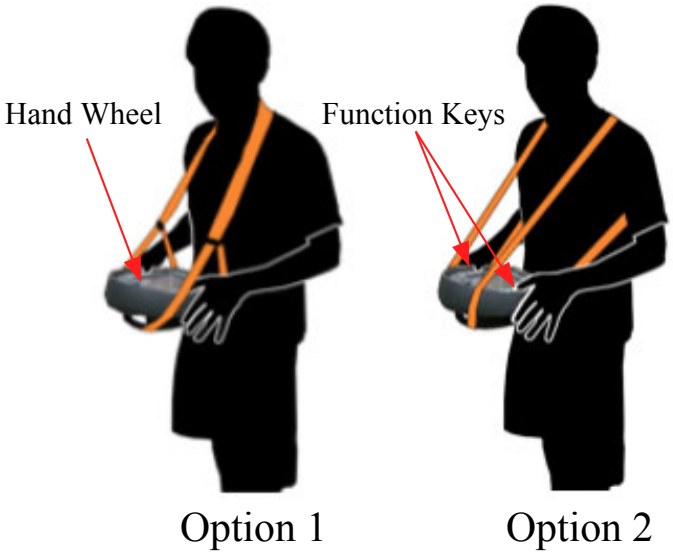

Figure 2.13: Straps for Mobile Panel

options is how the strap is attached to the mobile panel. Option one is meant to be used with GUI 1, shown in Figure 2.11, which requires the use of the hand wheel. Option two is meant to be used with the second GUI, shown in Figure 2.12, which uses the function keys on the sides of the panel.

2.3 Mobile Boom Crane Models

This section derives the equations of motion for a single and double-pendulum mobile boom crane.

2.3.1 Single-Pendulum Model

The equations of motion for a mobile boom crane were obtained using a multi-body dynamics approach. The mobile boom crane was divided into five components. The Mobile Base, the Slewing Base, and the Boom were modeled as rigid bodies with mass. The Suspension Cable was modeled as an inelastic rigid body without mass. The Hook was modeled as a point mass. Figures 2.14-2.16 show the top view, side view, and front view of the mobile boom crane model, respectively.

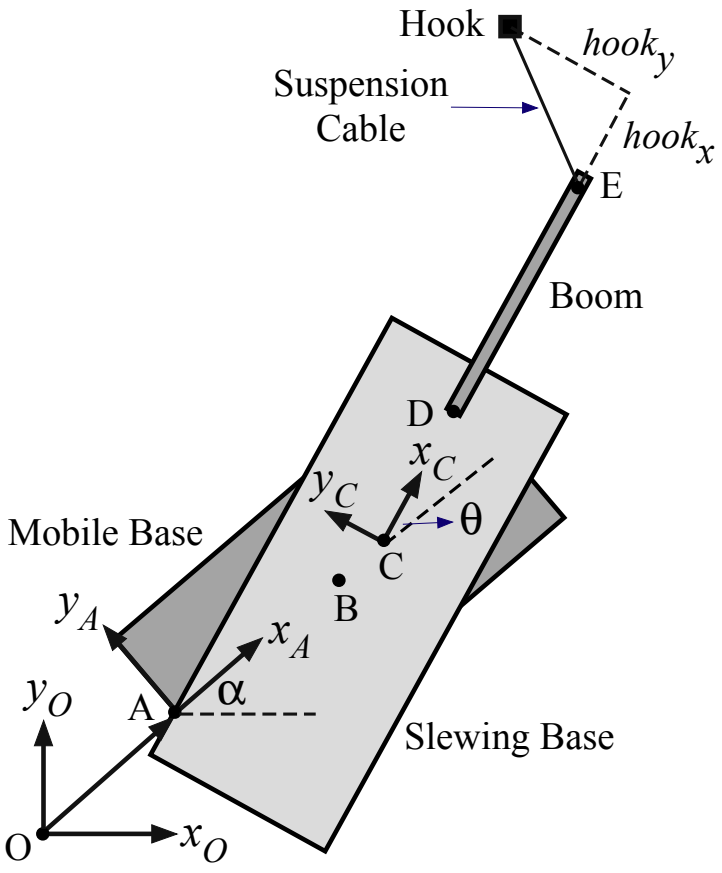

Figure 2.14: Top View of Mobile Boom Crane Model

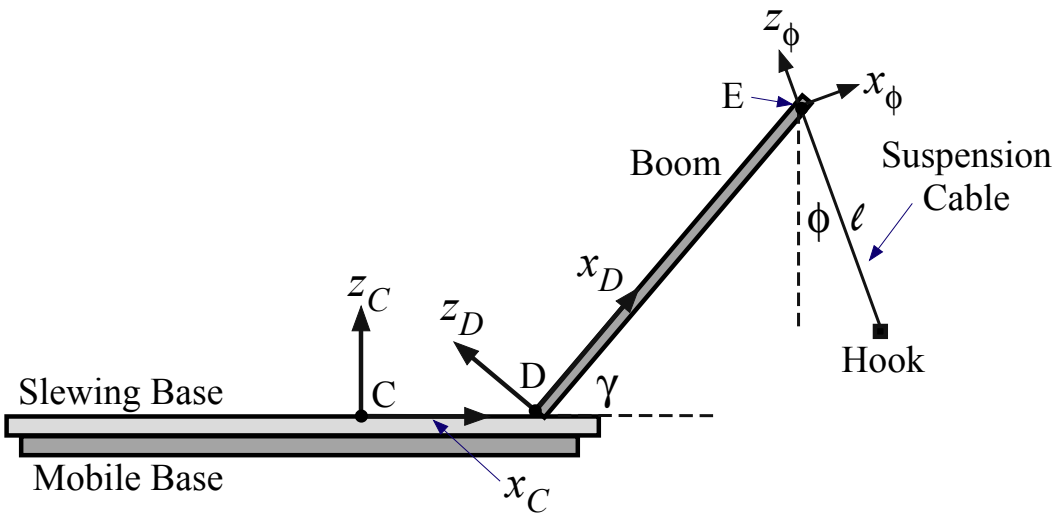

Figure 2.15: Side View of Mobile Boom Crane Model

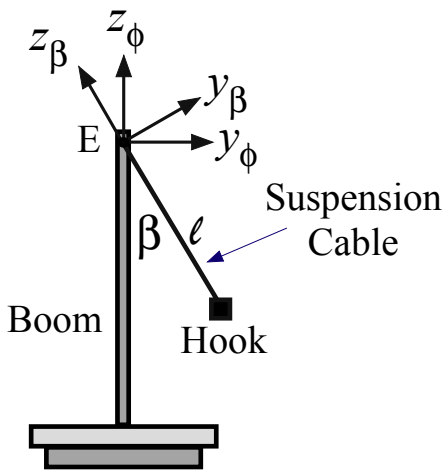

Figure 2.16: Front View of Mobile Boom Crane Model

The crane is defined with respect to an inertial, Newtonian reference frame, N, with origin at O. The center of the rear axle of the Mobile Base, point A, is located at:

$$\vec{P}_{A/O} = x\vec{x}_O + y\vec{y}_O \tag{2.1}$$

The center of the rear axle is chosen as the center of rotation of the Mobile Base because the Mobile Base is modeled as a rear-wheel drive car. The rotation of the Mobile Base about the inertial frame is given by:

$$\vec{\omega}_{MobileBase/N} = \dot{\alpha}\vec{z}_O \tag{2.2}$$

The geometric center of the Mobile Base, point B, and the slewing center of rotation, point C, are given by:

$$\vec{P}_{B/A} = x_{cent}\vec{x_A} + y_{cent}\vec{y_A} \tag{2.3}$$

$$\vec{P}_{C/B} = x_{slew}\vec{x_A} + y_{slew}\vec{y_A} \tag{2.4}$$

The Slewing Base can rotate about point C with respect to the Mobile Base with an angular velocity given by:

$$\vec{\omega}_{SlewingBase/MobileBase} = \dot{\theta}\vec{z_A} \tag{2.5}$$

The luffing center of rotation, point D, is given by:

$$\vec{P}_{D/C} = x_{luff}\vec{x_C} + y_{luff}\vec{y_C} \tag{2.6}$$

The Boom rotates about point D in a vertical plane perpendicular to the Slewing Base:

$$\vec{\omega}_{Boom/SlewingBase} = -\dot{\gamma}\vec{y_C} \tag{2.7}$$

The negative sign is to ensure that a positive luffing angular velocity will raise the Boom. The Suspension Cable attachment point, E, is given by:

$$\vec{P}_{E/D} = \ell_{boom}\vec{x_D} \tag{2.8}$$

The radial and tangential swings of the Suspension Cable are defined as:

$$\vec{\omega}_{Radial/Boom} = (-\dot{\phi} + \dot{\gamma})\vec{y_D} \tag{2.9}$$

$$\vec{\omega}_{Tangential/Radial} = \dot{\beta}\vec{x_\phi} \tag{2.10}$$

In order to define the radial swing, ϕ, with respect to reference frames that are perpendicular to the Slewing Base, the negative of the angular velocity in (2.7) is added to the radial swing. The tangential swing angle is defined relative to the radial swing angle.

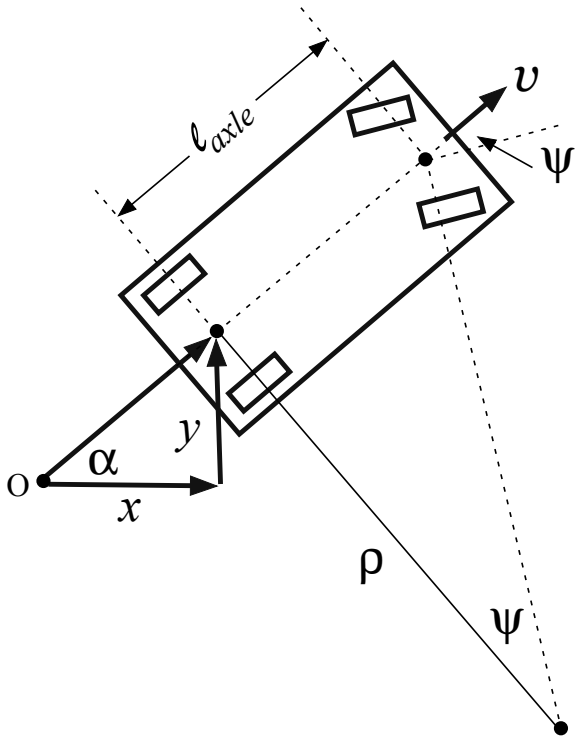

Figure 2.17: Sketch of Mobile Base Parameters

The Hook is located at the end of the Suspension Cable:

$$\vec{P}_{Hook/E} = -\ell \vec{z_\beta} \tag{2.11}$$

The displacement of the Hook relative to the overhead suspension point (in a reference frame parallel to that of the Slewing Base) is obtained by:

$$hook_x = \ell \cos(\beta) \sin(\phi) \tag{2.12}$$

$$hook_y = \ell \sin(\beta) \tag{2.13}$$

Figure 2.17 shows a sketch of the Mobile Base. It is treated as a car with rear-wheel drive and front-wheel steering. The coordinates x and y represent the location of the center of the rear axle with respect to the center of the Newtonian reference frame, ℓ_{axle} is the distance between the front and rear axle, and ρ is the radius of curvature of the arc that is traversed by the center of the rear axle, if the steering angle is constant. The inputs to the Mobile Base are the velocity of the base, v, and

the steering angle, ψ. The Cartesian components of the Mobile Base velocity, $\dot{x}$ and $\dot{y}$, as well as the Mobile Base rotation rate, $\dot{\alpha}$, are given by:

$$\dot{x} = v\cos(\alpha) \tag{2.14}$$

$$\dot{y} = v\sin(\alpha) \tag{2.15}$$

$$\dot{\alpha} = \frac{v}{\ell_{axle}}\tan(\psi) \tag{2.16}$$

The details of this derivation are given in [18].

Using a commercial dynamics package [29], the equations of motion for the mobile boom crane were obtained. The inputs to the model are the velocity of the base, v, and the accelerations for the steering angle, ψ, the slewing angle about the mobile base, θ, the luffing angle of the boom, γ, and the suspension cable length, ℓ. The important outputs are the hook swing angles in the radial direction, ϕ, and the tangential direction, β. The model assumes that the body of the crane is significantly more massive than the hook, so that the hook is unable to affect the motion of the crane base. There is no damping in the cable swing. Motor and transmission dynamics are also not modeled.

The equations of motion for the radial and tangential swings are given by:

$$\begin{aligned}
&-2\ell\cos(\beta)\ddot{\phi} = 2g\sin(\phi) + 4\dot{\ell}(\cos(\beta)\dot{\phi} - \sin(\beta)\cos(\phi)(\dot{\alpha}+\dot{\theta})) + 2\cos(\phi)\sin(\alpha+\theta)\ddot{y} + 2\cos(\phi)\cos(\alpha+\theta)\ddot{x} \\
&+ 2\ell(\sin(\beta)\sin(\phi)\dot{\phi}(\dot{\alpha}+\dot{\theta}) - \sin(\beta)\dot{\beta}\dot{\phi} - \cos(\beta)\cos(\phi)\dot{\beta}(\dot{\alpha}+\dot{\theta}) - \sin(\beta)\cos(\phi)(\ddot{\alpha}+\ddot{\theta})) - 2x_{luff}\cos(\phi)(\dot{\alpha} \\
&+ \dot{\theta})^2 - 2\ell_{boom}\cos(\gamma-\phi)(\dot{\gamma}^2 + \cos(\gamma)^2(\dot{\alpha}+\dot{\theta})^2) - 2\ell(\dot{\beta} + \sin(\phi)(\dot{\alpha}+\dot{\theta}))(\sin(\beta)\dot{\phi} + \cos(\beta)\cos(\phi)(\dot{\alpha}+\dot{\theta})) - \\
&\cos(\phi)\cos(\theta)((\ell_{axle}+2x_{slew})\dot{\alpha}^2 + 2y_{slew}\ddot{\alpha}) - \sin(\theta)\cos(\phi)(2y_{slew}\dot{\alpha}^2 - (\ell_{axle}+2x_{slew})\ddot{\alpha}) - 2\ell_{boom}\sin(\gamma \\
&- \phi)(\sin(\gamma)\cos(\gamma)(\dot{\alpha}+\dot{\theta})^2 + \ddot{\gamma})
\end{aligned} \tag{2.17}$$

$$\begin{aligned}
&2\ell\ddot{\beta} = 2\ell_{boom}\sin(\beta)\sin(\gamma-\phi)(\dot{\gamma}^2 + \cos(\gamma)^2(\dot{\alpha}+\dot{\theta})^2) + (\cos(\beta)\cos(\theta) - \sin(\beta)\sin(\phi)\sin(\theta))(2y_{slew}\dot{\alpha}^2 \\
&- (\ell_{axle}+2x_{slew})\ddot{\alpha}) + 2(\cos(\alpha)(\sin(\theta)\cos(\beta) + \sin(\beta)\sin(\phi)\cos(\theta)) + \sin(\alpha)(\cos(\beta)\cos(\theta) - \sin(\beta)\sin(\phi) \\
&\sin(\theta)))\ddot{x} + 2(\sin(\alpha)(\sin(\theta)\cos(\beta) + \sin(\beta)\sin(\phi)\cos(\theta)) - \cos(\alpha)(\cos(\beta)\cos(\theta) - \sin(\beta)\sin(\phi)\sin(\theta)))\ddot{y} + \\
&2\cos(\beta)(2\ell_{boom}\sin(\gamma)\dot{\gamma}(\dot{\alpha}+\dot{\theta}) - \ell\cos(\phi)(\dot{\alpha}+\dot{\theta})(\cos(\beta)\dot{\phi} - \sin(\beta)\cos(\phi)(\dot{\alpha}+\dot{\theta})) - \ell_{boom}\cos(\gamma)(\ddot{\alpha}+\ddot{\theta})) - \\
&2g\sin(\beta)\cos(\phi) - 4\dot{\ell}(\dot{\beta} + \sin(\phi)(\dot{\alpha}+\dot{\theta})) - 2x_{luff}\sin(\beta)\sin(\phi)(\dot{\alpha}+\dot{\theta})^2 - 2\ell\sin(\beta)\dot{\phi}(\cos(\beta)\dot{\phi} - \sin(\beta)\cos(\phi) \\
&(\dot{\alpha}+\dot{\theta})) - 2x_{luff}\cos(\beta)(\ddot{\alpha}+\ddot{\theta}) - 2\ell(\cos(\phi)\dot{\phi}(\dot{\alpha}+\dot{\theta}) + \sin(\phi)(\ddot{\alpha}+\ddot{\theta})) - 2\ell_{boom}\sin(\beta)\cos(\gamma-\phi)(\sin(\gamma) \\
&\cos(\gamma)(\dot{\alpha}+\dot{\theta})^2 + \ddot{\gamma}) - (\sin(\theta)\cos(\beta) + \sin(\beta)\sin(\phi)\cos(\theta))((\ell_{axle}+2x_{slew})\dot{\alpha}^2 + 2y_{slew}\ddot{\alpha})
\end{aligned} \tag{2.18}$$

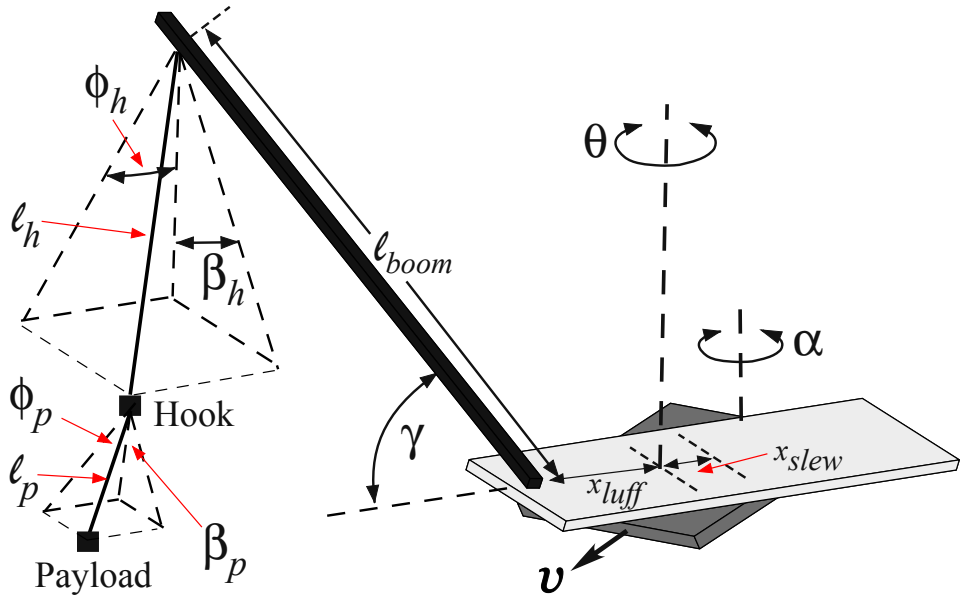

Figure 2.18: Sketch of Double-Pendulum Mobile Boom Crane Model

2.3.2 Double-Pendulum Model

To study the dynamics of the boom crane with double-pendulum payloads, the model presented above was modified to accommodate double-pendulum payloads. Figure 2.18 shows a three-dimensional sketch of the double-pendulum mobile boom crane model.

An additional Rigging Cable of length ℓ_p that attaches to the Payload and two swing angles have been added to the model. The Rigging Cable was modeled as an inelastic rigid body without mass. The Payload was modeled as a point mass. The orientation of the swing angles shown in Figure 2.18 may be somewhat difficult to discern. The Hook swing angles are clearly defined in Figures 2.15 and 2.16. The radial Payload swing, ϕ_p, is defined relative to the tangential Hook swing, β_h, and the tangential Payload swing, β_p, is defined relative to the radial Payload swing. The displacements of the Hook and the Payload relative to the overhead suspension point are given by:

$$hook_x = \ell_h \cos(\beta_h) \sin(\phi_h) \tag{2.19}$$

$$hook_y = \ell_h \sin(\beta_h) \tag{2.20}$$

$$payload_x = \ell_h \cos(\beta_h) \sin(\phi_h) + \ell_p(\cos(\phi_h) \sin(\phi_p) \cos(\beta_p) - \sin(\phi_h)(\sin(\beta_h) \sin(\beta_p) - \cos(\beta_h) \cos(\beta_p) \cos(\phi_p))) \tag{2.21}$$

$$payload_y = \ell_h \sin(\beta_h) + \ell_p(\sin(\beta_p) \cos(\beta_h) + \sin(\beta_h) \cos(\beta_p) \cos(\phi_p)) \tag{2.22}$$

The equations of motion for the double-pendulum mobile boom crane are presented in Appendix C.

CHAPTER III

FEEDBACK AND INPUT-SHAPING CONTROL

This chapter discusses two different methods for controlling oscillation of cranes. First, a brief overview of the work done in literature using feedback control is presented. Then, the challenges of feedback control are discussed. Finally, a more compatible command-generation control technique is presented and discussed.

3.1 Feedback Control on Cranes

Numerous researchers have proposed using feedback control to limit crane payload oscillation [2]. Souissi and Koivo proposed a two-tier controller for rotary cranes [46]. A PID controller was used to track the crane motions, and a PD controller was used to dampen the payload oscillation. Numerical simulation proved that the PD controller was not very effective at reducing the payload oscillation.

Henry et al. developed a delayed feedback controller for planar ship-mounted cranes [11]. Masoud et al. extended the idea to three-dimensional cranes [28]. Simulation and experiments showed significant payload oscillation reduction.

Valera et al. proposed the use of neural networks instead of PID controllers [49]. One neural network was trained (either in offline or online mode) to learn the nonlinear system behavior; another network calculated the control action. The combination of the two was shown to be effective at trajectory tracking and payload sway reduction.

Omar and Neyfeh applied two full state feedback controllers to a tower crane [31]. The controller was effective at reducing payload oscillation when the feedback gains were explicitly designed for the given system parameters. The controller effectiveness decreased for changes in the parameters.

Neupert et al. proposed a tracking and anti-sway controller for boom cranes

[30]. The anti-sway controller was composed of two disturbance observers. The tracking controller was based on model predictive control. The controller essentially solved an open-loop optimal control problem. The optimization took into account the behavior of the system with respect to the constraints. The control loop was closed by repeating the optimization process by using state measurements as initial conditions in the optimal control problem. The state measurements were obtained using two gyroscopes. Experiments on an industrial harbor mobile crane showed good tracking behavior with minimal load sway.

Although there has been success, there are several limiting factors that make implementing feedback control on cranes very challenging. One significant limitation of using feedback control on cranes is the difficulty of measuring the motion of the payload. There are two methods that have been used with some success: machine vision and gyroscopes. Machine vision systems can work well in fairly controlled environments, where lighting conditions are fairly constant and background clutter is minimal. However, most cranes operate in conditions that are significantly less ideal. Vision systems will have additional difficulties in the crowded, harsh, and changing environments in which many cranes operate.

Even under ideal conditions, sensing the payload is not trivial. One obvious place to mount a machine vision system is overhead, attached to the crane trolley. This configuration provides the best opportunity to keep the hook and payload in the camera field-of-view. However, the suspension cables and hook can limit the camera's view of the payload.

Other researchers have used gyroscope-based sensing solutions with some success [4,35,36]. In this work, the gyroscopic measurements are often coupled with secondary means of sensing, such as potentiometers measuring cable deflection, and observers are used to smooth the resulting signals. The design and implementation of such observers introduces an additional layer of complexity to the system.

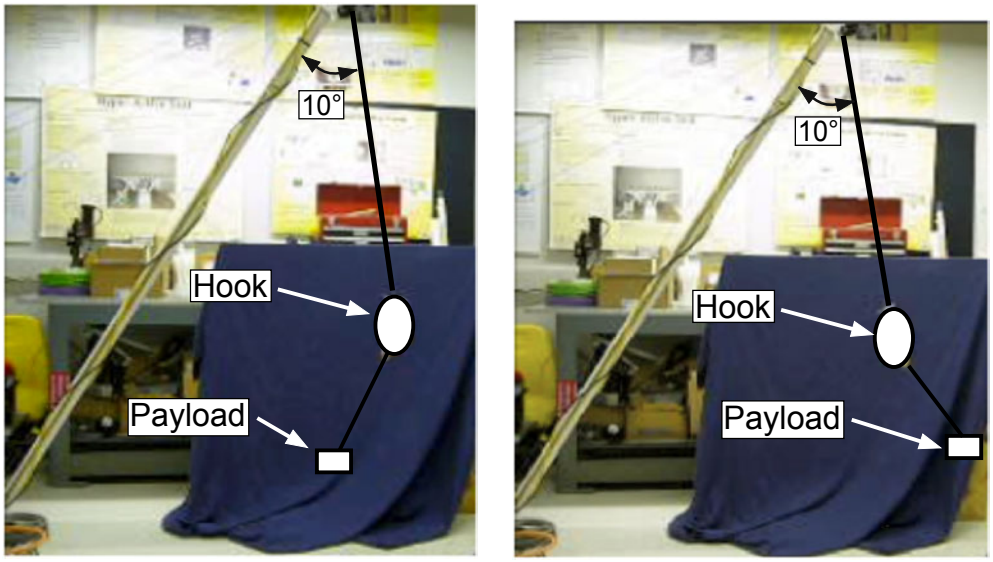

(a) Swing Angle 10°: Payload to the Left

(b) Swing Angle 10°: Payload to the Right

Figure 3.1: Varying Payload Locations at a Constant Swing Angle

Sensing the payload becomes even more challenging when there is a double-pendulum payload. Sensing both the hook and the payload is very difficult, so some feedback control methods do not measure the location of the actual payload. For example, if the hook swing angle is measured, then a feedback controller could be designed to eliminate the payload swing by driving the hook swing angle to zero. Figure 3.1 illustrates the problem with this approach when the payload creates a double-pendulum effect.

Figure 3.1(a) shows the location of the payload when the swing angle of the hook is 10°. The payload is to the left of the hook. Figure 3.1(b) shows the location of the payload for the same hook angle of 10°, but in this case, the payload is to the right of the hook. These two photographs demonstrate that measuring the suspension cable angle, or the hook location, does not provide reliable information about the payload location. Double-pendulum payloads commonly arise in many types of crane-handling processes. A feedback controller designed for single-pendulum payloads could lead to unstable results when used with double-pendulum dynamics. This is illustrated in Figure 3.2. The figure shows the disturbance responses of a small-scale

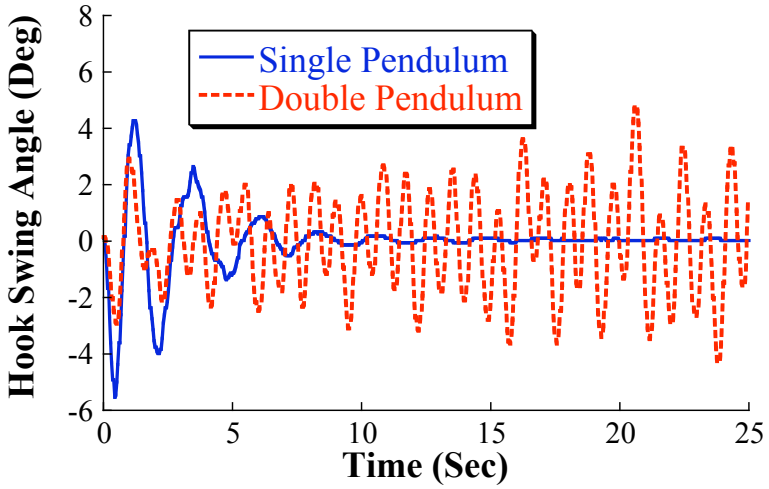

Figure 3.2: Example Instability Resulting from Double-Pendulum Dynamics

tower crane [20] for cases where the payload configuration creates single and double-pendulum dynamics. For the single pendulum, the feedback controller, using the hook swing angle as feedback, successfully eliminates the disturbance. However, when the payload creates a double-pendulum, the feedback controller drives the crane unstable.

Another major drawback of feedback control is that a fundamental conflict exists between computerized feedback control and human operators. For pre-designated or point-to-point motions, feedback control, ignoring the difficulties mentioned above, can work fairly well. However, most cranes are not controlled by a computer or driven through pre-defined trajectories. Rather, they are controlled in real time by human operators. Herein lies the conflict. The human operator provides not only the initial reference command to the crane, but also introduces adjustments and additional feedback as necessary to maneuver the crane through the desired trajectory.

3.2 Input-Shaping Control on Cranes

Input shaping [21, 34, 38, 39, 44, 48] is a command-generation control technique that modifies the reference input command to eliminate unwanted oscillatory dynamics. This modification is accomplished by convolving the reference command with a series of impulses, called the input shaper. Figure 3.3 demonstrates the input-shaping

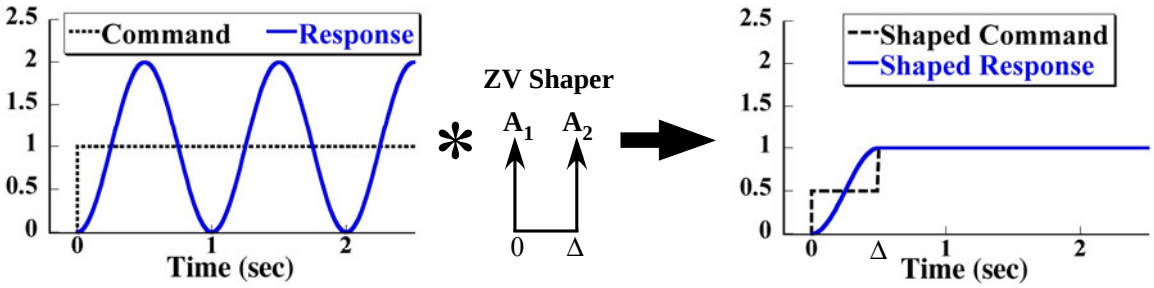

Figure 3.3: The ZV Input-Shaping Process

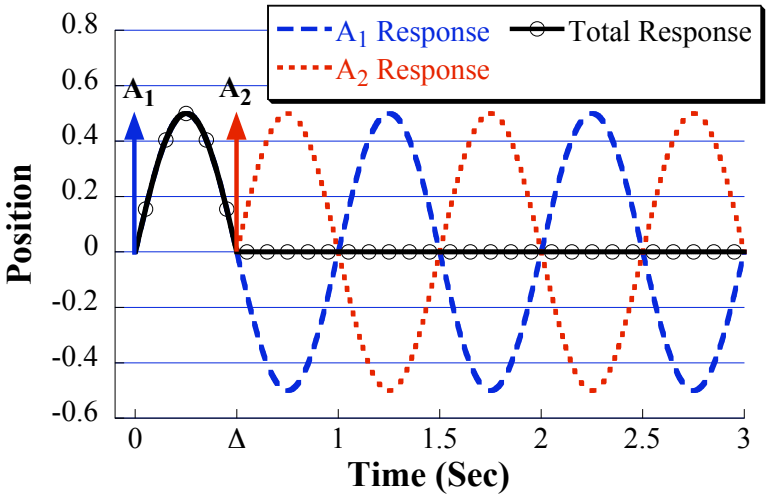

Figure 3.4: System Response to ZV Shaper

process with a two-impulse input shaper, called the Zero Vibration (ZV) shaper [38, 44]. The unshaped reference step command is convolved with the input shaper, resulting in the shaped command. The shaped command is composed of two step inputs of equal magnitude, but the second step is shifted in time. This shaped command can move the system without inducing residual oscillation.

To illustrate the input-shaping technique, Figure 3.4 shows the system response to only the ZV shaper. The magnitude of the first impulse is A_1, and the magnitude of the second impulse is A_2. Both of these impulses induce an oscillatory response. However, the sum of these two responses, which represents the total response of the system after the shaped command is complete, produces no residual oscillation. The amplitudes and times of the ZV input shaper are given by:

$$\begin{bmatrix} A_i \\ t_i \end{bmatrix} = \begin{bmatrix} \frac{1}{K+1} & \frac{K}{K+1} \\ 0 & 0.5T_d \end{bmatrix} \tag{3.1}$$

Where T_d is the damped period of vibration and K is given by:

$$K = e^{\left(\frac{-\zeta\pi}{\sqrt{1-\zeta^2}}\right)} \tag{3.2}$$

The ZV shaper is designed to produce zero residual vibration at the modeled frequency. If the actual natural frequency of the system is the same as the modeled frequency, then the residual vibration will be greatly reduced. In real machines; however, the exact value of the natural frequency is difficult to obtain. Only an estimate of the natural frequency is known. Therefore, it is important to design shapers that are robust to errors or variations in the system parameters. The ZV shaper is not very robust to parameter variation, but there exist many shapers that are robust, such as the Zero Vibration and Derivative (ZVD) shaper [38] and the Extra Insensitive (EI) shaper [42]. The fundamental idea behind all input shapers is similar to that of the ZV shaper; however, by adding additional impulses (at appropriate times), the robustness of the shaper to modeling errors can be increased. Figure 3.5 shows the sensitivity curves for the three input shapers mentioned above. The horizontal axis is the system natural frequency, ω, normalized by the modeled frequency, ω_m. The vertical axis is the percentage residual vibration. A percentage vibration of 100% means that the shaped command will produce the same amount of residual vibration as the unshaped command.

With increased robustness, however, comes increased time penalty. More robust shapers have longer durations. Specified Insensitivity (SI) shapers [40,43] provide the maximum amount of robustness for a given shaper duration. Specified Insensitivity shapers are designed by generating constraints that limit the residual vibration to a tolerable value, V_{tol}, over a range of frequencies. Figure 3.6 illustrates this design

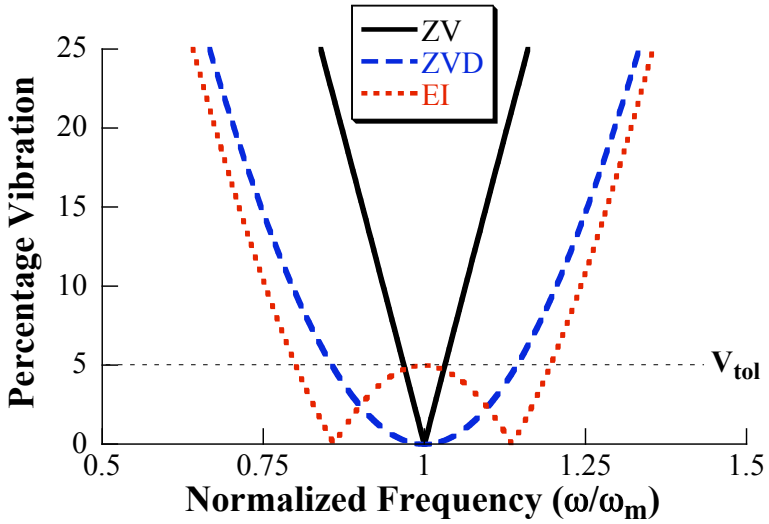

Figure 3.5: Sensitivity Curves for Various Shapers

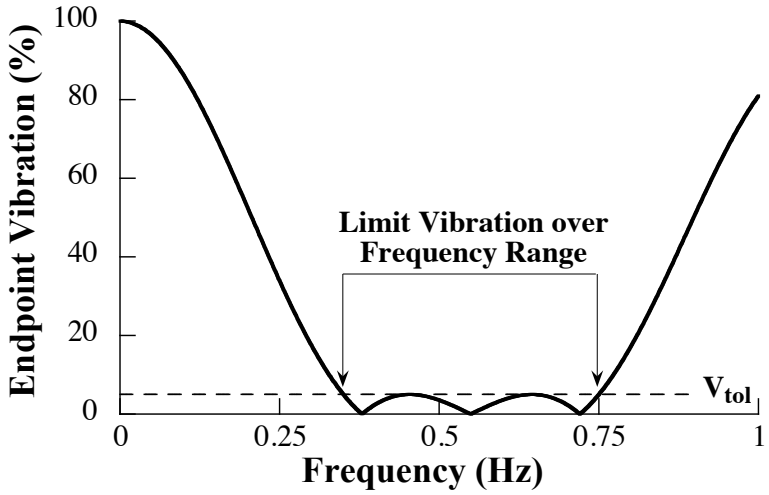

Figure 3.6: One-Mode SI Shaper Design Process

process. Then, an optimization routine can be used to solve for the amplitudes and times of the input-shaper impulses that achieve the desired vibration suppression.

Often, adding a payload to the crane hook will produce double-pendulum dynamics [16, 17, 40]. Double-pendulum payloads represent an important subset of crane applications where the hook and payload create a two-mode oscillatory system. Input shapers can easily suppress additional modes of oscillation. A two-mode SI shaper [40] is one such shaper that can account for multiple oscillation modes and is robust to parameter variations. The design process of the two-mode SI shaper is similar to the

one-mode SI shaper design process; however, instead of one, two frequency ranges are selected. Then, numerical optimization is performed to obtain the shaper parameters that meet the oscillation constraint requirements.

CHAPTER IV

BOOM-CRANE DYNAMICS AND INPUT-SHAPING CONTROL

In this chapter, the dynamics of the mobile boom crane motions are investigated through simulation and experiment. Input shaping is also applied to these motions and its effectiveness is quantified.

The baseline reference command used in this investigation is a trapezoidal-velocity profile (bang-coast-bang acceleration), as shown in Figure 4.1(a). For small motions, the trapezoid reduces to a triangular velocity, as shown in 4.1(b). The transient stage of the response is defined as the time frame from the beginning of the accelerating pulse to the end of the decelerating pulse. The residual stage is defined as the time frame from the end of the decelerating pulse to the end of the simulation.

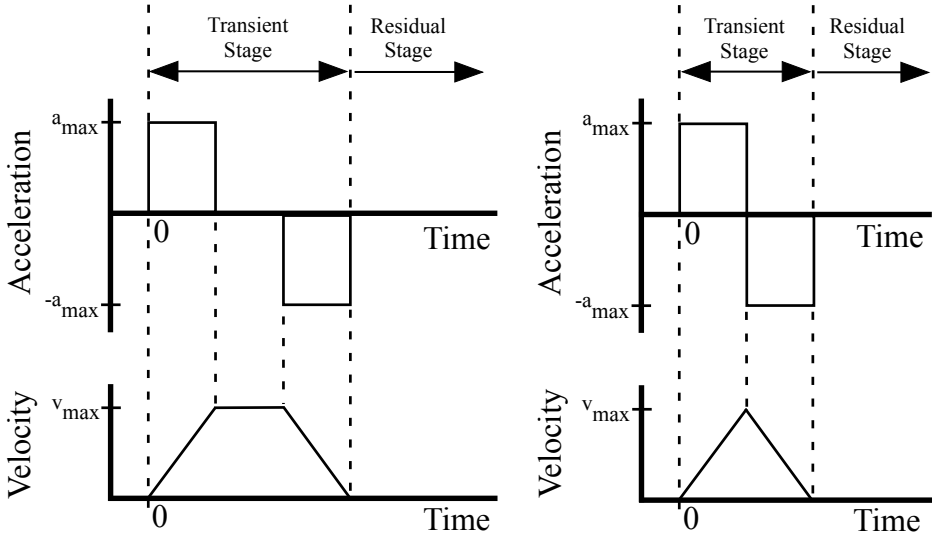

(a) Bang-Coast-Bang Command (b) Bang-Bang Command

Figure 4.1: Bang-Coast-Bang and Bang-Bang Commands

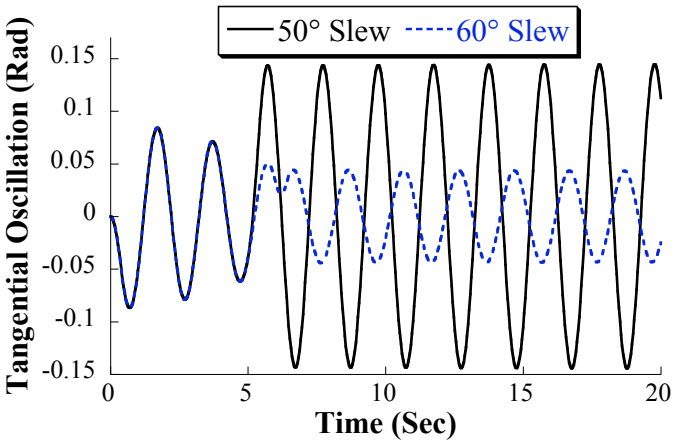

Figure 4.2: Tangential Payload Oscillation for Slewing Distances of 50° and 60°

4.1 Single-Pendulum Dynamics

This section analyzes the single-pendulum dynamics of various mobile boom crane motions. In this analysis, two important oscillation parameters are measured and discussed: transient deflection and residual vibration amplitude. Transient deflection is the average payload displacement relative to the overhead suspension point during the motion (transient stage). Residual vibration amplitude is the maximum payload displacement relative to the overhead suspension point after the completion of the motion (residual stage).

4.1.1 Slewing

Slewing motion of the boom crane is defined as the rotation, θ, of the slewing base about the mobile base. During numerical simulation of the boom crane, the maximum slewing velocity is limited to $10°/s$ and the maximum acceleration is limited to $25°/s^2$.

The solid line in Figure 4.2 shows the tangential swing of the payload during a 50° slewing motion. The luffing angle was held constant at 45°, and a constant suspension cable length of 1 m was used. The starting acceleration at 0 s initiates some oscillation. At approximately 5 s, the stopping deceleration induces more oscillation. In this case, the oscillation induced by stopping the slew is in phase with the swing

caused by the initial acceleration. Hence, the residual vibration amplitude is larger than the transient. For some cases, however, the stopping oscillation is out of phase with the starting oscillation and results in reduced residual vibration amplitude. This is demonstrated by the dotted line in Figure 4.2, which shows the tangential swing for a slewing distance of 60°. The stopping deceleration, which occurs at approximately 6 s, partially cancels out the oscillation caused by the starting acceleration, thus resulting in smaller residual oscillation.

The tangential and centripetal forces of the slewing motion cause the payload to oscillate in two directions, radial and tangential. This can be traced to coupling terms between the slewing motion and the radial and tangential swing angles, ϕ and β, in the equations of motion. During the slewing motion (transient stage), the frequencies of oscillation in the radial and tangential directions are slightly different [19]. This leads to beating between the two oscillations. This is demonstrated in Figure 4.3, which shows the radial and tangential oscillations for a 360° slewing motion that takes 36 s to complete. Using an FFT analysis, the two frequencies of oscillation were obtained as 0.47 Hz and 0.53 Hz. (The oscillation frequency of a simple pendulum with a 1 m suspension cable length is 0.50 Hz). The results of the FFT are shown in Figure 4.4.

Another result of the rotational slewing motion is the precession of the payload. To better demonstrate this effect, the dynamics were simulated for a duration of 1500 s. Figure 4.5 shows the radial and tangential oscillations for a 10° slewing motion, which is completed in 1.4 s. The maximum residual radial oscillation occurs when the residual tangential oscillation is near its minimum, and vice versa. This effect can be physically interpreted as the oscillation of the payload precessing from one direction to the other. Figure 4.6 shows the location of the payload relative to the suspension point for the 10° slew shown in Figure 4.5. The payload does not follow a single loop; it oscillates between the radial and tangential directions.

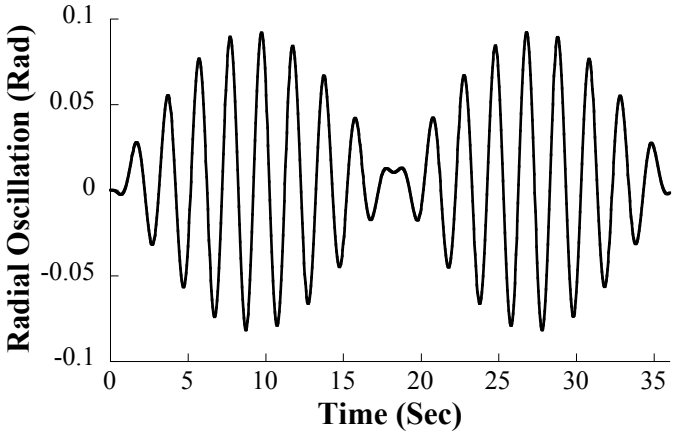

(a) Radial Oscillation

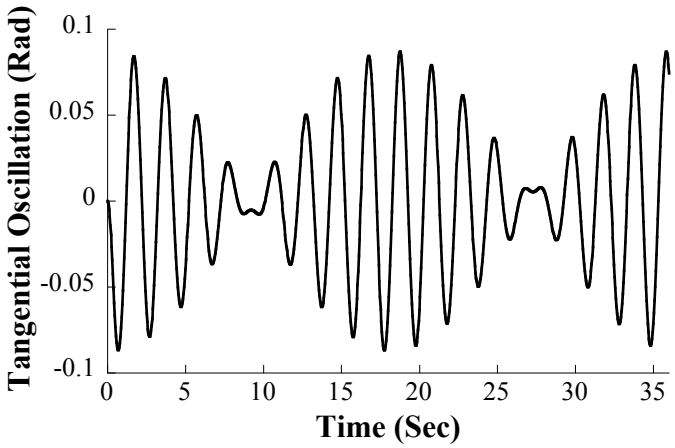

(b) Tangential Oscillation

Figure 4.3: Payload Oscillation During a 360° Slew

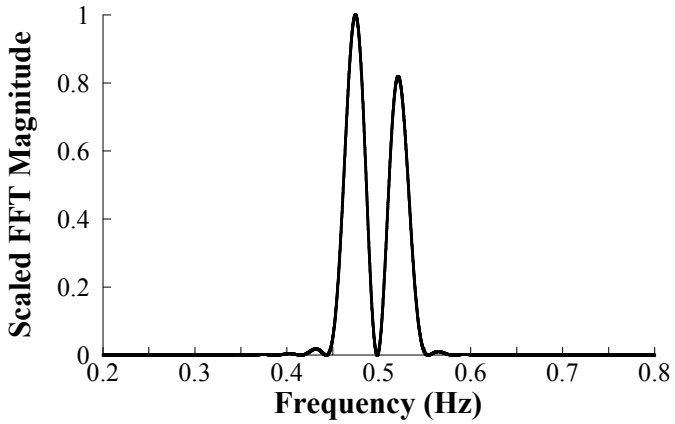

Figure 4.4: FFT Analysis of the Radial Swing for a 360° Slew

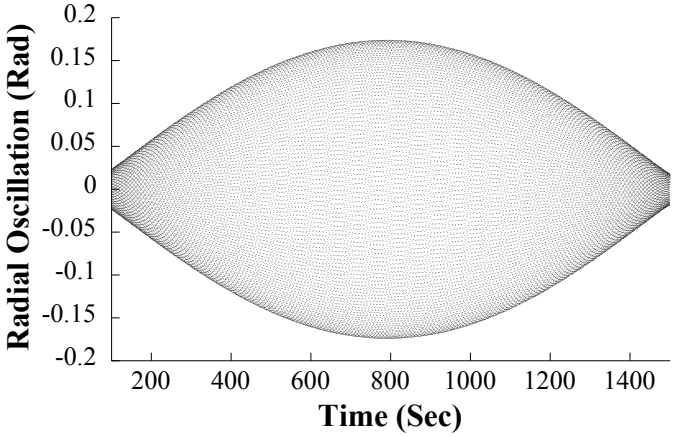

(a) Radial Oscillation

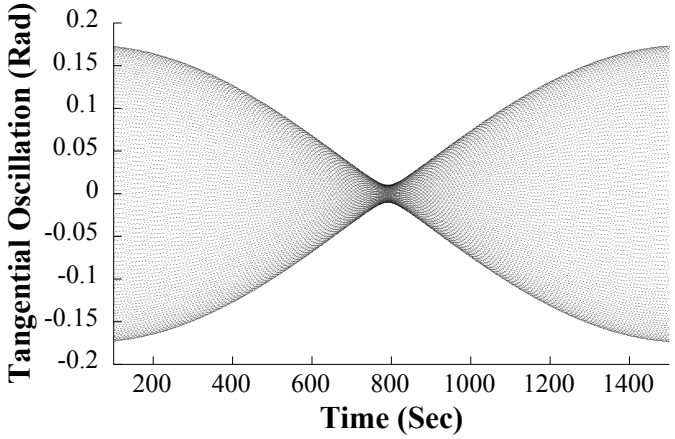

(b) Tangential Oscillation

Figure 4.5: Payload Oscillation Resulting from a 10° Slew

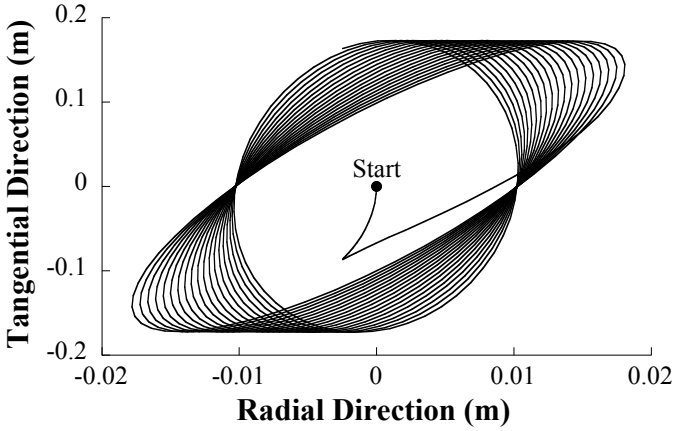

Figure 4.6: Payload Response from a 10° Slew

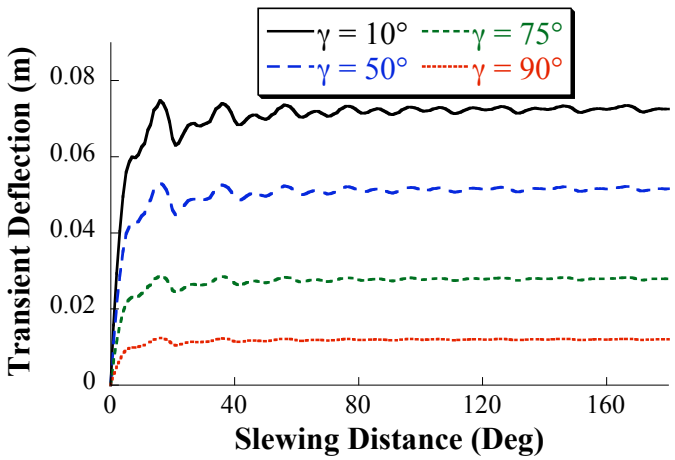

Figure 4.7: Transient Deflection vs. Slewing Distance

To better understand the dynamics of the slewing motion, the relationship between transient deflection, residual vibration amplitude, slewing distance, and luff angle were investigated. The crane was started from rest at the 0° slew position (with the boom pointing directly forward). Then, it was slewed with a constant luff angle. Figure 4.7 shows how the average transient deflection changes as a function of slewing distance.

The amount of transient deflection depends on the size of the acceleration pulse and the duration of the transient stage. For small slewing distances, the width of the acceleration pulse increases with slew distance. However, once the slew distance is large enough, the maximum velocity is reached and the maximum acceleration pulse for the bang-coast-bang command occurs. After this point, the transient deflection is no longer dependent on the acceleration pulse size, but varies as the slewing distance (the transient duration) is increased. This variation is due to the interference between the starting and stopping oscillations during the transient stage (more specifically, during the deceleration pulse of the bang-coast-bang command). As the slewing distance becomes large, however, the starting oscillation comprises a larger portion of the transient stage than the oscillation resulting from the interference between the starting and stopping oscillations. As a result, the average transient deflection levels

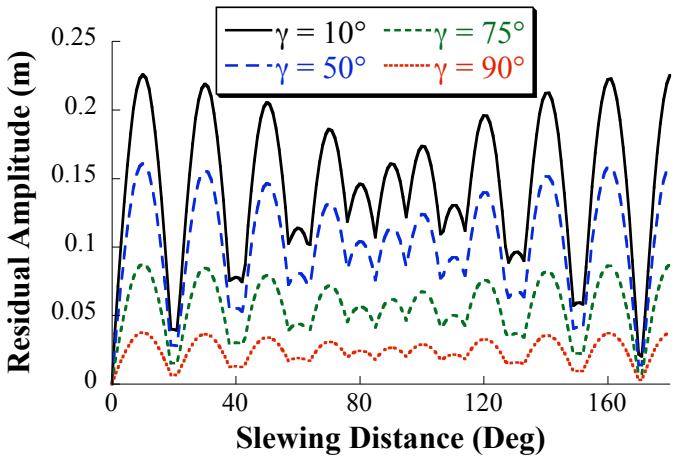

Figure 4.8: Residual Vibration Amplitude vs. Slewing Distance

out.

The relationship between residual vibration amplitude and slewing distance is complex, as shown in Figure 4.8. After a 90° slew, the radial and tangential directions have exactly switched. As a result, the residual vibration amplitude is almost symmetrical about a slewing distance of 90°.

There are numerous peaks and troughs in the residual amplitude curves as the slewing distance varies. Although the slewing motion is nonlinear, the trends in the peaks and troughs can be explained by using a simple, linear second-order model. Assume that the input to such a system is two pulses in acceleration that form a bang-coast-bang command. Both acceleration pulses have the same magnitude, so they induce the same amount of oscillation. For a linear model, the magnitude of oscillation caused by each pulse is equal in magnitude and sometimes in phase and sometimes out of phase with each other. The amplitude of residual vibration will then contain peaks and troughs as it is plotted versus the move distance. In the nonlinear slewing motion, however, the oscillations produced by the acceleration and deceleration are not quite equal in magnitude. The peaks in residual vibration amplitude arise when the responses from these two pulses are in phase and add up to produce more swing. The troughs occur when the two responses are out of phase

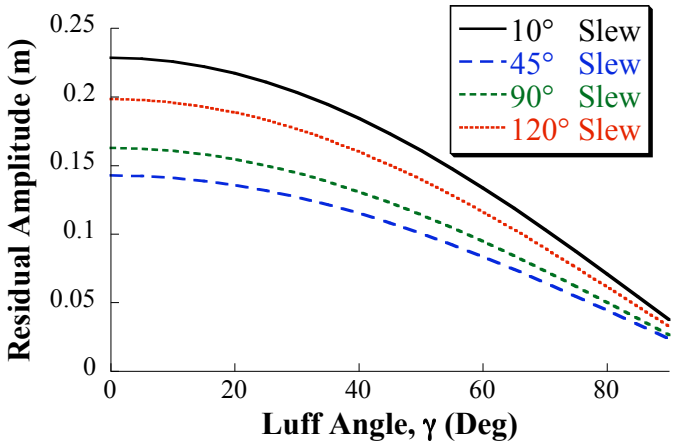

Figure 4.9: Residual Vibration Amplitude vs. Luff Angle

and partially cancel each other, resulting in low residual swing. These two scenarios were demonstrated in Figure 4.2. Figure 4.8 shows how these two scenarios alternate with slewing distance.

The relationships between transient deflection and luffing angle and between residual vibration amplitude and luffing angle are similar. Figure 4.9 shows how the residual vibration amplitude changes as a function of the luff angle. As the luff angle decreases, the end of the boom extends farther away from the base, and the residual vibration amplitude increases. When the payload is farther from the rotating base, it travels faster and covers a longer distance for a given slewing motion. The higher velocity requires higher tangential and centripetal forces; these cause more swing. This relationship, however, is not linear. When the boom is pointing straight up, with a luff angle of 90°, the oscillation is at its smallest; however, it is not zero. This is because the center of slewing and luffing are a finite distance, x_{luff}, apart. Hence, there is a small amount of oscillation even when the boom is straight up, and the base slews.

An iterative simulation routine was performed to find the residual vibration amplitude for a wide range of all possible slewing commands. The slewing motion was simulated for distances between 0° and 180°, using constant luffing angles between 0°

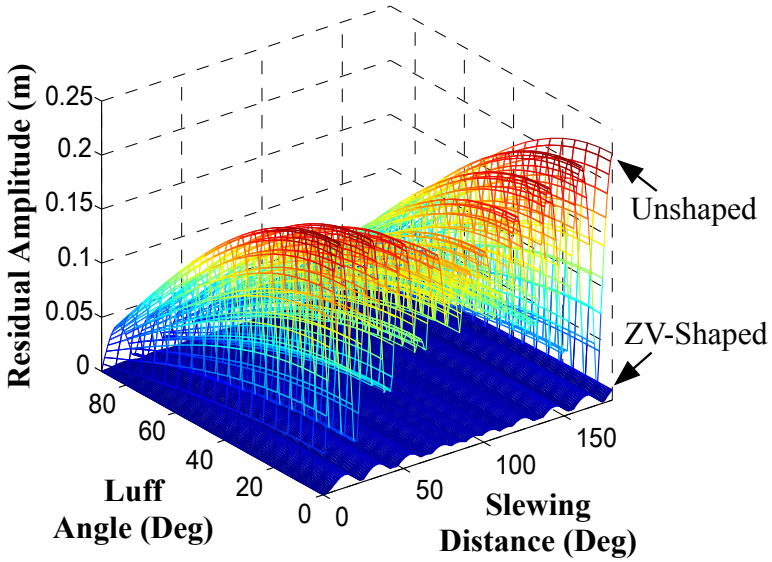

Figure 4.10: Slewing Residual Vibration Amplitude

and 90°. The suspension cable length was kept constant at 1 m. Figure 4.10 shows the residual vibration amplitude as a function of slewing distance and luffing angle. The complex dynamics discussed in Figures 4.8 and 4.9 are present in this figure.

To investigate the effectiveness of input shaping on controlling the oscillation induced by the slewing motion, the same maneuvers were repeated, but the reference commands were convolved with a two-impulse Zero Vibration (ZV) input shaper [38, 44]. The solid surface in Figure 4.10 shows the residual vibration amplitude induced by ZV-shaped commands. Figure 4.10 demonstrates the effectiveness of input shaping on this nonlinear slewing motion. The residual vibration amplitude was reduced for every slewing distance and luff angle. Over the entire space shown in Figure 4.10, input shaping reduced residual vibration by an average of 95%.

It is also of interest to analyze the transient deflection of the system during the motion. Figure 4.11 shows the unshaped and ZV-shaped average transient deflections. Note that cutting through the surface in Figure 4.11 along a line of constant luff angle would yield a curve similar to those shown in Figure 4.7. The shaped transient deflection is lower than the unshaped transient deflection by an average of 78%.

The velocity and acceleration limits used in these simulations are relatively low.

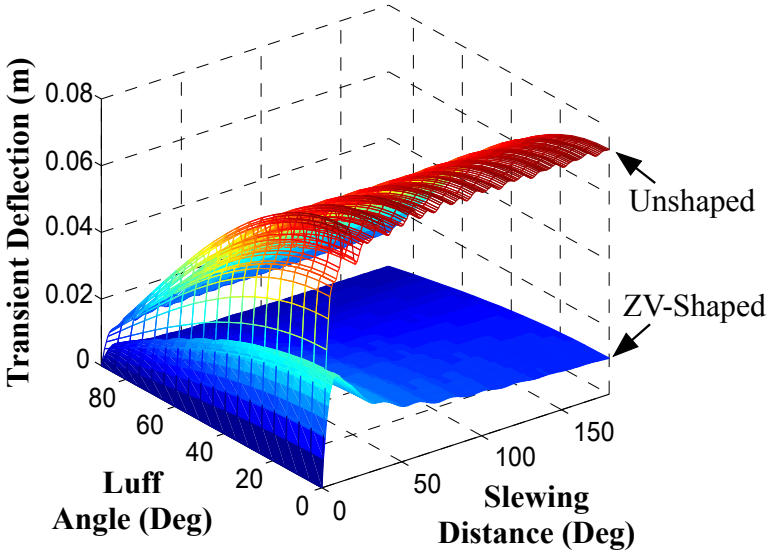

Figure 4.11: Slewing Transient Deflection

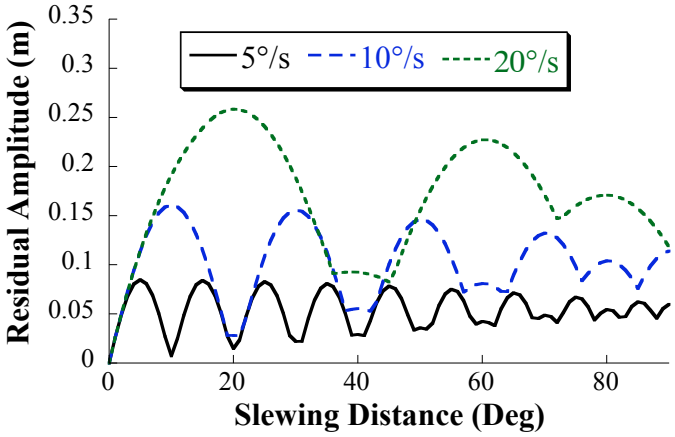

Figure 4.12: Unshaped Residual Vibration Amplitude vs. Slewing Velocity

These velocity and acceleration values, however, correspond reasonably well with those of real boom cranes. For higher velocities, nonlinear effects become more significant and the effectiveness of input shaping decreases. To demonstrate the effect of velocity on the boom crane dynamics, Figure 4.12 shows the unshaped residual vibration amplitude for slewing distances between 0° and 90° for three different maximum velocities: $5°/s$, $10°/s$, and $20°/s$. For each velocity limit, the acceleration and deceleration pulse sizes were set accordingly to keep the acceleration limit constant at $25°/s^2$.

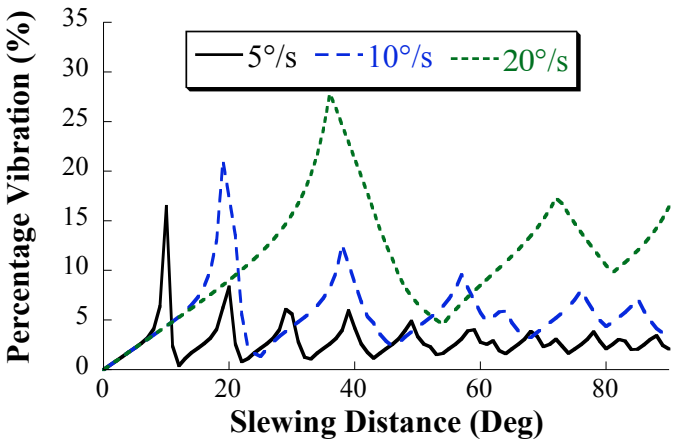

Figure 4.13: ZV-Shaped Percentage Residual Vibration vs. Slewing Velocity

Increasing the maximum velocity has two effects: *i)* increase in peak vibration amplitudes and *ii)* change in location of peaks and troughs. The shift in the location of the peaks and troughs is predictable, at least for smaller slewing distances where nonlinear affects are not very significant. For example, doubling the velocity from $5°/s$ to $10°/s$ moves the peak at 5° and the trough at 10° (on the $5°/s$ curve) to 10° and 20°, respectively (on the $10°/s$ curve).

The percentage residual vibration resulting from ZV-shaped commands for the same three maximum velocities is shown in Figure 4.13. The ZV-shaped commands reduced the residual vibration amplitude by an average of 97%, 95%, and 89% for velocities of $5°/s$, $10°/s$, and $20°/s$, respectively. The effectiveness of input shaping decreases with increasing maximum velocity; however, shaping still significantly reduces the residual vibration.

Experiments were performed to verify the slewing dynamics and the effectiveness of input shaping. As an initial test of input shaping, the crane was slewed 5°. Figure 4.14 shows the tangential swing caused by unshaped and ZV-shaped trapezoidal velocity commands. The ZV shaper was designed for a suspension cable length of 1 m. Besides the nonlinear rotation associated with the slewing motion, the slewing axis of the small-scale boom crane has other sources of nonlinearity such as backlash

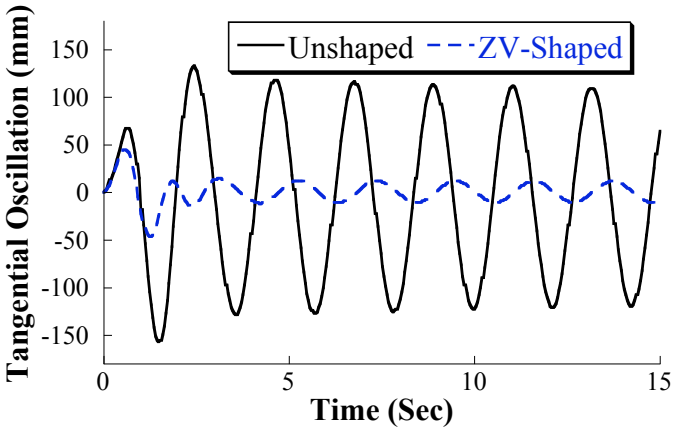

Figure 4.14: Experimental Slewing Response

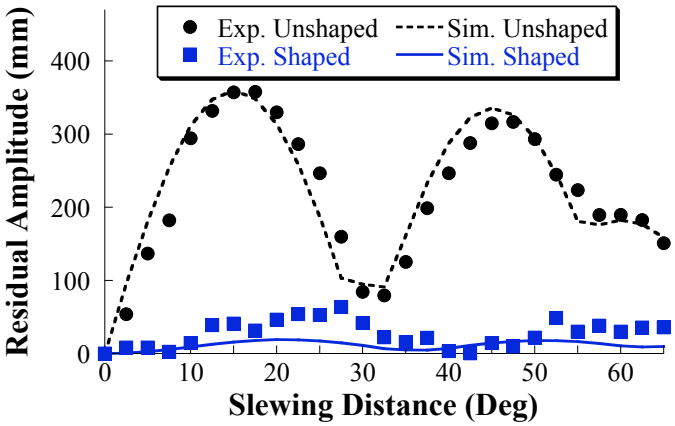

Figure 4.15: Experimental Slewing Residual Vibration Amplitude

in the belt-drive system. Nonetheless, the ZV input shaper substantially reduced the payload swing, as predicted by the simulations.

To verify the alternating peaks and troughs in the residual oscillation amplitude, the crane was slewed for distances between 0° and 65°, in increments of 2.5°. The luffing angle and suspension cable length were held constant at 50° and 1 m, respectively. Figure 4.15 shows the experimental and simulated residual vibration amplitudes. The residual amplitude increases and decreases as the slewing distance is increased, similar to the results obtained through simulation. Figure 4.15 also shows the ZV-shaped residual vibration amplitudes for the same slewing distances. The ZV-shaped commands reduced the residual vibration amplitude by an average of 88%. Notice that

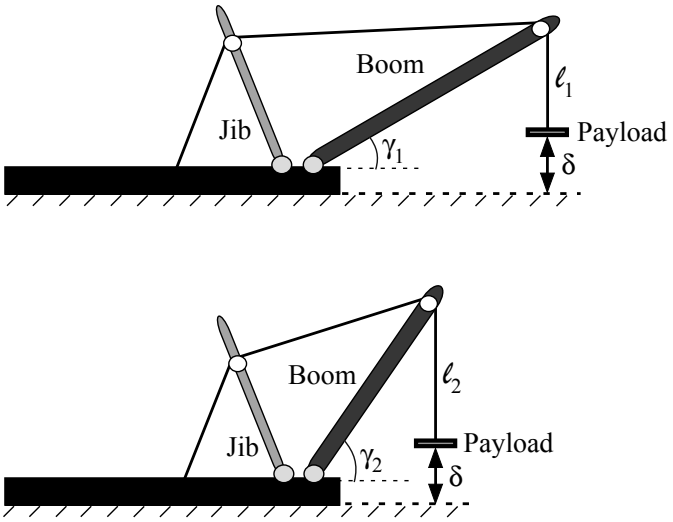

Figure 4.16: Level Luffing

this value is lower than the predicted percent reduction from simulation. The difference can be attributed to the nonlinearities discussed earlier. Nonetheless, the simulated and experimental results are very consistent with one another.

4.1.2 Luffing

Luffing motion of the boom crane occurs when the boom rotates, with angle γ, in a vertical plane. During numerical simulation, the maximum velocity of the luffing motion is limited to $6.67°/s$ and the maximum acceleration is limited to $83.33°/s^2$.

The luffing of the boom moves the payload in two directions simultaneously, in the radial and vertical directions. The vertical motion of the payload is typically achieved via a hoisting actuation in most cranes. However, to maintain a constant payload distance from the ground when luffing, boom cranes can employ a technique called level luffing, illustrated in Figure 4.16.

For level luffing, the suspension length, ℓ, changes in coordination with the luffing angle, γ, in order to keep the payload at the same height, δ, above ground. The model used here can rotate the boom both with and without level luffing.

Unlike the slewing motion, luffing results only in oscillation in the radial direction. For example, the boom was luffed upward from an initial angle of 30° to a final angle

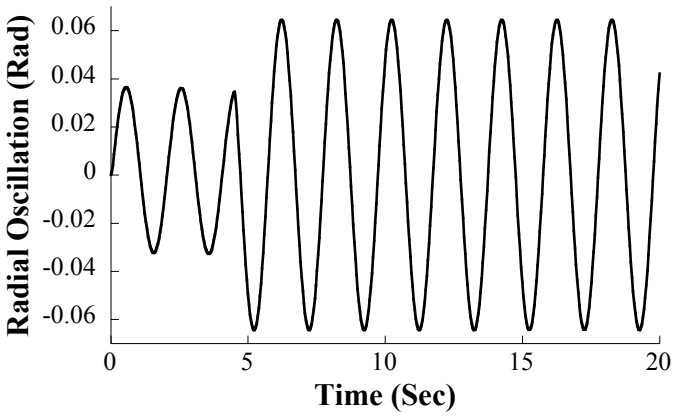

Figure 4.17: Radial Oscillation for an Upward Luff from 30° to 60°

of 60°. The slewing angle was set to zero, and the suspension cable length was kept constant at 1 m (no level luffing). Figure 4.17 shows the radial payload oscillation. The stopping oscillation is in phase with the starting oscillation, thereby increasing the residual vibration amplitude above the transient level. After the transient stage, the payload simply swings back and forth with approximately 13 cm peak-to-peak residual swing. The residual vibration amplitude caused by luffing motions is generally smaller than those produced by slewing commands because some portion of the acceleration is in the vertical direction. This vertical acceleration does not induce pendulum swing like horizontal accelerations.

The luffing dynamics are complicated because the magnitude of payload oscillation caused by a specific move distance is dependent on both the initial luff angle and the final luff angle. The direction of motion, upward or downward, can also be significant because the effect of gravity changes. When luffing upward, the payload is moving against the gravitational force; however, when luffing downward, the payload is moving along with gravity. The changes in the net applied forces not only change the oscillation amplitude, but also the oscillation frequency during accelerations [13]. However, this only becomes significant if the luffing acceleration is a substantial fraction of the gravitational acceleration. For the luffing acceleration limit used here, the maximum vertical acceleration (which occurs at $\gamma = 0°$) is only approximately 25%

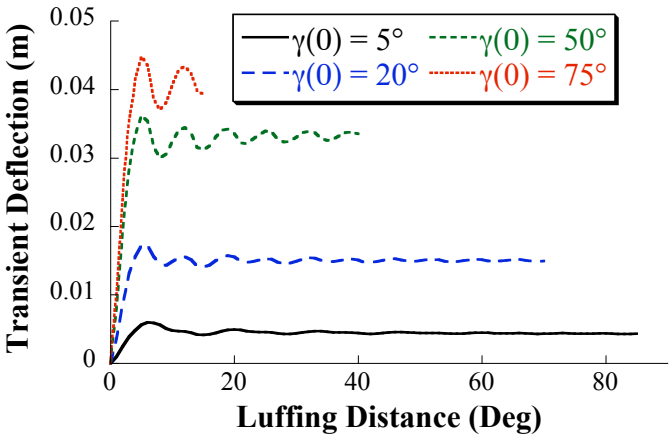

Figure 4.18: Transient Deflection vs. Luffing Distance

of the gravitational acceleration. This value decreases as the luffing angle increases.

Figure 4.18 shows the relationship between average transient deflection and luffing distance for upward luffing from four different initial luff angles, $\gamma(0) = [5°, 20°, 50°, 75°]$. All of the curves do not span the entire Luffing-Distance axis because the luffing angle was limited to between 0° and 90°. For example, if the initial luff angle is 75°, then the maximum allowable upward luffing distance is only 15°, as shown by the dotted line in Figure 4.18.

The amount of transient deflection depends on the size of the acceleration pulse and the duration of the transient stage. For small luffing distances, the width of the acceleration pulse increases with luffing distance. However, once the maximum velocity is reached, the width of the acceleration pulse stops increasing. After this point, the transient deflection is no longer dependent on the acceleration pulse size, but still varies as the luffing distance (the transient duration) is increased. This variation is due to the interference between the starting and stopping oscillations during the transient stage. As the luffing distance becomes large, however, the starting oscillation comprises a larger portion of the transient stage than the oscillation resulting from the interference between the starting and stopping oscillations. As a result, the average transient deflection levels out.

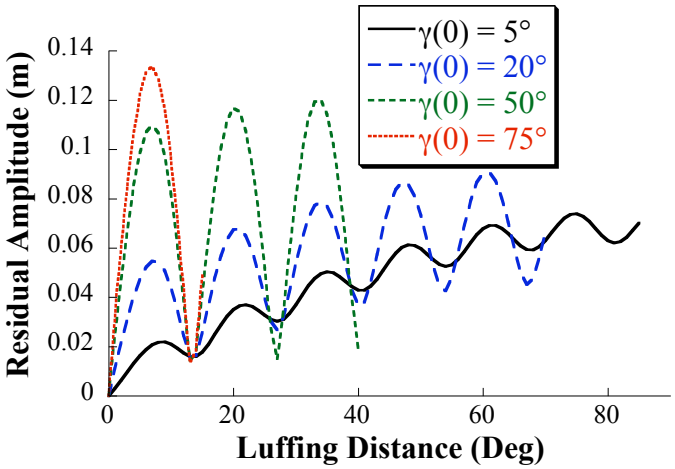

Figure 4.19: Residual Vibration Amplitude vs. Luffing Distance

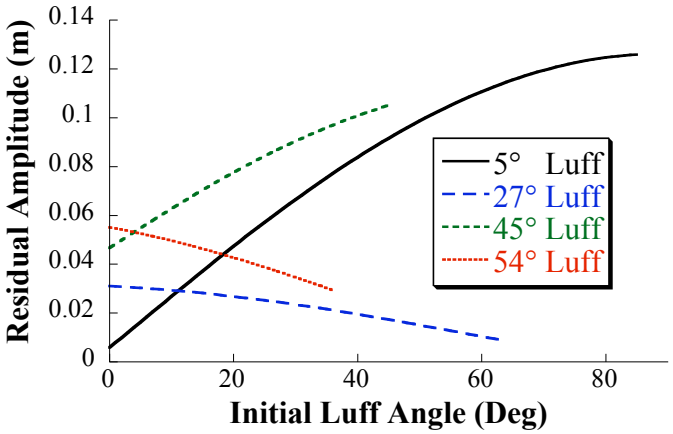

Figure 4.20: Residual Vibration Amplitude vs. Initial Luff Angle

Figure 4.19 shows the relationship between residual vibration amplitude and luffing distance for upward motion from four different initial luff angles. As explained before, the peaks and troughs are created when the starting and stopping oscillations align in phase to create the peaks and occur out of phase to create the troughs.

Figure 4.20 shows the relationship between residual vibration amplitude and initial luff angle for upward luffing. For certain luffing distances, for example 5° and 45°, larger initial luff angles lead to larger residual vibration. This occurs because for small initial luff angles, the boom is mainly in the horizontal plane. In this configuration, the starting motion is mostly vertical and does not contribute significantly to the radial swing of the payload. For large initial luff angles, on the other hand, the

starting motion has a larger component in the radial direction and therefore, results in larger radial payload oscillation. However, for some luffing distances, such as 27° and 54°, the residual vibration amplitude decreases for increasing initial luff angle. These luffing distances correspond to the troughs of Figure 4.19. For these luffing distances, the starting and stopping oscillations are out of phase. As the initial luff angle increases, the magnitude of the starting oscillation increases, becoming closer to the magnitude of the stopping oscillation. Because the oscillations are out of phase, the residual vibration amplitude decreases.

Luffing downward produces similar relationships to those during upward luffing. For equal luffing distances, luffing upward and downward will produce approximately the same magnitude of residual vibration if the initial and final luff angles are exactly reversed. For example, luffing from an initial angle of 45° to a final luffing angle of 65° produces 0.1104 m of residual vibration. Luffing downward from an initial luffing angle of 65° to a final luffing angle of 45° produces 0.1105 m of residual vibration. The transient deflections of the two scenarios, on the other hand, are different because the amount of transient deflection depends heavily on the initial luff angle.

Iterative simulation routines were carried out for the luffing motion to further investigate the relationship between the oscillation (transient and residual), move distance, and initial luff angle. The suspension cable length was set to 1 m and the initial luff angle and luffing distance were varied between 0° and 90°. Figure 4.21 shows the residual vibration amplitude from upward luffing for unshaped and ZV-shaped commands. Input shaping reduced residual vibration by an average of 97% and reduced the transient deflection by an average of 62%.

4.1.3 Level Luffing

The analysis in Section 4.1.2 assumes that the luffing motion does not induce a change in the length of the suspension cable length. Because many boom cranes utilize level

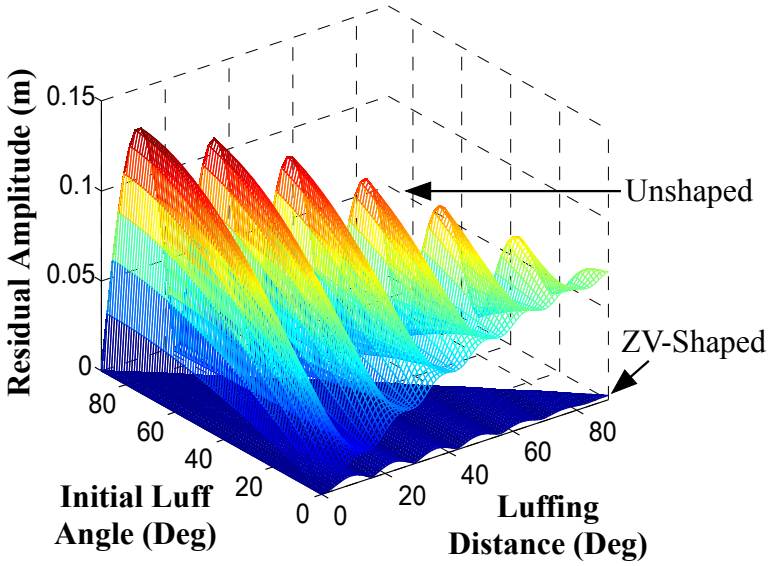

Figure 4.21: Upward Luffing Residual Vibration Amplitude

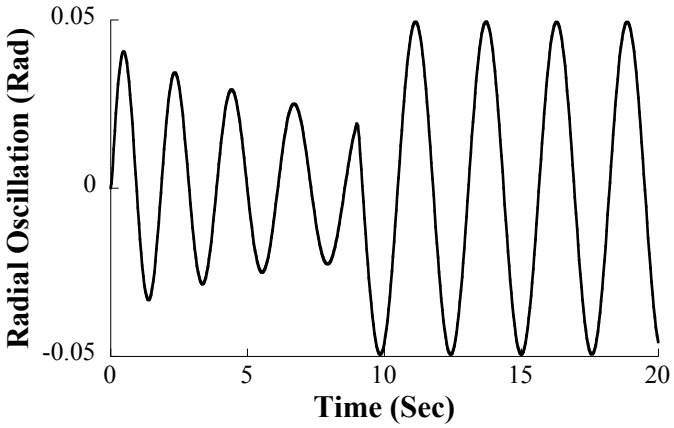

Figure 4.22: Radial Payload Oscillation for Level Luffing from 30° to 90°

luffing, it is of interest to analyze how the dynamics change when level luffing is used. During this investigation, the payload was maintained 20 cm above "ground" during the luffing motion. For example, if the initial luff angle was 30° and the boom was luffed upward 60°, then the suspension cable length would change from 0.725 m to 1.65 m. This change in suspension cable length allows the payload to remain at the same vertical level. Figure 4.22 shows the radial payload oscillation for luffing from 30° to 90°, while keeping the payload 20 cm above ground.

The change in cable length has two effects on the transient deflection: *i)* change in

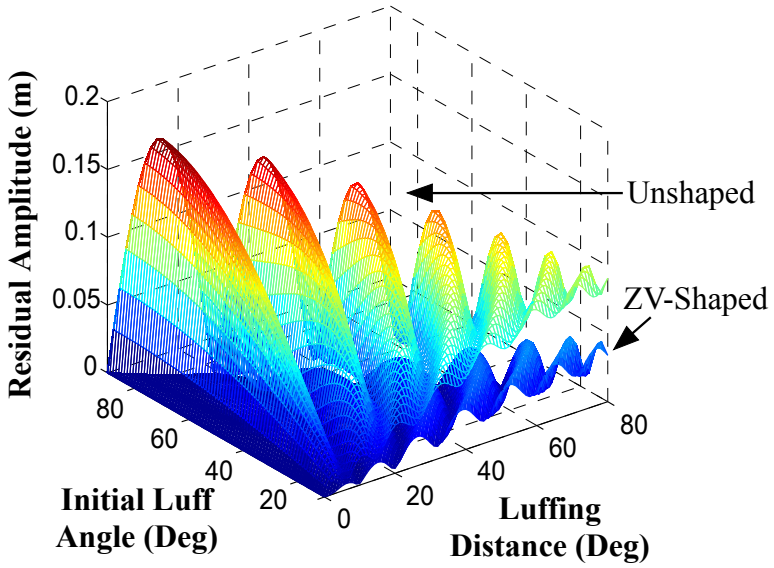

Figure 4.23: Upward Level Luffing Residual Vibration Amplitude

frequency and *ii)* change in amplitude. At the 30° starting angle, the suspension cable length is short, so the frequency of oscillation is high. As the suspension cable length increases to accomplish the level-luffing, the frequency is lowered. The decrease in amplitude is a result of the nonlinear dynamics of the crane. Hoisting up and down can either increase or decrease (dampen) the vibration amplitude [1, 8]. In the level-luffing case shown above, the hoisting motion, which occurs simultaneously with the luffing motion, decreases the oscillation amplitude.

Figure 4.23 shows the maximum residual vibration amplitude over a range of conditions when the payload is kept 20 cm above ground during level luffing. The results are a warped version of those for the non-level-luffing case in Figure 4.21. The warping effect is due to the change in the natural frequency induced by the change in the suspension cable length associated with level luffing. The residual vibration amplitude varies in an oscillatory manner; however, this pattern is more complex. This is because the cancellation or addition of the oscillations caused by the starting and stopping accelerations now depend not only on the move distance, but also on the varying frequency of the oscillation.

Input shaping requires very little knowledge of the system being controlled. However, it does require a reasonable estimate of the natural frequency of the system. During level-luffing operations, the natural frequency varies. ZV shapers are not very robust to modeling errors; therefore, the ZV shapers used here were designed for the average natural frequency of each motion. For example, for luffing from 30° (0.725 m) to 90° (1.65 m), the ZV shaper was designed for a suspension cable length of 1.19 m. The residual vibration amplitude resulting from these ZV-shaped commands is also shown in Figure 4.23. The shaped commands reduced the residual vibration amplitude by an average of 83%. As expected, ZV shaping is less effective at reducing the residual vibration amplitude when there is a time-varying oscillation frequency during level luffing. However, it still provides substantial vibration reduction. The transient deflection was also investigated for level luffing. ZV shaping reduced the transient deflection by an average of 51%.

Experiments were performed to verify two important aspects of the simulation results: *i)* the effectiveness of input shaping at reducing the residual oscillation, and *ii)* the alternating peaks and troughs in the residual oscillation amplitude as a function of move distance. As an initial test of input shaping, the crane was luffed from an initial angle of 20° upward by 5°. Figure 4.24 shows the radial swing angle caused by both unshaped and ZV-shaped trapezoidal velocity commands. Input shaping substantially reduced the payload swing, as predicted by the simulations.

To verify the alternating peaks and troughs in the residual oscillation amplitude, the crane was luffed upward from an initial luffing angle of 20° for distances between 0° and 55°. At the initial state, the payload was 20 cm above the ground. The boom crane has a physical design that provides automatic level luffing as the boom is luffed. The level luffing is optimized to work best in the range of 40° to 70°. Outside of that range, the payload height above ground does not stay perfectly level. However, the suspension cable length does change to provide approximate height

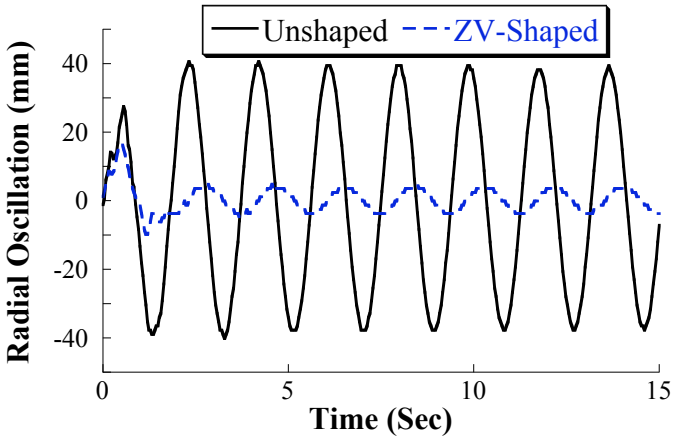

Figure 4.24: Experimental Luffing Response

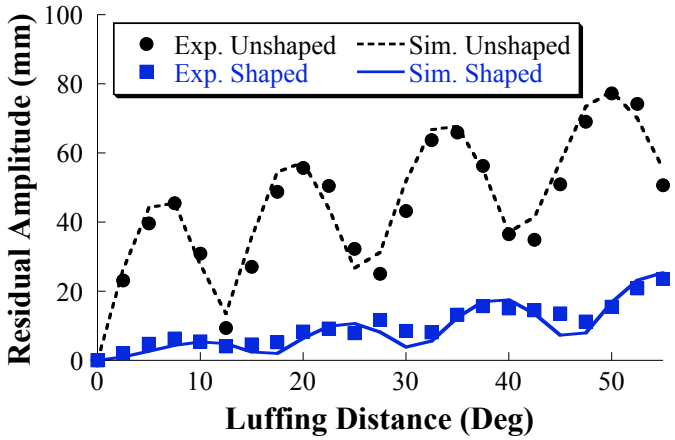

Figure 4.25: Experimental Upward Level Luffing Residual Vibration Amplitude

compensation. Figure 4.25 shows the experimental and simulated residual oscillation amplitudes. This figure represents a slice through Figure 4.23 at the point where the initial luff angle is 20°. Notice that the simulated results predict the experimental values very closely. The residual vibration amplitude increases and decreases as the luffing distance is increased, similar to the results obtained through simulation. Figure 4.25 also shows the shaped residual vibration amplitude for the same luffing distances. The ZV shapers were designed for the average natural frequency during the luffing motion. The ZV-shaped commands reduced the residual vibration amplitude by an average of 77%.

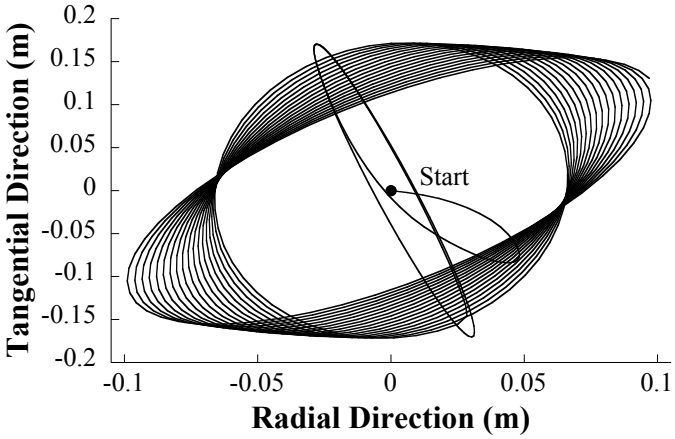

Figure 4.26: Payload Response to 10° Slew and 30° Luff

4.1.4 Combined Slewing and Luffing

The boom crane dynamics become even more complex when two rotations are performed simultaneously. Figure 4.26 shows the location of the payload relative to the overhead suspension point during an upward luffing from 45° to 75°, and a simultaneous 10° slewing. The suspension cable length was kept constant at 1 m. The payload motion during the transient stage is a complicated function of the radial, tangential, and centripetal accelerations caused by the slewing and luffing commands. However, once the slewing and luffing commands are complete, the payload moves in symmetric loops, similar to those caused by slewing commands alone.

In order to analyze the effectiveness of input shaping on the combined luffing and slewing motions, both unshaped and ZV-shaped commands were used to drive the boom crane model for luffing distances between 0° and 55°, from an initial luff angle of 35°, and slewing distances between 0° and 90°. Figure 4.27 shows the residual vibration amplitude as a function of slewing and luffing distances. There are variations in the residual vibration amplitude with respect to changes in luffing distance. However, there are much larger variations in the residual vibration amplitude with respect to slewing distance. As seen in the previous data, slewing commands produce larger residual vibration and are responsible for the majority of the residual

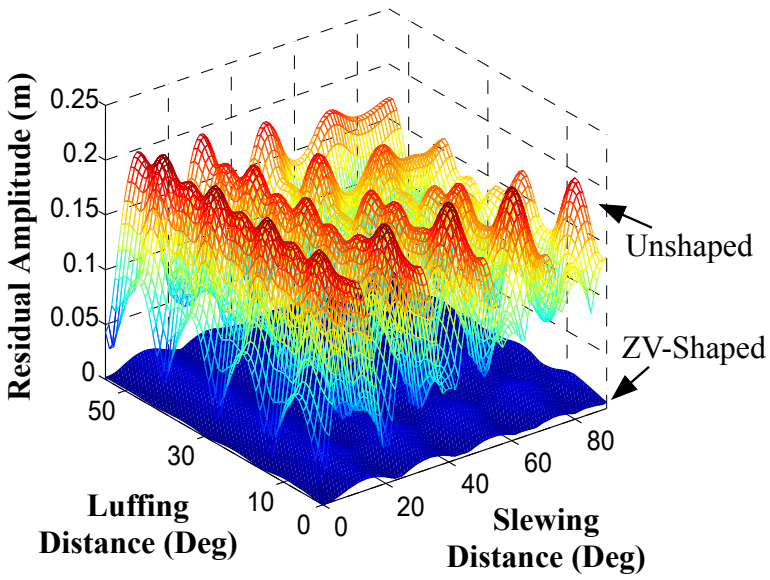

Figure 4.27: Luffing and Slewing Residual Vibration Amplitude

vibration amplitude. Even given the complicated dynamics of multiple-axis motion, ZV-shaping is still able to substantially reduce the residual vibration amplitude for all combinations of slewing and luffing commands. For the parameter space shown in Figure 4.27, input shaping reduced residual vibration by an average of 93%.

Figure 4.28 shows the unshaped and shaped average transient deflection for slewing and upward luffing. There are oscillatory variations as the luffing and slewing distances are varied. However, as the slewing and luffing distances become large, these variations begin to level out. The ZV-shaped commands reduced the transient deflection by an average of 76%.

4.1.5 Mobile Base

Motion of the mobile base is divided into the linear movement of the base, x and y, and the rotation, α, of the mobile base about a vertical axis in the inertial Newtonian frame. These parameters are defined as functions of the input variables: linear speed, v, and steering angle, ψ. During numerical simulation of the boom crane, the maximum driving velocity is limited to 0.35 m/s and the maximum acceleration is limited to 0.7 m/s^2.

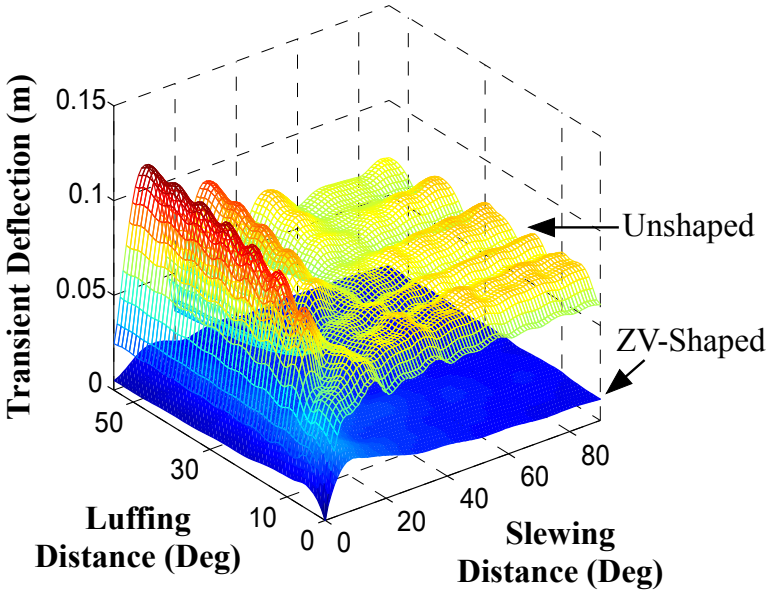

Figure 4.28: Luffing and Slewing Transient Deflection

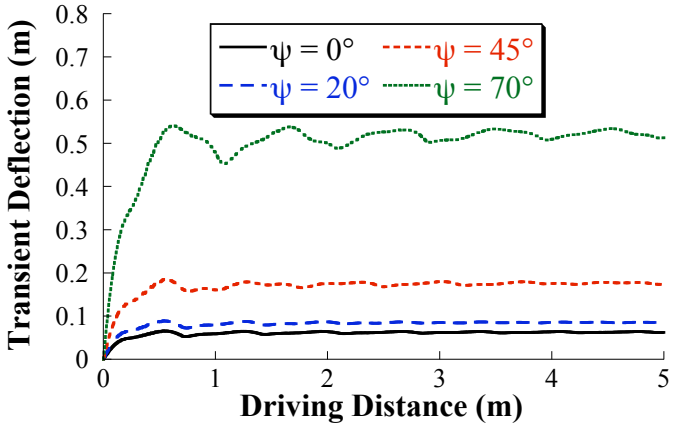

Figure 4.29: Transient Deflection vs. Driving Distance

Figure 4.29 shows the transient deflection for move distances between 0 m and 5 m for 4 different steering angles. The luffing angle was held constant at 45°, and the suspension cable length was set to 1 m. The amount of transient deflection depends on the size of the acceleration pulse and the duration of the transient stage. For small driving distances, the width of the acceleration pulse increases with driving distance. However, once the maximum velocity is reached, the width of the acceleration pulse stops increasing. After this point, the transient deflection is no longer dependent on the acceleration pulse size, but still varies as the driving distance (the transient

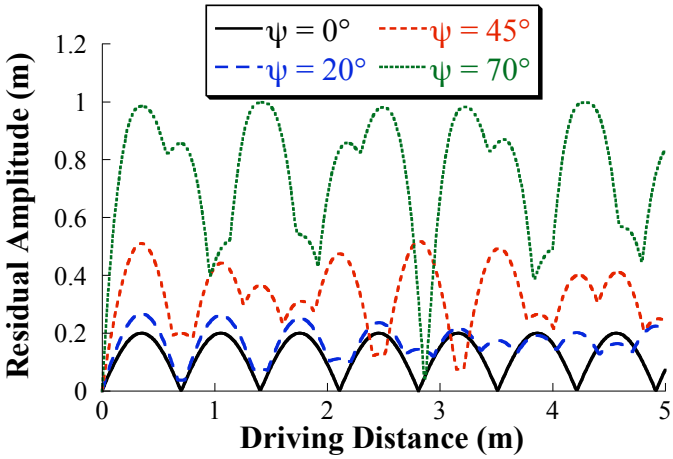

Figure 4.30: Residual Vibration Amplitude vs. Driving Distance

duration) is increased. This variation is due to the interference between the starting and stopping oscillations during the transient stage. As the driving distance becomes large, however, the starting oscillation comprises a larger portion of the transient stage than the oscillation resulting from the interference between the starting and stopping oscillations. As a result, the average transient deflection levels out.

Figure 4.30 shows the maximum residual vibration amplitude for the same parameter space as in Figure 4.29. For a steering angle of 0°, driving results only in radial oscillation of the payload. This is demonstrated in Figure 4.30 by the solid line. Driving in a straight line is approximately linear. As the driving distance varies, the oscillation caused by the starting and stopping accelerations are sometimes in phase causing the peaks and sometimes out of phase causing near-zero residual vibration amplitude. This pattern is similar to the trends observed for slewing and luffing commands.

As the steering angle increases, the mobile base rotates faster causing higher centripetal and tangential accelerations (for example, for a steering angle of 70°, the rotation rate of the mobile base is approximately $60°/s$). These higher accelerations increase the residual vibration amplitude. In addition, the higher mobile base rotation rates produce more nonlinear effects.

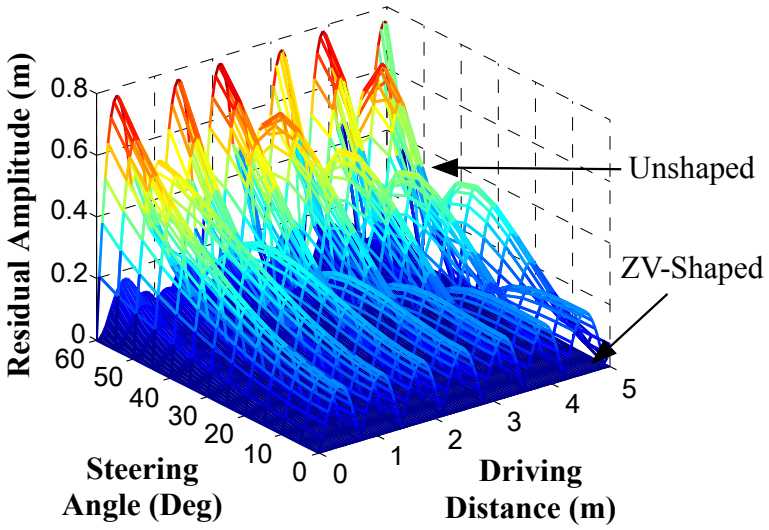

Figure 4.31: Driving Residual Vibration Amplitude

To control the payload oscillation caused by driving motions, ZV-shaped commands were used. The ZV shaper was designed for the frequency of a single pendulum with a 1 m length. Figure 4.31 shows the maximum residual vibration amplitude for driving distances from 0 m to 5 m and for steering angles from 0° to 60°. For higher steering angles, the rotation rate of the mobile base increases dramatically and the ZV shaper loses some effectiveness. However, the steering angle of most vehicles, including the mobile base of the small-scale boom crane, is generally limited to a range of approximately -45° to 45°. Even with these extreme conditions included (steering angles between 0° and 60°), ZV-shaped commands reduced the maximum residual vibration amplitude by an average of 89%. The transient deflection was also analyzed for the same parameter space. ZV-shaped commands reduced the transient deflection by an average of 68%.

Experiments were performed to verify the dynamics of the mobile base, as well as the effectiveness of input shaping. Figure 4.32 shows the radial oscillation of the payload resulting from a 40 cm straight-line driving motion. The response of the payload to the ZV-shaped command is also shown. The shaper was able to significantly reduce the residual vibration, as predicted by the simulations.

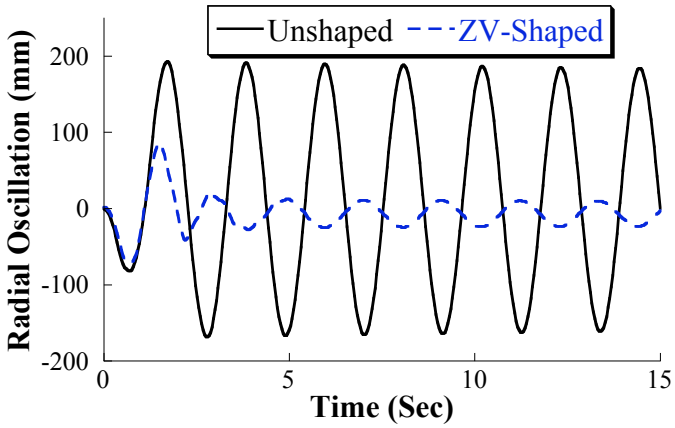

Figure 4.32: Experimental Driving Response

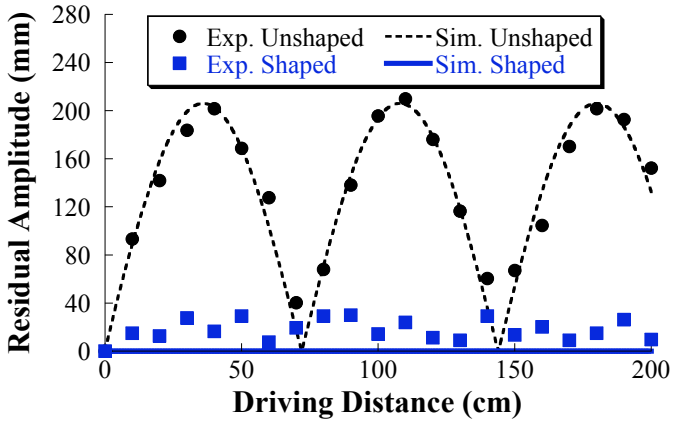

Figure 4.33: Experimental Driving Residual Vibration Amplitude

Next, the mobile base of the small-scale boom crane was driven in a straight line for distances between 10 cm and 200 cm, in increments of 10 cm, using both unshaped and ZV-shaped commands. Figure 4.33 shows the experimental and simulated residual vibration amplitudes induced by unshaped and ZV-shaped driving commands. This figure represents a slice through Figure 4.31 where the steering angle, ψ, is zero. The simulated ZV-shaped vibration amplitudes are virtually zero, but the ZV-shaped experimental vibration amplitudes are slightly larger (with an average of 18 mm). This difference is because of the nonlinearities of the experimental setup. The main source of these nonlinearities is the belt-drive system. The unshaped simulated and experimental results, on the other hand, match well.

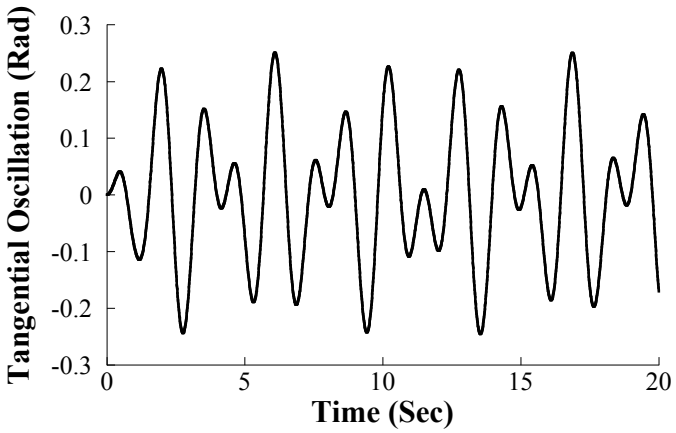

Figure 4.34: Tangential Oscillation from 10° Slew with Double-Pendulum Payload

Similar to the simulation results, the unshaped driving residual vibration amplitude contains peaks and troughs as the driving distance is varied. The ZV-shaped commands, however, are much less dependent on the driving distance, as they reduce the residual vibration amplitude to near zero for all move distances. The ZV-shaped commands reduced the residual vibration amplitude by an average of 87%.

4.2 Double-Pendulum Dynamics

Figure 4.34 shows the tangential payload swing for a 10° slew with a double-pendulum payload. The two oscillation modes are clearly visible in this figure. Unlike the single-pendulum system, the vibration frequencies of a double pendulum depend not only on the suspension cable length, but also on the rigging cable length and the masses of the hook and payload [40]. Because these parameters can be different from one crane operation task to another, the controller needs to suppress two varying oscillation modes.

The luffing motion is particularly challenging with double-pendulum payloads not only because it is a rotational motion, but also because in many boom cranes, a change in the luffing angle produces a change in the suspension cable length. This level-luffing technique is demonstrated in Figure 4.35 for a double-pendulum payload. The length of the suspension cable (L_1) changes in conjunction with luffing angle changes (γ) to

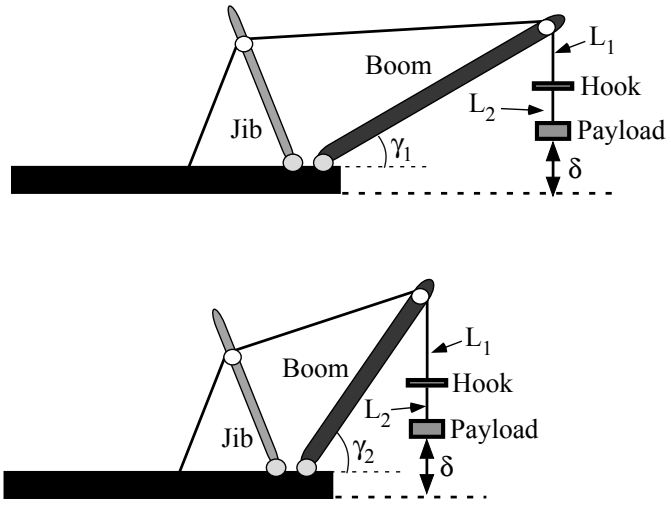

Figure 4.35: Level Luffing with Double-Pendulum Payload

keep the payload the same height above the ground.

As explained in section 3.1, feedback control of double-pendulum payloads is challenging because of the difficulty of measuring the position of the payload and the constantly varying double-pendulum dynamics. Therefore, a robust input shaper is designed that can eliminate residual vibration across a large range of double-pendulum parameters. The next section presents the process followed to design a robust shaper for the small-scale mobile boom crane. It concludes with a set of general guidelines to follow to design robust shapers for related applications. The robustness of the shaper is then verified through simulations and experiments.

4.2.1 Shaper Design

Specified Insensitivity (SI) shapers [27, 40, 43] were chosen for this application. These shapers allow the designer to specify the desired range of frequency suppression. Figure 4.36 demonstrates the design constraints of a two-mode SI shaper. Two frequency suppression ranges, I_1 and I_2, and the tolerable vibration, V_{tol}, over the two ranges are specified. An optimization utilizing the MATLAB optimization toolbox obtains the shaper amplitudes and times that satisfy the vibration-suppression constraints.

The first step in designing a robust input shaper for double-pendulum payloads

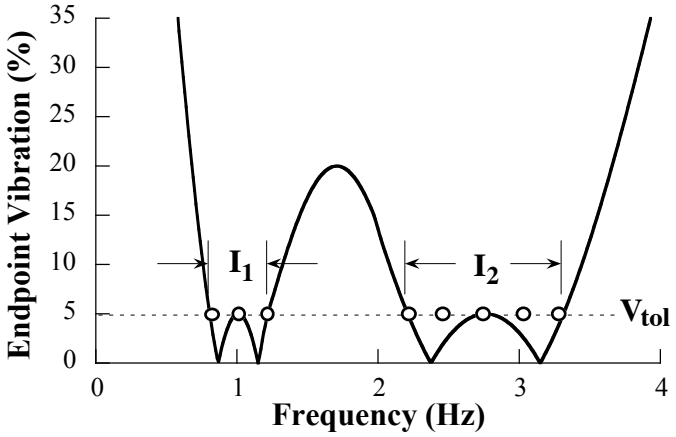

Figure 4.36: Two-Mode SI Shaper Design Process

is to determine the effect of all the varying parameters on the oscillation frequencies. Because there are four different parameters (suspension cable length, rigging cable length, payload mass, and hook mass) that can be varied, it is important to determine how the parameter values affect the oscillation modes. The linearized frequencies of oscillation for a given set of parameters are [7]:

$$\omega_{1,2} = \sqrt{\frac{g}{2}}\sqrt{(1+R)\left(\frac{1}{L_1}+\frac{1}{L_2}\right) \mp \beta} \tag{4.1}$$

$$\beta = \sqrt{(1+R)^2\left(\frac{1}{L_1}+\frac{1}{L_2}\right)^2 - 4\left(\frac{1+R}{L_1 L_2}\right)} \tag{4.2}$$

The gravitational acceleration is represented by g, L_1 is the suspension cable length, L_2 is the rigging cable length, and R is the ratio of the payload mass to the hook mass. In most cranes the hook is not interchangeable, so it was fixed at 0.63 kg to match the hook mass of the small-scale boom crane used for the experiments in this section.

Figure 4.37 shows the variation in the first and second modes as a function of the suspension cable length and the payload mass. The suspension cable length was varied from 0.05 m to 2 m and the payload mass was varied from 0 kg to 2 kg. The rigging cable length was fixed at 0.3 m. The second mode clearly undergoes a larger variation than the first mode. The second-mode frequency rapidly increases with

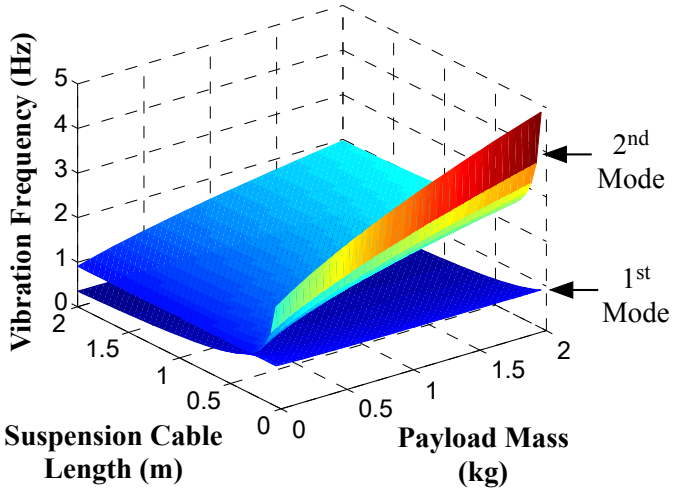

Figure 4.37: Oscillation Frequency vs. Suspension Cable Length and Payload Mass

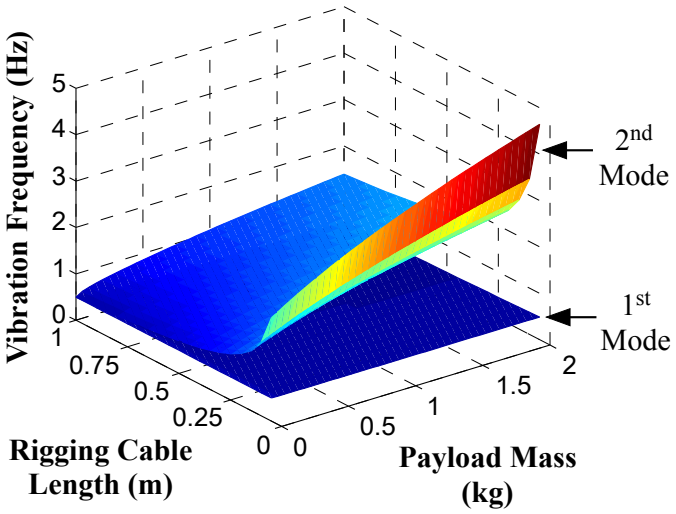

Figure 4.38: Oscillation Frequency vs. Rigging Cable Length and Payload Mass

small suspension cable lengths, which are uncommon in crane applications. If small suspension cable lengths (less than 0.2 m) are ignored, then the first mode varies from 0.33 Hz to 0.91 Hz, while the second mode varies from 0.91 Hz to 2.85 Hz.

Figure 4.38 shows the variation in the first and second modes as a function of the rigging cable length and the payload mass. The rigging cable length was varied from 0.05 m to 1 m and the payload mass was again varied from 0 kg to 2 kg. The suspension cable length was held constant at 1 m. Once again, the variation

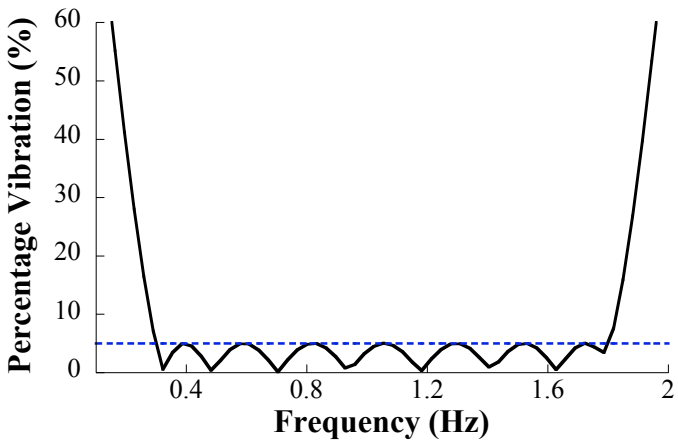

Figure 4.39: Two-Mode SI Shaper Sensitivity Curve

in the second mode is more visible. The second mode rapidly increases with very short rigging cable lengths. For short rigging cable lengths, however, the payload is effectively a single pendulum, and the high mode no longer produces a significant oscillation amplitude [27, 40]. If short rigging cable lengths (less than 0.1 m) are ignored, then the first mode varies from 0.36 Hz to 0.50 Hz, while the second mode varies from 0.5 Hz to 3.34 Hz.

Based on this analysis, the range of frequency suppression was chosen to be from 0.3 Hz to 0.9 Hz for the low mode and from 1 Hz to 1.8 Hz for the high mode. The tolerable vibration percentage was chosen to be 5% for both ranges. The SI shaper meeting these design requirements is:

$$\begin{bmatrix} A_i \\ t_i \end{bmatrix} = \begin{bmatrix} 0.0569 & 0.0844 & 0.1237 & 0.1530 & 0.1639 & 0.1530 & 0.1237 & 0.0844 & 0.0569 \\ 0 & 0.4724 & 0.9449 & 1.4174 & 1.8899 & 2.3624 & 2.8350 & 3.3076 & 3.7801 \end{bmatrix} \quad (4.3)$$

Figure 4.39 shows the sensitivity curve for the two-mode SI shaper in (4.3). For the entire range of 0.3 Hz to 1.8 Hz, the percentage residual vibration (PRV) is below the desired 5%. However, for frequencies above and below this range, the PRV increases rapidly.

This shaper design procedure can be generalized as:

1. Estimate the range of payloads that a crane will move. (The maximum capacity of the crane can be used.)
2. Estimate the possible ranges of the rigging and suspension cable lengths.
3. Determine the possible frequency ranges for the low and high modes.
4. Set a tolerable vibration percentage, V_{tol}.
5. Use numerical optimization to obtain the shaper.

4.2.2 Numerical Shaper Performance Verification

Simulations using the double-pendulum model in Section 2.3.2 were performed to analyze the performance of input shaping for a variety of parameters. The first set of simulations evaluated the dynamics and shaper performance of double-pendulum slewing motions. The luffing angle was held constant at 45° and the rigging cable length and the payload mass were set to 0.3 m and 0.2 kg, respectively. The hook mass was fixed at 0.63 kg. The crane was slewed for distances between 5° and 90°, at 5° increments. For each slewing distance, the suspension cable length was varied from 0 m to 2 m. Figure 4.40 shows the maximum residual vibration amplitude for this parameter space. Note that the residual vibration amplitude shown here (and in all the figures in this section) is the peak-to-peak displacement of the payload relative to the overhead suspension point. The unshaped residual amplitude increases and decreases as the slewing distance changes, similar to the single-pendulum slewing results. However, the double pendulum makes the dynamics more complex. The two-mode SI shaper reduced the residual amplitude by an average of 96%.

In order to test dependence on rigging cable length and payload mass, the luffing angle and the slewing distance, θ_{dist}, were held constant at 45° and 40°, respectively. The suspension cable length was set to 1 m and the hook mass was again set to 0.63 kg. The 40° slewing motion was repeated for rigging cable length from 0 m to 2 m

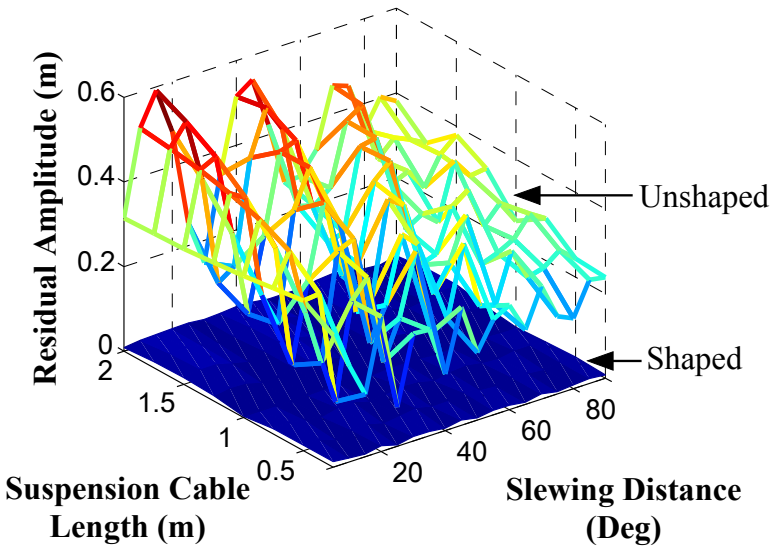

Figure 4.40: Residual Vibration Amplitude vs. Slewing Distance and Suspension Cable Length [$\gamma = 45°$, $L_2 = 0.3$ m, $m_p = 0.2$ kg]

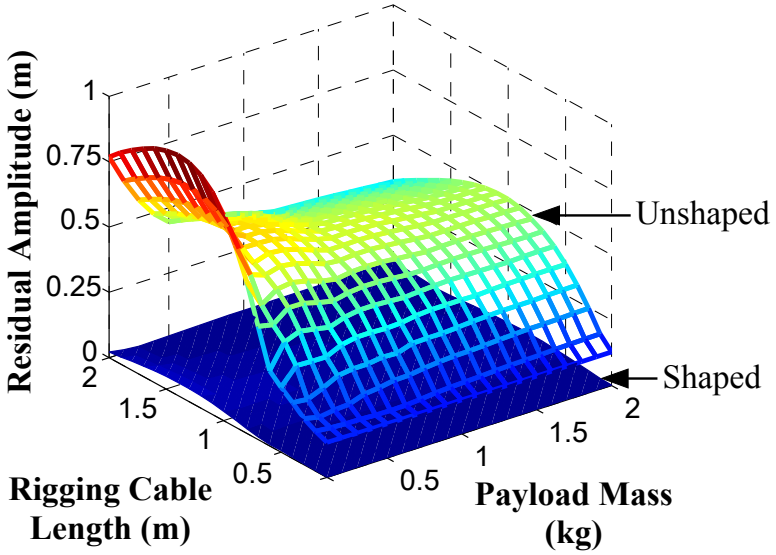

Figure 4.41: Residual Vibration Amplitude vs. Payload Mass and Rigging Cable Length [$\gamma = 45°$, $\theta_{dist} = 40°$, $L_1 = 1$ m]

and payload masses from 0 kg to 2 kg. Figure 4.41 shows the maximum peak-to-peak residual vibration amplitude for this parameter space. For rigging cable lengths close to the suspension cable length and small payload masses, the residual amplitude dramatically increases. In this range of parameters, the contribution of the second mode is significant [40]; therefore, the residual amplitude increases. The two-mode SI shaper reduced the residual amplitude by an average of 96%.

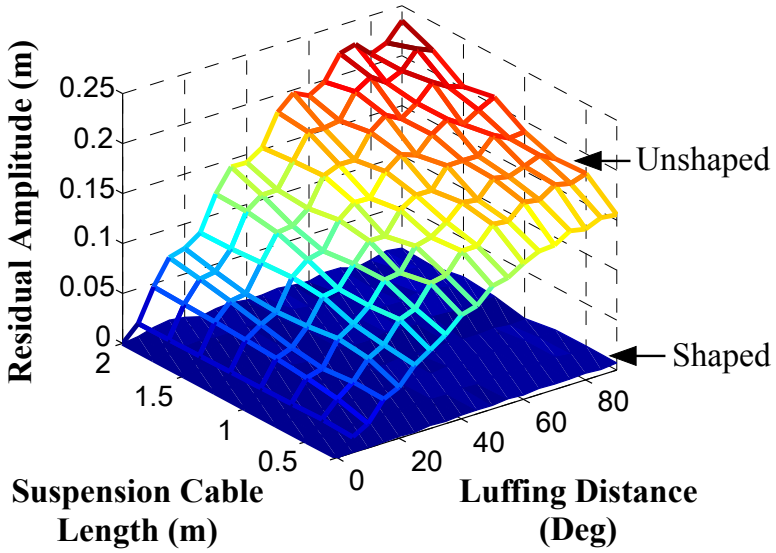

Figure 4.42: Residual Vibration Amplitude vs. Luffing Distance and Suspension Cable Length [$\gamma(0) = 0°$, $L_2 = 0.3$ m, $m_p = 0.2$ kg]

The dynamics and shaper performance of double-pendulum luffing motions were also analyzed. First, the boom was luffed upward from an initial luffing angle of 0° for distances between 5° and 90° (in 5° increments). For each luffing distance, the suspension cable was varied from 0 m to 2 m. The rigging cable length and the payload mass were held constant at 0.3 m and 0.2 kg, respectively. Figure 4.42 shows the maximum residual vibration amplitude for each test. The shaper was able to reduce the residual vibration amplitude by an average of 97% over the range of luffing distances and suspension cable lengths analyzed.

Next, the luffing distance, γ_{dist}, was held constant at 70° (a luffing motion from 0° to 70°) and the suspension cable length and the payload mass were varied from 0 m to 2 m and from 0 kg to 2 kg, respectively. Figure 4.43 shows the maximum residual vibration amplitude for these parameters. For very small payload masses and suspension cable lengths close to the rigging cable length, the residual vibration amplitude increases dramatically. However, as the suspension cable length increases beyond the rigging cable length (while the payload mass remains constant), the dynamics approach those of a single-pendulum system. The two-mode SI shaper was

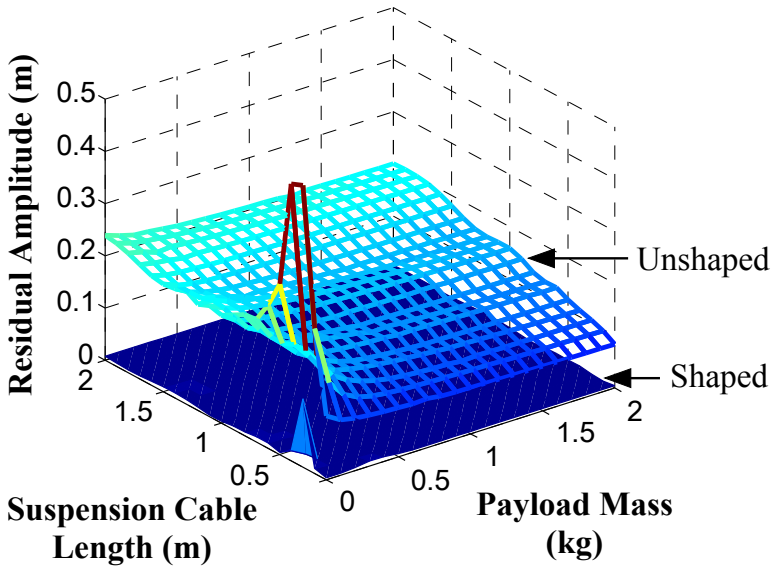

Figure 4.43: Residual Vibration Amplitude vs. Payload Mass and Suspension Cable Length [$\gamma(0) = 0°$, $\gamma_{dist} = 70°$, $L_2 = 0.3$ m]

able to reduce the residual vibration amplitude by an average of 97% over the range of payload masses and suspension cable lengths analyzed.

The simulations presented above did not utilize level luffing during the motions. Additional simulations used level luffing to keep the payload directly above the ground. Ground is represented by the location of the tip of the boom when the luffing angle is 0°. The initial luffing angle and the luffing distance were held constant at 35° and 45°, respectively. The rigging cable length was varied from 0 m to 1 m and the payload mass was varied in the same manner as before. The suspension cable length varied automatically as the rigging cable length was varied in order to keep the payload at the same vertical height (directly above ground). Figure 4.44 shows the maximum residual vibration amplitude for these simulations. Small payload masses and similar rigging and suspension cable lengths result in large residual vibration. The two-mode SI shaper was able to reduce the residual amplitude by 94% over the range of parameters analyzed.

The results displayed in Figures 4.40-4.44 clearly demonstrate that the two-mode SI shaper in (4.3) can significantly reduce the residual payload oscillation for a large

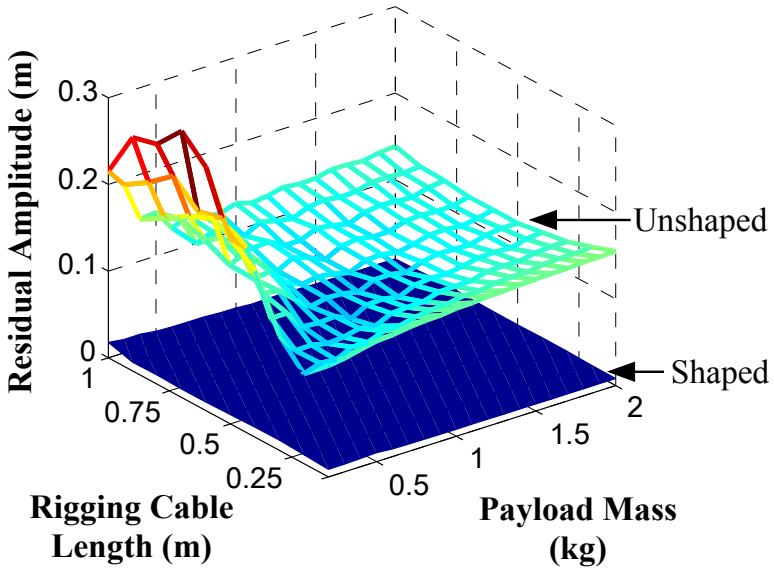

Figure 4.44: Level Luffing Residual Vibration Amplitude vs. Payload Mass and Rigging Cable Length [$\gamma(0) = 35°$, $\gamma_{dist} = 45°$]

range of double-pendulum payload dynamics and suspension cable lengths.

4.2.3 Experimental Shaper Performance Verification

The luffing axis of the small-scale boom crane was used for experimental verification of the double-pendulum dynamics and control. The double-pendulum experimental set-up is shown in Figure 4.45. An additional camera placed to the side of the crane was used to record the payload oscillation. Three different double-pendulum payloads were used in the experiments. Table 4.1 shows the parameters of these payloads and their rigging cables. Payload A is a light payload with a long rigging cable. Payload B is a medium-weight payload with a medium-length rigging cable. Payload C is a heavy payload that is used with rigging cables of various lengths during level-luffing operation.

The first set of experiments analyzed the effectiveness of the input shaper for varying luffing distances. Luffing is a rotational motion; therefore, longer luffing distances will induce more nonlinear effects. The suspension cable length was held constant at 80 cm and payload A was used. The boom was luffed upward from

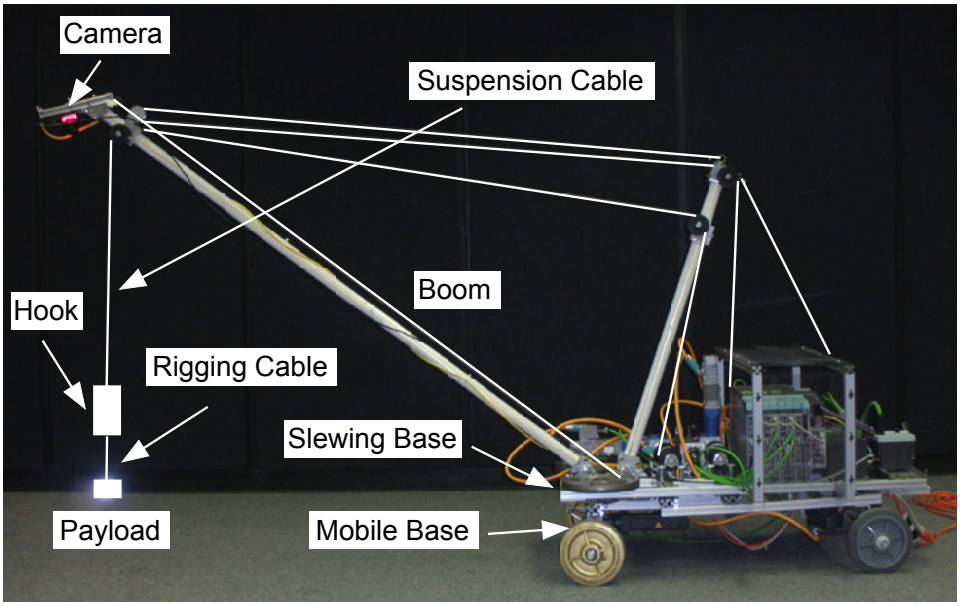

Figure 4.45: Small-Scale Mobile Boom Crane with Double-Pendulum Payload

Table 4.1: Payload and Rigging Cable Parameters

Payload	Mass (g)	Rigging Cable Length (cm)
A	200	30
B	320	15
C	870	various

an initial luffing angle of 35° for distances between 5° and 40°. Figure 4.46 shows the payload displacement (with respect to the overhead suspension point) during the residual stage for a 40° luff. The unshaped response is shown by the dashed line and the shaped data is shown as a solid line. The double-pendulum dynamics are clearly visible in the unshaped response. The two-mode SI shaper dramatically decreased the residual vibration amplitude.

Figure 4.47 shows the experimental and simulated residual vibration amplitudes for various luffing distances. The unshaped residual amplitude varies as the luffing distance increases. On the other hand, the shaped results are independent of the luffing distance because they are near zero for all cases. The two-mode SI shaper reduced the residual vibration amplitude by an average of 98%.

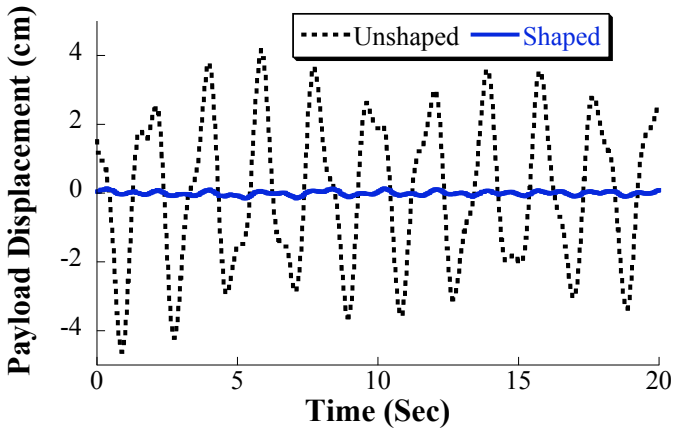

Figure 4.46: Experimental Residual Payload Displacement for 40° Luff

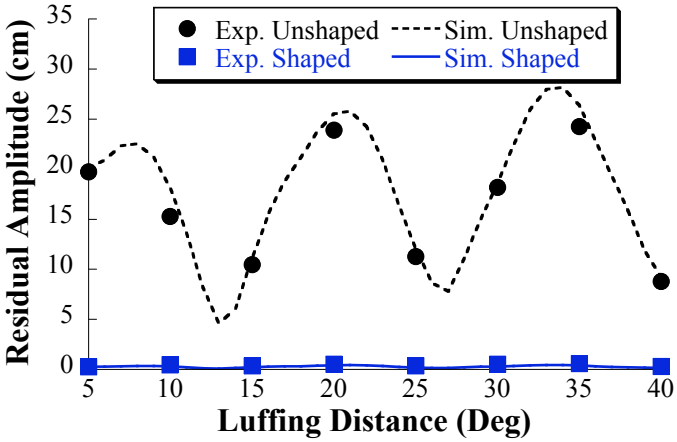

Figure 4.47: Residual Vibration Amplitude vs. Luffing Distance

The second set of experiments tested varying suspension cable lengths. Payload B was used and the initial luff angle and luffing distance were held constant at 50° and 20°, respectively. The suspension cable length was varied from 20 cm to 140 cm. Figure 4.48 shows the resulting experimental and simulated residual vibration amplitudes. There is a local minimum in the unshaped data for a suspension cable length of 40 cm. This local minimum occurs because the starting and stopping oscillations caused by the acceleration and deceleration of the unshaped command were out of phase and partially cancelled. The SI shaper was able to reduce the residual vibration amplitude by an average of 96% over the range of suspension cable lengths tested.

The final set of experiments utilized the level-luffing capabilities of the boom crane.

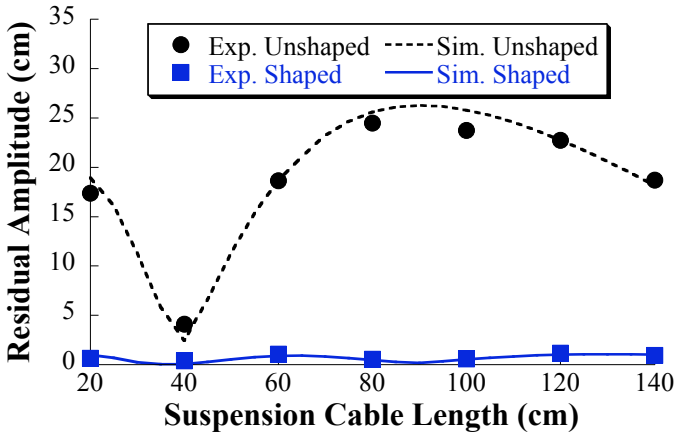

Figure 4.48: Residual Vibration Amplitude vs. Suspension Cable Length

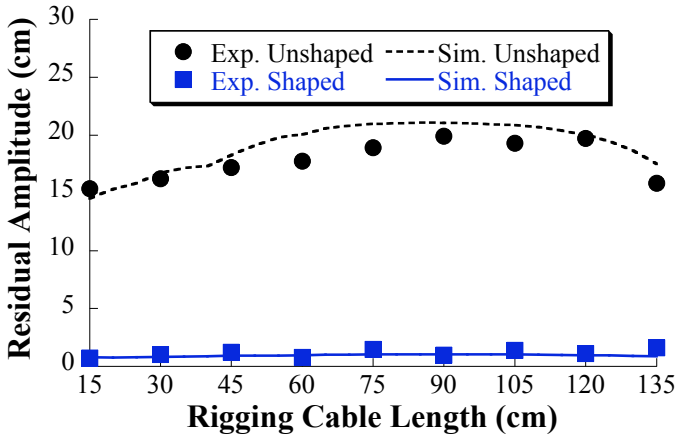

Figure 4.49: Residual Vibration Amplitude vs. Rigging Cable Length

The crane was setup to keep payload C directly above the ground. The rigging cable length was varied between 15 cm and 130 cm. The initial suspension cable length was adjusted according to the rigging cable length to place the payload directly above the ground. A luffing motion from a 50° luff angle to a 70° luff angle was performed in all the tests. Figure 4.49 shows the experimental and simulated residual vibration amplitudes. The input shaper reduced the residual amplitude by an average of 93% over the range of suspension cable lengths and rigging cable lengths tested.

Figures 4.47-4.49 demonstrate the effectiveness of the two-mode SI shaper for a large range of suspension cable lengths and double-pendulum parameters. Also, the simulated and experimental results were shown to be consistent with one another.

4.3 Operator Study

Cranes are virtually always controlled by human operators [14–16]. The performance of human operators varies greatly from one to another. Most skilled operators have years of experience; however, even their performance can vary from day to day. As a result, any controller designed for cranes should be compatible with a variety of human operators. To this end, this section presents an operator performance study on the small-scale mobile boom crane shown in Figure 2.1 in order to quantify the effectiveness of input-shaping control.

For this operator study, Specified Insensitivity (SI) shapers [40, 43] were utilized. For the single-pendulum payload, the tolerable vibration percentage, V_{tol}, was set to 5% and the frequency range from 0.35 Hz to 0.75 Hz was selected. It was assumed that the damping ratio of the payload oscillation was zero. Using the MATLAB optimization toolbox, the SI shaper times and amplitudes were obtained as:

$$\begin{bmatrix} A_i \\ t_i \end{bmatrix} = \begin{bmatrix} 0.1575 & 0.3210 & 0.0430 & 0.3210 & 0.1575 \\ 0 & 0.8937 & 1.3711 & 1.8485 & 2.7422 \end{bmatrix} \tag{4.4}$$

The frequency range selected suppresses the frequency of a single pendulum with a cable length from 0.44 m to 2 m. Although the single-pendulum cable length does not vary during the operator study, the added robustness of the SI shaper can compensate (to some degree) for the nonlinearities that exist in the driving and slewing axes of the crane.

For the double-pendulum payload, the two-mode SI shaper in (4.3) was used. This two-mode suppressing shaper is only 1 s longer than the single-mode shaper in (4.4).

Figure 4.50 shows a sketch of the obstacle course for the operator study. The crane motions were limited to driving and slewing. The operators were not required to luff or hoist. All operators began at the same starting position. The course is designed so that during the first stage, the operators use driving commands to navigate the

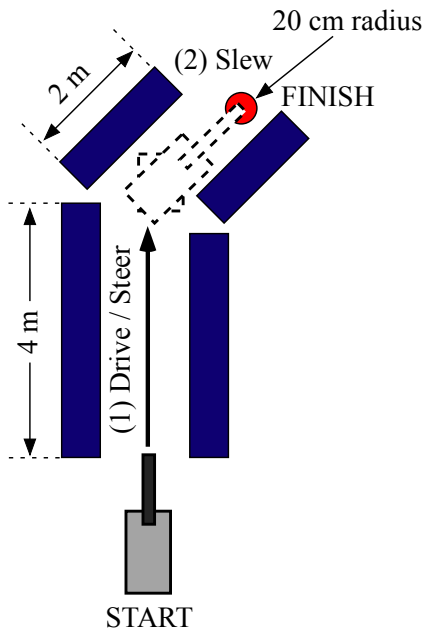

Figure 4.50: Obstacle Course

crane approximately 4 m straight through the course. During the second stage, the operators use the slewing motion to position the payload in the target zone. The target was a circle with a 20 cm radius. The task was considered complete when the payload oscillation settled completely within the target zone.

Each operator completed the course under four different conditions:

- Unshaped with a single-pendulum payload
- One-mode SI-shaped control with a single-pendulum payload
- Unshaped with a double-pendulum payload
- Two-mode SI-shaped control with a double-pendulum payload

The single-pendulum payload consisted of the suspension cable and hook. The suspension cable length and hook mass were held constant at 155 cm and 0.63 kg, respectively. To create the double-pendulum payload, an additional mass of 0.2 kg was attached to the hook with a rigging cable length of 65 cm. The suspension cable was hoisted to 90 cm so that the total length remained at 155 cm. The luffing angle was held constant at 55° for both single and double-pendulum trials. The order of

the four tests was chosen randomly for each operator.

Before the operators began the required tasks, they were provided 15 minutes of basic training in crane operation. In order to provide consistency, all operators completed the same training exercises during the same amount of time. The training tasks and their durations were:

1. Driving with both shapers - 3 minutes
2. Regular unshaped driving and slewing - 9 minutes
3. Slewing with both shapers - 3 minutes

The first training exercise familiarized the operator with the acceleration and deceleration rates of the mobile base. The second task was vital to help the operator complete the course within a reasonable amount of time using regular crane operations. The operators were taught how to manually break up their commands into multiple steps in order to reduce the payload oscillation. Task 3 was designed to familiarize the operator with the acceleration and deceleration rates of the slewing motion.

The Siemens touchscreen mobile panel shown in Figure 2.10 was used to maneuver the crane through the obstacle course. The GUI shown in Figure 2.12 was used. Because the mobile panel communicates wirelessly with the boom crane, the operator is free to walk around and stand anywhere in or around the obstacle course.

Figure 4.51(a) shows the payload (i.e. hook) position for a sample single-pendulum trial as measured by the overhead camera. Figure 4.51(b) shows the hook position for a sample double-pendulum trial. Without input shaping, the hook undergoes large oscillations that make positioning of the payload very challenging. In both cases, however, input shaping was able to substantially decrease the hook oscillation, simplifying the positioning and maneuvering of the crane. The maximum unshaped payload swing in Figure 4.51(a) is 0.53 m and the maximum shaped swing is only 0.08 m. The maximum unshaped and shaped hook swings in Figure 4.51(b) are 0.30

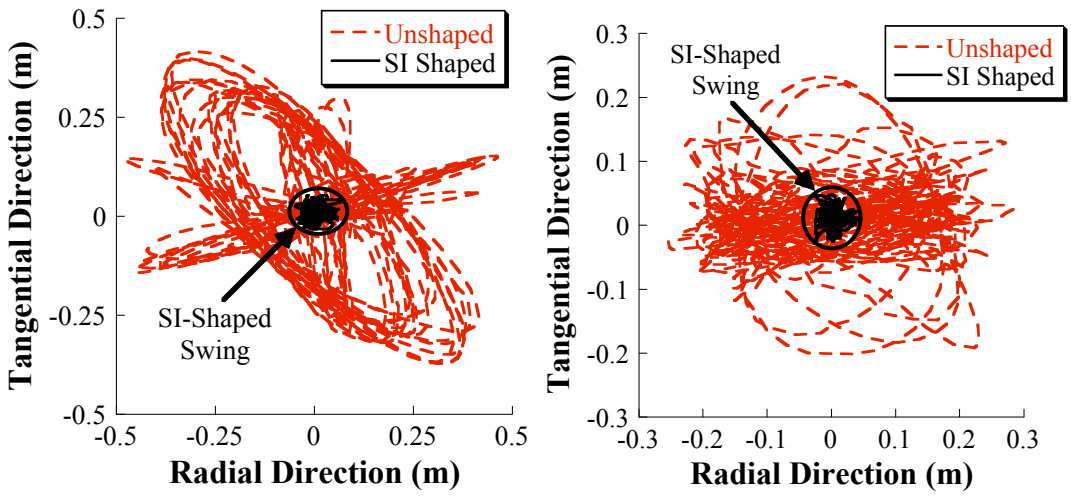

(a) Single-Pendulum Trial (b) Double-Pendulum Trial

Figure 4.51: Sample Payload/Hook Swings

m and 0.055 m, respectively. Note that Figure 4.51(b) shows the hook location, not the payload location. The camera cannot see through the hook and measure the payload position. So, the hook swing was recorded instead. The payload swing was considerably larger than the hook swing shown in the figure.

For every operator trial, the completion time, the number of button pushes, the maximum peak-to-peak residual vibration amplitude, and the number of collisions, were recorded. The completion time is the time from the first button push to when the payload oscillation has settled completely within the target zone. The number of button pushes is related to the effort the operator exerts to complete the task. The higher the number of pushes, the more effort and concentration the operator must exert in order to complete the task. The maximum residual vibration amplitude is the maximum peak-to-peak payload oscillation once the swing has settled within the target zone. For the double-pendulum payload, the maximum oscillation of the hook was measured.

Figure 4.52(a) shows the completion times for unshaped and SI-shaped single-pendulum trials for all 12 operators tested. The average completion time without shaping was 126 s. It was only 41.5 s when shaping was utilized, a 67% reduction.

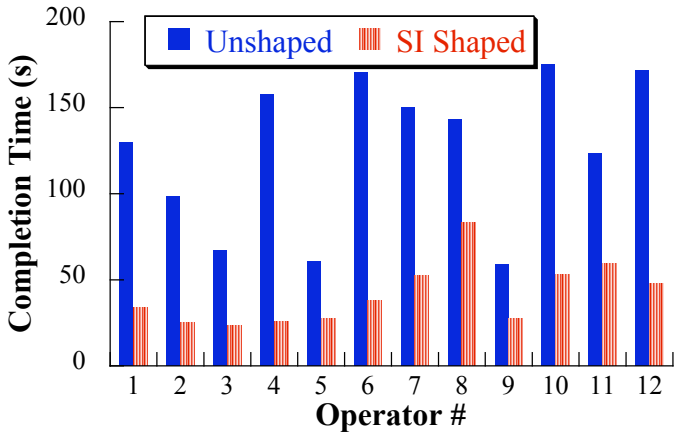

(a) Single-Pendulum

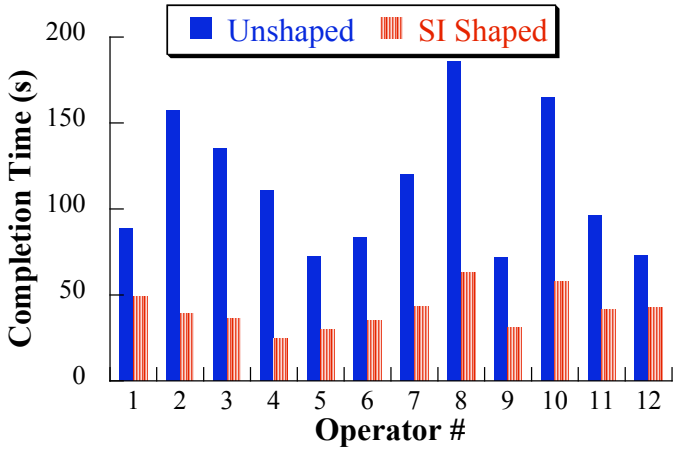

(b) Double-Pendulum

Figure 4.52: Completion Times

Operator 4 experienced the greatest improvement (84%) when SI shaping was utilized. Operator 8 experienced the least improvement (42%). Figure 4.52(b) shows the completion times for unshaped and two-mode SI shaping when the double-pendulum payload was used. The average completion time for the unshaped trials was 113 s. Input shaping reduced the average completion time to 41.2 s, a 64% reduction. Operator 4 again experienced the greatest improvement (78%) when SI shaping was utilized. Operator 12 experienced the least improvement (41%).

Figure 4.53(a) shows the number of button pushes for unshaped and SI-shaped single-pendulum trials. The average number of button pushes without shaping was 39.7 and only 12.4 with shaping, a 69% reduction. Figure 4.53(b) shows the number of

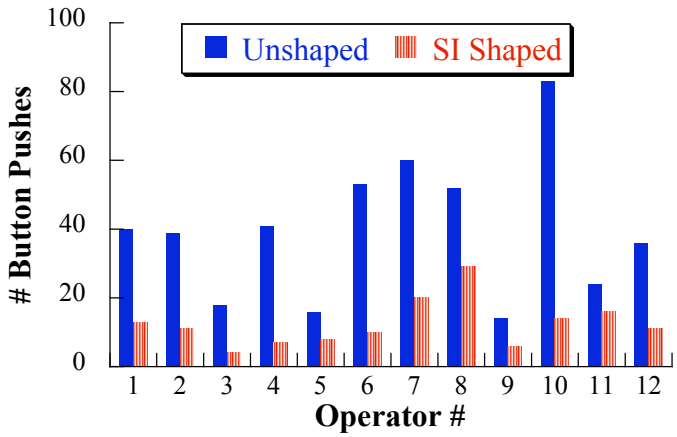

(a) Single-Pendulum

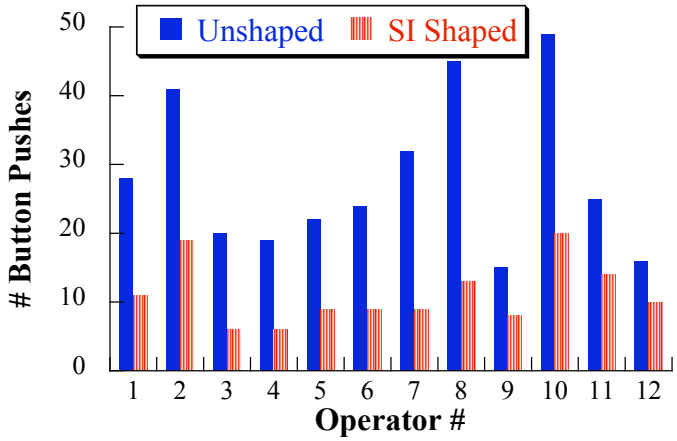

(b) Double-Pendulum

Figure 4.53: Button Pushes

button pushes for the double-pendulum trials. The average number of button pushes for the unshaped trials was 28. It was only 11.2 when input shaping was used, a 60% reduction.

Figure 4.54(a) shows the maximum residual vibration amplitude for unshaped and SI-shaped single-pendulum trials. The average maximum residual amplitude without shaping was 34.9 cm and only 7.7 cm with shaping, a 78% reduction. Figure 4.54(b) shows the maximum residual vibration amplitude for the double-pendulum trials. The average maximum residual amplitude for the unshaped trials was 18.3 cm and only 4 cm for shaped, a 78% reduction.

There were a total of 39 collisions for the unshaped trials (27 with the single

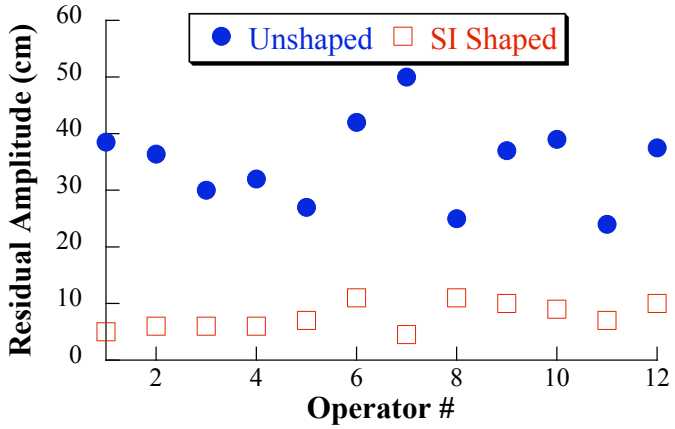

(a) Single-Pendulum

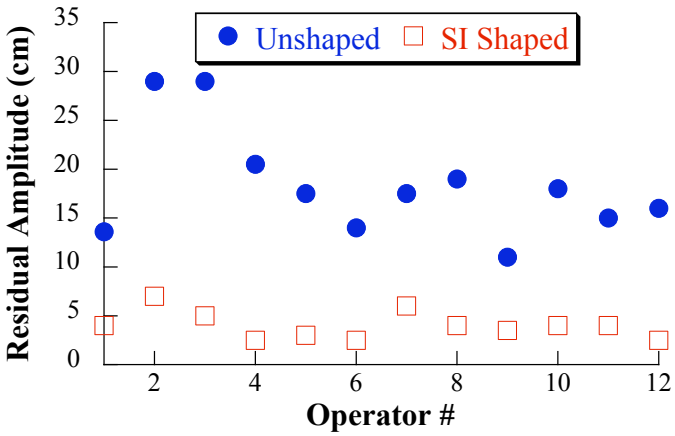

(b) Double-Pendulum

Figure 4.54: Residual Amplitude

pendulum and 12 with the double pendulum). However, there were only 3 collisions for all the shaped trials (all 3 with the double pendulum). The 3 shaped collisions occurred when operators overshot the target, whereas the unshaped collisions were caused by the large payload oscillations resulting from unshaped slewing and driving commands.

In order to determine whether the differences in the unshaped and shaped results for the single-pendulum and double-pendulum payloads are statistically significant, one-way ANOVA tests were completed for the completion time, button pushes, and maximum residual amplitude results. Table 4.2 shows the ANOVA test results.

The numbers in the second column of Table 4.2 were obtained by dividing the

Table 4.2: Summary of ANOVA Results

Trial Type	F/F_{crit}	P-value
Completion Time, SP	8.67	$3.79e^{-6}$
Completion Time, DP	8.63	$3.94e^{-6}$
Button Pushes, SP	4.48	$2.34e^{-4}$
Button Pushes, DP	5.23	$9.87e^{-5}$
Vibration Amplitude, SP	32.60	$5.14e^{-11}$
Vibration Amplitude, DP	17.17	$1.77e^{-8}$

F-values by the critical F-values obtained from one-way ANOVA tests for 95% confidence. A F/F_{crit} value greater than 1 and a small P-value indicate that the differences in the averages between the unshaped and shaped results are statistically significant. Larger F/F_{crit} ratios and smaller P-values indicate a lower probability that the difference between the unshaped and shaped results is due to random chance. The results of the ANOVA tests demonstrate that the one-mode and two-mode SI shapers were statistically successful in decreasing the completion time, lowering the number of button pushes, and reducing the maximum residual vibration amplitude.

In addition to the parameters measured, each operator was asked to fill out a questionnaire after completing all four trials. The operators were asked to qualitatively evaluate the SI shapers, to compare the single and double-pendulum trials, and to select the task that required the least effort on their part. All twelve operators stated that input shaping made the task much easier to complete. This is not surprising because with shaping, moving the crane body was approximately equivalent to moving the payload. Almost all operators also stated that the double-pendulum payload was more difficult to control than the single-pendulum, and that the shaped single-pendulum trial was the easiest of the four tasks.

CHAPTER V

STEP MODE

The boom crane is manually controlled via directional buttons on the right side of the Graphical User Interface (GUI) shown in Figure 2.9. For long moves, pushing buttons is easy and effective. However, when the payload is close to its final position, "tapping" the buttons to move the payload accurately into place can prove quite challenging. The operator has to press the buttons for a precise, short period of time to create a desired small motion. To alleviate the need for this precise timing by the operator, a step mode was developed for the motions of the boom crane [37]. Once the step mode is turned on, both short and long button pushes are converted to a short pre-designated pulse duration. This command conversion process is demonstrated in Figure 5.1 for a step-mode pulse of 200 ms.

This step mode was programmed in the programmable logic controller (PLC) of the small-scale boom crane using a timer function. The input and output parameters of the timer function are shown in Figure 5.2. The start signal of the timer was set to a button push on the GUI and the duration was set to 200 ms. Once the timer detects a button push, it outputs a move command to the corresponding motion axis for 200

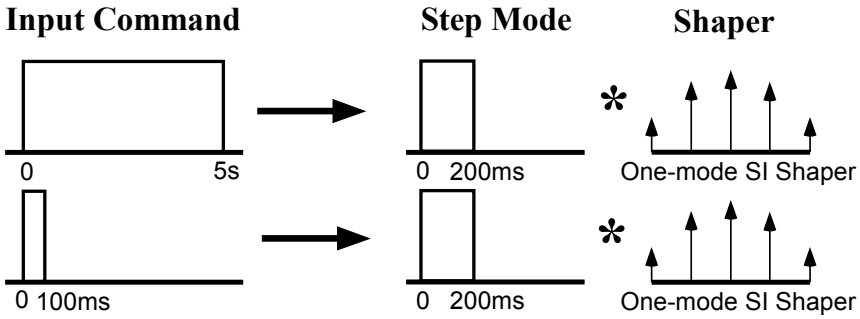

Figure 5.1: Structure of Step Mode

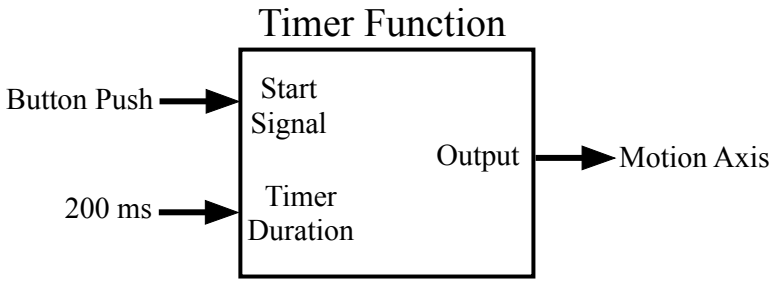

Figure 5.2: Timer Function

ms. The duration of the button push is unimportant because the timer only detects a positive change (from false to true) in the start signal. If another button push occurs within the 200 ms duration, the timer is reset, but the output to the motion axis continues without interruption. Because the timer duration is very short, tapping the directional buttons at a relatively quick rate will result in continuous motion. The motion stops 200 ms after the last button push.

There are two main advantages to such a step mode: *i)* the operator does not have to accurately "tap" the buttons to induce a short motion and *ii)* the shaper designed for the step mode can have a shorter duration. Because the step mode is designed for short motions, using a long shaper is inefficient and bothersome for the operator. Therefore, a one-mode SI shaper was designed to suppress the residual vibration in the frequency range of 0.4 Hz to 1 Hz. The impulse amplitudes and times of the step-mode shaper are:

$$\begin{bmatrix} A_i \\ t_i \end{bmatrix} = \begin{bmatrix} 0.1127 & 0.2375 & 0.2996 & 0.2375 & 0.1127 \\ 0 & 0.6478 & 1.2942 & 1.9407 & 2.5885 \end{bmatrix} \tag{5.1}$$

This frequency suppression range was selected because it covers a large range of possible single-pendulum suspension cable lengths (0.25 m to 1.6 m). This frequency range is also effective for double-pendulum payloads. The short bursts of motion that occur in step mode do not generally induce high-amplitude second-mode oscillations. To demonstrate this, the double-pendulum boom crane model was slewed using the

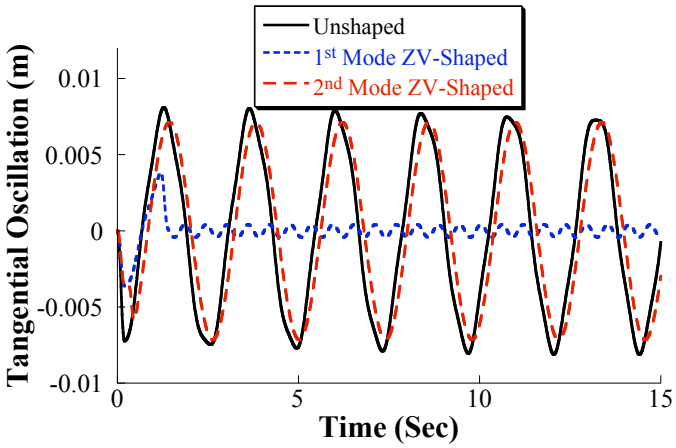

Figure 5.3: Tangential Payload Oscillation Resulting from Slewing with Step Mode [1^{st} mode = 0.42 Hz, 2^{nd} mode = 1.71 Hz]

step mode for parameters that produced first and second-mode frequencies of 0.42 Hz and 1.71 Hz, respectively. The parameters were as follows: suspension cable length of 1 m, rigging cable length of 0.5 m, hook mass of 0.63 kg, and payload mass of 2 kg. With step mode, the slewing motion results in a 0.25° turn. Figure 5.3 shows the tangential payload oscillation resulting from this test. Figure 5.3 also shows the payload response for two types of shaped commands. The first-mode shaper is a ZV shaper designed for the first-mode frequency. The second-mode shaper is a ZV shaper designed for the second-mode frequency. The first-mode shaper substantially reduces the residual oscillation (95% reduction), but the second-mode shaper is much less effective (only 12% reduction). This is because the contribution of the second mode is small compared with the contribution of the first mode.

If the suspension and rigging cable lengths are similar and the payload mass is small relative to the hook mass, then the second mode can have a significant contribution to the overall oscillation. To demonstrate this case, the parameters of the crane were modified as follows: suspension cable length of 1 m, rigging cable length of 1 m, hook mass of 0.63 kg, and payload mass of 0.05 kg. These parameters result in first and second-mode frequencies of 0.44 Hz and 0.58 Hz, respectively. Figure 5.4 shows the tangential payload oscillation for the same step-mode slewing

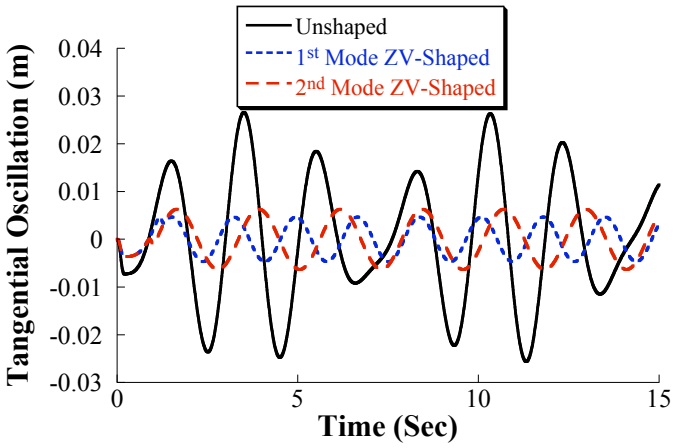

Figure 5.4: Tangential Payload Oscillation Resulting from Slewing with Step Mode [1^{st} mode = 0.44 Hz, 2^{nd} mode = 0.58 Hz]

motion. Notice that, as expected, the tangential oscillation is larger in this case. Again, two ZV shapers, each designed for one of the two frequencies, were applied to the slewing motion. The first-mode shaper is less effective (83% reduction) at reducing the residual oscillation. In addition, the second-mode shaper is almost as effective (76% reduction) as the first-mode shaper.

However, for the majority of the range of parameters that induce a large second-mode contribution, the frequency of the second mode is close to the frequency of the first mode; hence, it falls in the frequency suppression region of the 1-mode SI shaper in (5.1). For example, Figure 5.5 shows the first-mode and second-mode frequencies as a function of identical suspension cable and rigging cable lengths. The payload mass and the hook mass were kept constant at 0.05 kg and 0.63 kg, respectively. For the majority of the suspension cable and rigging cable lengths, the frequency of both modes is less than 1 Hz. The vibration frequencies do increase above 1 Hz for very small suspension cable and rigging cable length. However, small suspension cable lengths are uncommon in crane operation.

To test the effectiveness of the step mode, the payload manipulation task illustrated in Figure 5.6 was completed by an operator. The operator lowered the double-pendulum payload from its start position until the payload was as close to the target

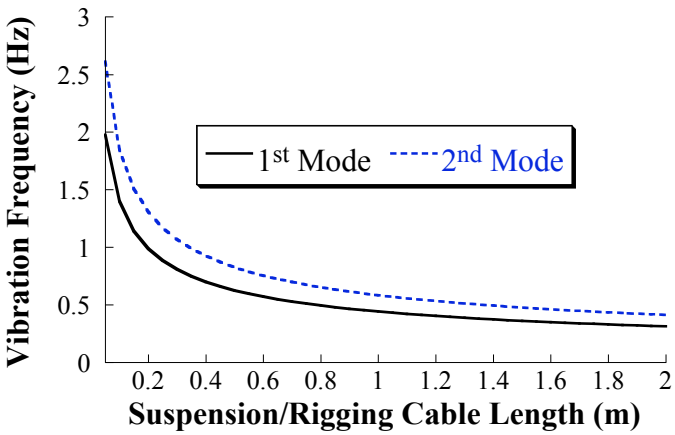

Figure 5.5: Vibration Frequency vs. Identical Suspension Cable and Rigging Cable Lengths

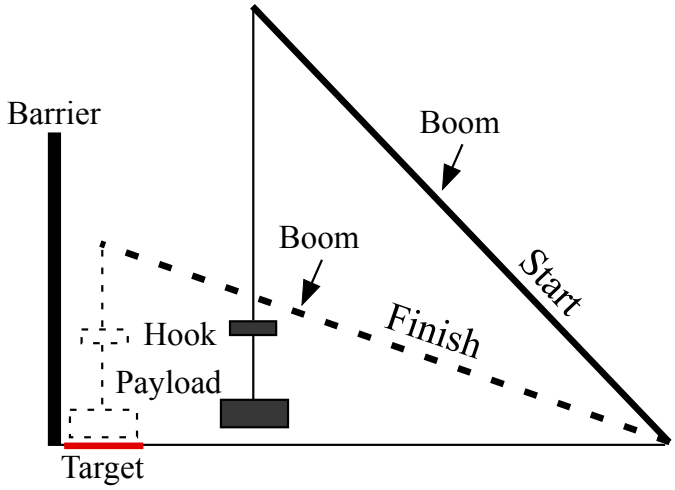

Figure 5.6: Sketch of Payload Delivery Task

as possible without colliding with the barrier. The move was a horizontal displacement of approximately 60 cm. The operator performed the task without input shaping and then again in step mode. Figure 5.7 shows the payload position during the tests. The downward drift of the payload occurs because the level luffing of the boom crane does not keep the payload perfectly level over the entire usable range of luffing angles. This vertical drift of approximately 6 cm in Figure 5.7 has been elongated to better present the horizontal oscillation of the payload.

Without input shaping, the payload collides with the target before the hook is close enough to utilize the step mode. With shaping; however, the payload was

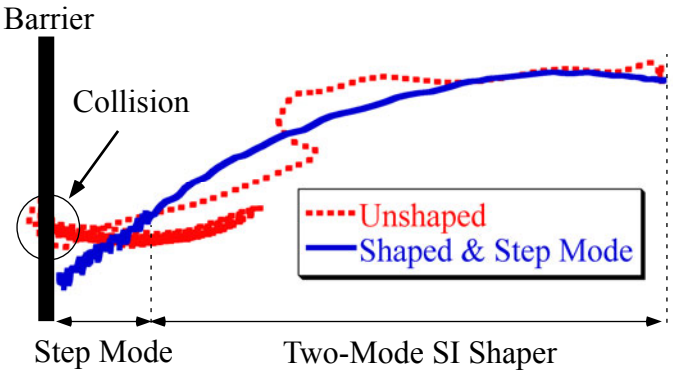

Figure 5.7: Operator Performing the Payload Delivery Task

moved the majority of the distance using the two-mode SI shaper in (4.3). Then, the payload was moved into its final position using the step mode with the one-mode SI shaper in (5.1). The payload reaches the target in a well-controlled manner and without collisions.

CHAPTER VI

CONCLUSIONS AND FUTURE WORK

6.1 Conclusions

This thesis studied the dynamics of mobile boom cranes. Boom cranes are useful and vital components of construction, manufacturing, and many other material-handling operations. However, payload oscillation inherent to boom cranes not only decreases efficiency and throughput, but can also create hazardous working conditions. Boom cranes have very complicated dynamics because of their rotational joints and swinging payloads. These nonlinear motions, coupled with a mobile base, make controlling these machines very challenging.

The dynamics of the slewing motion, the luffing motion, and the mobile base were studied and analyzed in detail. All major contributing factors to the transient and residual oscillation of the payload were presented and analyzed. It was shown that the amplitude of residual vibration does not increase with increasing move distance, but rather contains peaks and troughs and varies periodically. It was also shown that the luffing angle and the move velocity were significant in determining the vibration amplitude.

To eliminate the unwanted oscillatory dynamics of mobile boom cranes, a command-generation technique called input shaping was utilized. Input shaping modifies the input to the system in order to allow the machine to move fast, but not oscillate. Input-shaping control was shown to be very effective at reducing the transient and the residual vibration for a large range of slewing, luffing, and driving motions.

Double-pendulum dynamics were also studied and the effectiveness of input shaping on this more complex problem was quantified. A two-mode Specified-Insensitivity

shaper was designed and the shaper-design process was generalized for other applications. Then, the shaper was tested on slewing and luffing commands with double-pendulum payloads. It was shown that even given the complex double-pendulum dynamics, the two-mode Specified-Insensitivity shaper greatly reduces the payload oscillation.

A small-scale mobile boom crane was constructed to verify the simulation results. Several different experiments were performed that verified the complicated boom crane dynamics, as well as the effectiveness of input-shaping control at reducing the payload oscillation. In addition, an operator performance study was conducted that tested the compatibility of the input-shaping controller with human operators. All operators improved their performance with input shaping enabled. They were able to complete the task in less time and avoid the workspace obstacles. These improvements occurred even though the operator effort was decreased, as measured by the amount of control effort exerted by the operators.

Finally, a small-step control mode was designed to aid the operator accurately position the payload. A Specified-Insensitivity shaper was designed to eliminate the oscillation induced by the small motions. The effectiveness of the step mode was experimentally verified.

6.2 Future Work

The research presented in this thesis can be extended several different ways. One such extension is conducting additional operator performance studies. An operator study that utilizes a larger workspace and all five motion axes of the crane is one interesting possibility. The operator would have to assess the task at hand and issue commands to five different axes. Such an operator study raises questions beyond dynamics and control, such as: *i)* what is a good user interface? and *ii)* how important is operator learning?

Another extension is to implement a conversion between crane motions and actual payload movements. For example, instead of slewing and luffing to move the payload in a straight line, the operator can accomplish the same task by simply pushing one button. Then, the crane would execute the move by actuating the necessary motion axes to create the straight-line move. This would greatly simplify manual control of boom cranes.

Multi-input shaping is another possible extension. Because the mobile boom crane is redundantly actuated, a combination of moves can be used to increase speed and eliminate payload oscillation. For example, slewing can be accompanied by a luffing motion, which compensates for the radial oscillation caused by the slewing motion. Also, the slewing and luffing motions could be used to eliminate oscillations caused by driving.

APPENDIX A

SINGLE-PENDULUM MODEL

This code generates equations of motion for MATLAB simulation of a single-pendulum small-scale mobile boom crane using *Autolev*.

```
% Default settings
Autoz off     % switching off intermediate variables

% Newtonian, Bodies, Frames, Points, and Particles
Newtonian N                    % Newtonian reference system
Bodies CL, CU, B, C            % bodies with mass and inertia for carts, boom, and cable
Frames P                       % intermediate frame for defining radial hook swing
Points RA, CC, SCL, SCU, BA    % important points
Particle hook                  % hook as a point mass

% Constants
Constants mb, mc1, mc2                  % masses (boom, lower cart, upper cart)
Constants bc1, lc1, bc2, lc2, axlel     % dimensions of carts, axle-to-axle length
Constants l1, l2, l3, l4, l5, l6, l7    % distances (look at position vector section)
Constants lb, lbc, lbcom, g             % boom length, length to cable, boom COM, gravity

% Variables and Specified
Motionvariables' phi'', beta''     % motion variables for hook swings
Variables x'', y'', v', psi'', alpha'', theta'', gamma'', l''
Specified psi_ddot, v_dot, theta_ddot, gamma_ddot, l_ddot, mpay

% Auxiliary equations
psi'' = psi_ddot                   % steering angle
theta'' = theta_ddot               % slewing angle
gamma'' = gamma_ddot               % luffing angle
l'' = l_ddot                       % suspension cable length
v'=v_dot                           % linear velocity of back wheels (back-wheel drive)
x'' = DT(v*COS(alpha))             % EOM for acceleration in the x-direction
y'' = DT(v*SIN(alpha))             % EOM for acceleration in the y-direction
alpha'' = DT(v/axlel*TAN(psi))     % EOM for angular acceleration
```

```
% Masses and Inertias
Mass CL = mc1, CU = mc2, B = mb, C = 0, hook = mhook
Inertia CL, mc1/12*bc1^2, mc1/12*lc1^2, mc1/12*(lc1^2+bc1^2)     % lower cart
Inertia CU, mc2/12*bc2^2, mc2/12*lc2^2, mc2/12*(lc2^2+bc2^2)     % upper cart
Inertia B, 0, IB = mb/12*lb^2, IB                                % boom
Inertia C, 0,0,0                                                 % cable

% Position vectors
P_NO_RA> = x*N1> + y*N2>                    % N to center of rear axle
P_RA_CC> =  axlel/2*CL1>                    % center of rear axle to lower cart center
P_RA_CLO> = P_RA_CC> + l1*CL1> + l2*CL2>    % center of rear axle to lower cart COM
P_RA_SCL> = P_RA_CC> + l3*CL1> + l4*CL2>    % center of rear axle to lower cart slewing center
P_RA_SCU> = P_RA_SCL> + l5*CL3>             % center of rear axle to upper cart slewing center
P_SCU_CUO> = -l6*CU1>                       % upper cart slewing center to upper cart COM
P_SCU_BA> = l7*CU1>                         % upper cart slewing center to boom attachment
P_BA_CO> = lbc*B1>                          % boom attachment point to suspension point
P_BA_BO> = lbcom*B1>                        % boom attachment point to boom COM
P_CO_hook> = -l*C3>                         % suspension point to hook

% Rotation matrices
Simprot(N,CL,3,alpha)         % rotation of lower cart
Simprot(CL,CU,3,theta)        % rotation of upper cart (slewing)
Simprot(CU,B,2,-gamma)        % luffing of boom
Simprot(B,P,2,-phi+gamma)     % radial hook swing (front to back)
Simprot(P,C,1,beta)           % tangential hook swing (side to side)

% Angular velocities
W_CL_N> = alpha'*CL3>                              % of lower cart in N
W_CU_N> = W_CL_N> + theta'*CU3>                    % of upper cart in N
W_B_N> = W_CU_N> - gamma'*B2>                      % of boom in N
W_C_N> = W_B_N> + (-phi'+gamma')*P2> + beta'*C1>   % of cable in N

% Angular accelerations
ALF_CL_N> = DT(W_CL_N>,N)     % of lower cart in N
ALF_CU_N> = DT(W_CU_N>,N)     % of upper cart in N
ALF_B_N> = DT(W_B_N>,N)       % of boom in N
ALF_C_N> = DT(W_C_N>,N)       % of cable in N

% Hook location
x_location=l*COS(beta)*SIN(phi)     % location of hook in x-direction
```

```
y_location=l*SIN(beta)              % location of hook in y-direction
z_location=l*COS(beta)*COS(phi)     % location of hook in z-direction

% Velocities
V_RA_N>=DT(P_NO_RA>,N)                % of center of rear axle in N
V_CC_N> = DT(P_NO_CC>,N)              % of lower cart center in N
V_CLO_N> = DT(P_NO_CLO>,N)            % of lower cart center of mass in N
V_CUO_N> = DT(P_NO_CUO>,N)            % of upper cart center of mass in N
V_hook_N> = DT(P_NO_hook>,N)          % of hook in N
V2pts(N,CL,CLO,SCL)                   % of SCL in N
V2pts(N,CU,CUO,SCU)                   % of SCU in N
V2pts(N,CU,CUO,BA)                    % of BA in N
V2pts(N,B,BA,BO)                      % of boom center of mass in N
V2pts(N,B,BO,CO)                      % of suspension point in N

% Accelerations
A_RA_N> = DT(V_RA_N>,N)               % of center of rear axle in N
A_CC_N> = DT(V_CC_N>,N)               % of lower cart center in N
A_CLO_N> = DT(V_CLO_N>,N)             % of lower cart center of mass in N
A_CUO_N> = DT(V_CUO_N>,N)             % of upper cart center of mass in N
A_hook_N> = DT(V_hook_N>,N)           % of hook in N
A2pts(N,CL,CLO,SCL)                   % of SCL in N
A2pts(N,CU,CUO,SCU)                   % of SCU in N
A2pts(N,CU,CUO,BA)                    % of BA in N
A2pts(N,B,BA,BO)                      % of boom center of mass in N
A2pts(N,B,BO,CO)                      % of suspension point in N

% Forces
Gravity(-g*N3>)     % gravity force

% Equations of motion
Zero = Fr() + FrStar()
Kane()

% Generate MATLAB code for simulation
UnitSystem kg, meter, sec
Input mc1 = 25 kg, mc2= 100 kg, mb = 8.0 kg, bc1 = 0.50 m, lc1 = 0.92 m, bc2 = 0.50 m,
Input lc2 = 1.15 m, l1 = 0.0 m, l2 = 0.0 m, l3 = 0.095 m, l4 = 0.0 m, l5 = 0 m, l6 = 0.24 m,
Input l7 = 0.36 m, lb = 2 m, lbc = 1.85 m, lbcom = 1.0 m, axlel = 0.90 m, g = 9.81 m/sec^2
Output T sec, psi rad, alpha rad, theta rad, gamma rad, l m, x m, y m, psi' rad/sec,
Output alpha' rad/sec, theta' rad/sec, gamma' rad/sec, l' m/sec, x' m/sec, y' m/sec,
```

```
Output v m/sec, psi'' rad/sec^2, alpha'' rad/sec^2, theta'' rad/sec^2, gamma'' rad/sec^2,
Output l'' m/sec^2, x'' m/sec^2, y'' m/sec^2, v' m/sec^2, phi rad, beta rad, phi' rad/sec,
Output beta' rad/sec, x_location m, y_location m, z_location m
CODE Dynamics() MobileBoomCrane.m
```

APPENDIX B

DOUBLE-PENDULUM MODEL

This code generates equations of motion for MATLAB simulation of a double-pendulum small-scale mobile boom crane using *Autolev*.

```
% Default settings
Autoz off     % switching off intermediate variables

% Newtonian, Bodies, Frames, Points, and Particles
Newtonian N                    % Newtonian reference system
Bodies CL, CU, B, C, D         % bodies with mass and inertia for carts, boom, and cables
Frames P, Q                    % intermediate frame for defining radial hook/payload swings
Points RA, CC, SCL, SCU, BA    % important points
Particle hook, payload         % hook and payload as point masses

Constants mb, mc1, mc2                 % masses (boom, lower cart, upper cart)
Constants bc1, lc1, bc2, lc2, axlel    % dimensions of carts, axle-to-axle length
Constants l1, l2, l3, l4, l5, l6, l7   % distances (look at position vector section)
Constants lb, lbc, lbcom, g            % boom length, length to cable, boom COM, gravity
Constants ll, mhook                    % rigging cable length and hook mass

% Variables and Specified
Motionvariables' phi_h'', phi_p'', beta_h'', beta_p''    % hook and payload swings
Variables x'', y'', v', psi'', alpha'', theta'', gamma'', l''
Specified psi_ddot, v_dot, theta_ddot, gamma_ddot, l_ddot, mpay

% Auxiliary equations
psi'' = psi_ddot                % steering angle
theta'' = theta_ddot            % slewing angle
gamma'' = gamma_ddot            % luffing angle
l'' = l_ddot                    % suspension cable length
v'=v_dot                        % linear velocity of back wheels (back-wheel drive)
x'' = DT(v*COS(alpha))          % EOM for acceleration in the x-direction
y'' = DT(v*SIN(alpha))          % EOM for acceleration in the y-direction
alpha'' = DT(v/axlel*TAN(psi))  % EOM for angular acceleration
```

```
% Masses and Inertias
Mass CL = mc1, CU = mc2, B = mb, C = 0, D = 0, hook = mhook, payload = mpay
Inertia CL, mc1/12*bc1^2, mc1/12*lc1^2, mc1/12*(lc1^2+bc1^2)     % lower cart
Inertia CU, mc2/12*bc2^2, mc2/12*lc2^2, mc2/12*(lc2^2+bc2^2)     % upper cart
Inertia B, 0, IB = mb/12*lb^2, IB                                % boom
Inertia C, 0,0,0                                                 % suspension cable
Inertia D, 0,0,0                                                 % rigging cable

% Position vectors
P_NO_RA> = x*N1> + y*N2>                    % N to center of rear axle
P_RA_CC> =  axlel/2*CL1>                    % center of rear axle to lower cart center
P_RA_CLO> = P_RA_CC> + l1*CL1> + l2*CL2>    % center of rear axle to lower cart COM
P_RA_SCL> = P_RA_CC> + l3*CL1> + l4*CL2>    % center of rear axle to lower cart slewing center
P_RA_SCU> = P_RA_SCL> + l5*CL3>             % center of rear axle to upper cart slewing center
P_SCU_CUO> = -l6*CU1>                       % upper cart slewing center to upper cart COM
P_SCU_BA> = l7*CU1>                         % upper cart slewing center to boom attachment
P_BA_CO> = lbc*B1>                          % boom attachment point to suspension point
P_BA_BO> = lbcom*B1>                        % boom attachment point to boom COM
P_CO_hook> = -l*C3>                         % suspension point to hook
P_hook_payload> = -ll*D3>                   % hook to payload

% Rotation matrices
Simprot(N,CL,3,alpha)          % rotation of lower cart
Simprot(CL,CU,3,theta)         % rotation of upper cart (slewing)
Simprot(CU,B,2,-gamma)         % luffing of boom
Simprot(B,P,2,-phi_h+gamma)    % radial hook swing (front to back)
Simprot(P,C,1,beta_h)          % tangential hook swing (side to side)
Simprot(C,Q,2,-phi_p)          % radial payload swing (front to back)
Simprot(Q,D,1,beta_p)          % tangential payload swing (side to side)

% Angular velocities
W_CL_N> = alpha'*CL3>                                % of lower cart in N
W_CU_N> = W_CL_N> + theta'*CU3>                      % of upper cart in N
W_B_N> = W_CU_N> - gamma'*B2>                        % of boom in N
W_C_N> = W_B_N> + (-phi_h'+gamma')*P2> + beta_h'*C1>    % of suspension cable in N
W_D_N> = W_C_N> + (-phi_p')*Q2> + beta_p'*D1>        % of rigging cable in N

% Angular accelerations
ALF_CL_N> = DT(W_CL_N>,N)     % of lower cart in N
ALF_CU_N> = DT(W_CU_N>,N)     % of upper cart in N
```

```
ALF_B_N> = DT(W_B_N>,N)       % of boom in N
ALF_C_N> = DT(W_C_N>,N)       % of suspension cable in N
ALF_D_N> = DT(W_D_N>,N)       % of rigging cable in N

% Velocities
V_RA_N>=DT(P_NO_RA>,N)                % of center of rear axle in N
V_CC_N> = DT(P_NO_CC>,N)              % of lower cart center in N
V_CLO_N> = DT(P_NO_CLO>,N)            % of lower cart center of mass in N
V_CUO_N> = DT(P_NO_CUO>,N)            % of upper cart center of mass in N
V_hook_N> = DT(P_NO_hook>,N)          % of hook in N
V_payload_N> = DT(P_NO_payload>,N)    % of payload in N
V2pts(N,CL,CLO,SCL)                   % of SCL in N
V2pts(N,CU,CUO,SCU)                   % of SCU in N
V2pts(N,CU,CUO,BA)                    % of BA in N
V2pts(N,B,BA,BO)                      % of boom center of mass in N
V2pts(N,B,BO,CO)                      % of suspension point in N

% Accelerations
A_RA_N> = DT(V_RA_N>,N)              % of center of rear axle in N
A_CC_N> = DT(V_CC_N>,N)              % of lower cart center in N
A_CLO_N> = DT(V_CLO_N>,N)            % of lower cart center of mass in N
A_CUO_N> = DT(V_CUO_N>,N)            % of upper cart center of mass in N
A_hook_N> = DT(V_hook_N>,N)          % of hook in N
A_payload_N> = DT(V_payload_N>,N)    % of payload in N
A2pts(N,CL,CLO,SCL)                  % of SCL in N
A2pts(N,CU,CUO,SCU)                  % of SCU in N
A2pts(N,CU,CUO,BA)                   % of BA in N
A2pts(N,B,BA,BO)                     % of boom center of mass in N
A2pts(N,B,BO,CO)                     % of suspension point in N

% Forces
Gravity(-g*N3>)     % gravity force

% Hook and Payload Cartesian positions
hook_x = dot(express(P_CO_hook>,CU),CU1>)
hook_y = dot(express(P_CO_hook>,CU),CU2>)
payload_x = dot(express(P_CO_payload>,CU),CU1>)
payload_y = dot(express(P_CO_payload>,CU),CU2>)

% Equations of motion
Zero = Fr() + FrStar()
```

```
Kane()


% Generate MATLAB code for simulation
UnitSystem kg, meter, sec
Input mc1 = 25 kg, mc2= 100 kg, mb = 8.0 kg, bc1 = 0.50 m, lc1 = 0.92 m, bc2 = 0.50 m,
Input lc2 = 1.15 m, l1 = 0.0 m, l2 = 0.0 m, l3 = 0.095 m, l4 = 0.0 m, l5 = 0 m, l6 = 0.24 m,
Input l7 = 0.36 m, lb = 2 m, lbc = 1.85 m, lbcom = 1.0 m, axlel = 0.90 m, g = 9.81 m/sec^2, ll=0.5 m
Output T sec, psi rad, alpha rad, theta rad, gamma rad, l m, x m, y m, psi' rad/sec,
Output alpha' rad/sec, theta' rad/sec, gamma' rad/sec, l' m/sec, x' m/sec, y' m/sec,
Output v m/sec, psi'' rad/sec^2, alpha'' rad/sec^2, theta'' rad/sec^2, gamma'' rad/sec^2,
Output l'' m/sec^2, x'' m/sec^2, y'' m/sec^2, v' m/sec^2, phi_h rad, beta_h rad, phi_p rad,
Output beta_p rad, hook_x m, hook_y m, payload_x m, payload_y m
CODE Dynamics() MobileBoomCrane_DP.m
```

APPENDIX C

DOUBLE-PENDULUM EQUATIONS OF MOTION

$$0.5m_{hook}\ell_h\cos(\beta_h)(2x_{luff}\cos(\phi_h)(\dot{\alpha}+\dot{\theta})^2+2\ell_{boom}\cos(\gamma-\phi_h)(\dot{\gamma}^2+\cos(\gamma)^2(\dot{\alpha}+\dot{\theta})^2)+2\ell_h(\dot{\beta_h}+\sin(\phi_h)(\dot{\alpha}+\dot{\theta}))(\sin(\beta_h)\dot{\phi_h}+\cos(\beta_h)\cos(\phi_h)(\dot{\alpha}+\dot{\theta}))+\cos(\phi_h)\cos(\theta)((\ell_{axle}+2x_{slew})\dot{\alpha}^2+2y_{slew}\ddot{\alpha})+\sin(\theta)\cos(\phi_h)(2y_{slew}\dot{\alpha}^2-(\ell_{axle}+2x_{slew})\ddot{\alpha})+2\ell_{boom}\sin(\gamma-\phi_h)(\sin(\gamma)\cos(\gamma)(\dot{\alpha}+\dot{\theta})^2+\ddot{\gamma})-4\dot{\ell_h}(\cos(\beta_h)\dot{\phi_h}-\sin(\beta_h)\cos(\phi_h)(\dot{\alpha}+\dot{\theta}))-2\cos(\phi_h)\sin(\alpha+\theta)\ddot{y}-2\cos(\phi_h)\cos(\alpha+\theta)\ddot{x}-2\ell_h(\sin(\beta_h)\sin(\phi_h)\dot{\phi_h}(\dot{\alpha}+\dot{\theta})-\sin(\beta_h)\dot{\beta_h}\dot{\phi_h}-\cos(\beta_h)\cos(\phi_h)\dot{\beta_h}(\dot{\alpha}+\dot{\theta})-\sin(\beta_h)\cos(\phi_h)(\ddot{\alpha}+\ddot{\theta})))+0.5m_{pay}(2x_{luff}\ell_h\cos(\beta_h)\cos(\phi_h)(\dot{\alpha}+\dot{\theta})^2+2\ell_{boom}\ell_h\cos(\beta_h)\cos(\gamma-\phi_h)(\dot{\gamma}^2+\cos(\gamma)^2(\dot{\alpha}+\dot{\theta})^2)+2\ell_{boom}\ell_p(\cos(\beta_h)\cos(\beta_p)-\sin(\beta_h)\sin(\beta_p)\cos(\phi_p))(\cos(\phi_p)\cos(\gamma-\phi_h)+\sin(\phi_p)\cos(\beta_h)\sin(\gamma-\phi_h))(\dot{\gamma}^2+\cos(\gamma)^2(\dot{\alpha}+\dot{\theta})^2)+2x_{luff}\ell_p(\cos(\beta_h)\cos(\beta_p)-\sin(\beta_h)\sin(\beta_p)\cos(\phi_p))(\cos(\gamma)(\cos(\phi_p)\cos(\gamma-\phi_h)+\sin(\phi_p)\cos(\beta_h)\sin(\gamma-\phi_h))+\sin(\gamma)(\cos(\phi_p)\sin(\gamma-\phi_h)-\sin(\phi_p)\cos(\beta_h)\cos(\gamma-\phi_h)))(\dot{\alpha}+\dot{\theta})^2+2\ell_h\ell_p\sin(\phi_p)\cos(\beta_h)\dot{\phi_p}(\cos(\beta_p)\dot{\phi_p}+\sin(\beta_p)\sin(\phi_p)\dot{\beta_h}+(\cos(\beta_h)\cos(\beta_p)-\sin(\beta_h)\sin(\beta_p)\cos(\phi_p))\dot{\phi_h}-\cos(\gamma)(\sin(\beta_h)\cos(\beta_p)\cos(\gamma-\phi_h)+\sin(\beta_p)(\sin(\phi_p)\sin(\gamma-\phi_h)+\cos(\beta_h)\cos(\phi_p)\cos(\gamma-\phi_h)))(\dot{\alpha}+\dot{\theta})-\sin(\gamma)(\sin(\beta_h)\cos(\beta_p)\sin(\gamma-\phi_h)-\sin(\beta_p)(\sin(\phi_p)\cos(\gamma-\phi_h)-\cos(\beta_h)\cos(\phi_p)\sin(\gamma-\phi_h)))(\dot{\alpha}+\dot{\theta}))+2\ell_h\ell_p\sin(\phi_p)\cos(\beta_h)\cos(\beta_p)((\dot{\beta_p}+\cos(\phi_p)\dot{\beta_h}+\sin(\beta_h)\sin(\phi_p)\dot{\phi_h}+\sin(\gamma)(\cos(\phi_p)\cos(\gamma-\phi_h)+\sin(\phi_p)\cos(\beta_h)\sin(\gamma-\phi_h))(\dot{\alpha}+\dot{\theta})-\cos(\gamma)(\cos(\phi_p)\sin(\gamma-\phi_h)-\sin(\phi_p)\cos(\beta_h)\cos(\gamma-\phi_h))(\dot{\alpha}+\dot{\theta}))^2+((\cos(\beta_h)\cos(\beta_p)-\sin(\beta_h)\sin(\beta_p)\cos(\phi_p))\dot{\phi_h}-\cos(\gamma)(\sin(\beta_h)\cos(\beta_p)\cos(\gamma-\phi_h)+\sin(\beta_p)(\sin(\phi_p)\sin(\gamma-\phi_h)+\cos(\beta_h)\cos(\phi_p)\cos(\gamma-\phi_h)))(\dot{\alpha}+\dot{\theta})-\sin(\gamma)(\sin(\beta_h)\cos(\beta_p)\sin(\gamma-\phi_h)-\sin(\beta_p)(\sin(\phi_p)\cos(\gamma-\phi_h)-\cos(\beta_h)\cos(\phi_p)\sin(\gamma-\phi_h)))(\dot{\alpha}+\dot{\theta}))(\cos(\beta_p)\dot{\phi_p}+\sin(\beta_p)\sin(\phi_p)\dot{\beta_h}+(\cos(\beta_h)\cos(\beta_p)-\sin(\beta_h)\sin(\beta_p)\cos(\phi_p))\dot{\phi_h}-\cos(\gamma)(\sin(\beta_h)\cos(\beta_p)\cos(\gamma-\phi_h)+\sin(\beta_p)(\sin(\phi_p)\sin(\gamma-\phi_h)+\cos(\beta_h)\cos(\phi_p)\cos(\gamma-\phi_h)))(\dot{\alpha}+\dot{\theta})-\sin(\gamma)(\sin(\beta_h)\cos(\beta_p)\sin(\gamma-\phi_h)-\sin(\beta_p)(\sin(\phi_p)\cos(\gamma-\phi_h)-\cos(\beta_h)\cos(\phi_p)\sin(\gamma-\phi_h)))(\dot{\alpha}+\dot{\theta}))+\ell_h\cos(\beta_h)\cos(\phi_h)\cos(\theta)((\ell_{axle}+2x_{slew})\dot{\alpha}^2+2y_{slew}\ddot{\alpha})+\ell_h\sin(\theta)\cos(\beta_h)\cos(\phi_h)(2y_{slew}\dot{\alpha}^2-(\ell_{axle}+2x_{slew})\ddot{\alpha})+2\ell_{boom}\ell_h\cos(\beta_h)\sin(\gamma-\phi_h)(\sin(\gamma)\cos(\gamma)(\dot{\alpha}+\dot{\theta})^2+\ddot{\gamma})+2\ell_{boom}\ell_p(\cos(\beta_h)\cos(\beta_p)-\sin(\beta_h)\sin(\beta_p)\cos(\phi_p))(\cos(\phi_p)\sin(\gamma-\phi_h)-\sin(\phi_p)\cos(\beta_h)\cos(\gamma-\phi_h))(\sin(\gamma)\cos(\gamma)(\dot{\alpha}+\dot{\theta})^2+\ddot{\gamma})+2\ell_h\cos(\beta_h)(\ell_h(\dot{\beta_h}+\sin(\phi_h)(\dot{\alpha}+\dot{\theta}))(\sin(\beta_h)\dot{\phi_h}+\cos(\beta_h)\cos(\phi_h)(\dot{\alpha}+\dot{\theta}))-2\dot{\ell_h}(\cos(\beta_h)\dot{\phi_h}-\sin(\beta_h)\cos(\phi_h)(\dot{\alpha}+\dot{\theta}))-\ell_h(\sin(\beta_h)\sin(\phi_h)\dot{\phi_h}(\dot{\alpha}+\dot{\theta})-\sin(\beta_h)\dot{\beta_h}\dot{\phi_h}-\cos(\beta_h)\cos(\phi_h)\dot{\beta_h}(\dot{\alpha}+\dot{\theta})-\sin(\beta_h)\cos(\phi_h)(\ddot{\alpha}+\ddot{\theta})))+\ell_p(\cos(\beta_h)\cos(\beta_p)-\sin(\beta_h)\sin(\beta_p)\cos(\phi_p))(\sin(\beta_h)\sin(\phi_p)\sin(\theta)+\cos(\theta)(\cos(\gamma)(\cos(\phi_p)\cos(\gamma-\phi_h)+\sin(\phi_p)\cos(\beta_h)\sin(\gamma-\phi_h))+\sin(\gamma)(\cos(\phi_p)\sin(\gamma-\phi_h)-\sin(\phi_p)\cos(\beta_h)\cos(\gamma-\phi_h))))((\ell_{axle}+2x_{slew})\dot{\alpha}^2+2y_{slew}\ddot{\alpha})+2\ell_p\cos(\phi_p)(\cos(\beta_h)\cos(\beta_p)-\sin(\beta_h)\sin(\beta_p)\cos(\phi_p))(\ell_h(\dot{\beta_h}+\sin(\phi_h)(\dot{\alpha}+\dot{\theta}))(\sin(\beta_h)\dot{\phi_h}+\cos(\beta_h)\cos(\phi_h)(\dot{\alpha}+\dot{\theta}))-2\dot{\ell_h}(\cos(\beta_h)\dot{\phi_h}-\sin(\beta_h)\cos(\phi_h)(\dot{\alpha}+\dot{\theta}))-\ell_h(\sin(\beta_h)\sin(\phi_h)\dot{\phi_h}(\dot{\alpha}+\dot{\theta})-\sin(\beta_h)\dot{\beta_h}\dot{\phi_h}-\cos(\beta_h)\cos(\phi_h)\dot{\beta_h}(\dot{\alpha}+\dot{\theta})-\sin(\beta_h)\cos(\phi_h)(\ddot{\alpha}+\ddot{\theta}))+\ell_p\sin(\beta_h)\sin(\phi_p)(\cos(\theta)(\cos(\beta_h)\cos(\beta_p)-\sin(\beta_h)\sin(\beta_p)\cos(\phi_p))-\sin(\theta)(\sin(\gamma)(\sin(\beta_p)\sin(\phi_p)\sin(\gamma-\phi_h)+\cos(\gamma-\phi_h)(\sin(\beta_h)\cos(\beta_p)+\sin(\beta_p)\cos(\beta_h)\cos(\phi_p)))+\cos(\gamma)(\sin(\beta_p)\sin(\phi_p)\cos(\gamma-\phi_h)-\sin(\gamma-\phi_h)(\sin(\beta_h)\cos(\beta_p)+\sin(\beta_p)\cos(\beta_h)\cos(\phi_p)))))(2y_{slew}\dot{\alpha}^2-(\ell_{axle}+2x_{slew})\ddot{\alpha})+2\ell_p\sin(\beta_h)\sin(\phi_p)\cos(\beta_p)(\ell_p\sin(\phi_p)\dot{\beta_h}(\cos(\beta_p)\dot{\phi_p}+\sin(\beta_p)\sin(\phi_p)\dot{\beta_h}+(\cos(\beta_h)\cos(\beta_p)-\sin(\beta_h)\sin(\beta_p)\cos(\phi_p))\dot{\phi_h}-\cos(\gamma)(\sin(\beta_h)\cos(\beta_p)\cos(\gamma-\phi_h)+\sin(\beta_p)(\sin(\phi_p)\sin(\gamma-\phi_h)+\cos(\beta_h)\cos(\phi_p)\cos(\gamma-\phi_h)))(\dot{\alpha}+\dot{\theta})-\sin(\gamma)(\sin(\beta_h)\cos(\beta_p)\sin(\gamma-\phi_h)-\sin(\beta_p)(\sin(\phi_p)\cos(\gamma-\phi_h)-\cos(\beta_h)\cos(\phi_p)\sin(\gamma-\phi_h)))(\dot{\alpha}+\dot{\theta}))-2\dot{\ell_h}(\dot{\beta_h}+\sin(\phi_h)(\dot{\alpha}+\dot{\theta}))-\ell_h\sin(\beta_h)\dot{\gamma}(\cos(\beta_h)\dot{\phi_h}-\sin(\beta_h)\cos(\phi_h)(\dot{\alpha}+\dot{\theta}))-\ell_h(\cos(\phi_h)\dot{\phi_h}(\dot{\alpha}+\dot{\theta})+\sin(\phi_h)(\ddot{\alpha}+\ddot{\theta})))+2\ell_p\sin(\beta_h)\sin(\phi_p)(\cos(\alpha)(\sin(\theta)(\cos(\beta_h)\cos(\beta_p)-\sin(\beta_h)\sin(\beta_p)\cos(\phi_p))+\cos(\theta)(\sin(\gamma)(\sin(\beta_p)\sin(\phi_p)\sin(\gamma-\phi_h)+\cos(\gamma-\phi_h)(\sin(\beta_h)\cos(\beta_p)+\sin(\beta_p)\cos(\beta_h)\cos(\phi_p)))+\cos(\gamma)(\sin(\beta_p)\sin(\phi_p)\cos(\gamma-\phi_h)-\sin(\gamma-\phi_h)(\sin(\beta_h)\cos(\beta_p)+\sin(\beta_p)\cos(\beta_h)\cos(\phi_p)))))+\sin(\alpha)(\cos(\theta)(\cos(\beta_h)\cos(\beta_p)-\sin(\beta_h)\sin(\beta_p)\cos(\phi_p))-\sin(\theta)(\sin(\gamma)(\sin(\beta_p)\sin(\phi_p)\sin(\gamma-\phi_h)+\cos(\gamma-\phi_h)(\sin(\beta_h)\cos(\beta_p)+\sin(\beta_p)\cos(\beta_h)\cos(\phi_p)))+\cos(\gamma)(\sin(\beta_p)\sin(\phi_p)\cos(\gamma-\phi_h)-\sin(\gamma-\phi_h)(\sin(\beta_h)\cos(\beta_p)+\sin(\beta_p)\cos(\beta_h)\cos(\phi_p)))))\ddot{x}+2\ell_p\sin(\beta_h)\sin(\phi_p)(\sin(\alpha)(\sin(\theta)(\cos(\beta_h)\cos(\beta_p)-\sin(\beta_h)\sin(\beta_p)\cos(\phi_p))+\cos(\theta)(\sin(\gamma)(\sin(\beta_p)\sin(\phi_p)\sin(\gamma-\phi_h)+\cos(\gamma-\phi_h)(\sin(\beta_h)\cos(\beta_p)+\sin(\beta_p)\cos(\beta_h)\cos(\phi_p)))+\cos(\gamma)(\sin(\beta_p)\sin(\phi_p)\cos(\gamma-\phi_h)-\sin(\gamma-\phi_h)(\sin(\beta_h)\cos(\beta_p)+\sin(\beta_p)\cos(\beta_h)\cos(\phi_p)))))+\cos(\alpha)(\cos(\theta)(\cos(\beta_h)\cos(\beta_p)-\sin(\beta_h)\sin(\beta_p)\cos(\phi_p))-\sin(\theta)(\sin(\gamma)(\sin(\beta_p)\sin(\phi_p)\sin(\gamma-\phi_h)+\cos(\gamma-\phi_h)(\sin(\beta_h)\cos(\beta_p)+\sin(\beta_p)\cos(\beta_h)\cos(\phi_p)))+\cos(\gamma)(\sin(\beta_p)\sin(\phi_p)\cos(\gamma-\phi_h)-\sin(\gamma-\phi_h)(\sin(\beta_h)\cos(\beta_p)+\sin(\beta_p)\cos(\beta_h)\cos(\phi_p)))))\ddot{y}+2\ell_h\ell_p\sin(\beta_p)\sin(\phi_p)\cos(\beta_h)(\sin(\beta_h)\cos(\phi_p)\dot{\phi_h}\dot{\phi_p}+\sin(\phi_p)\cos(\beta_h)\dot{\beta_h}\dot{\phi_h}+\sin(\gamma)(\dot{\alpha}+\dot{\theta})(\cos(\phi_p)\sin(\gamma-\phi_h)\dot{\phi_h}+\cos(\beta_h)\cos(\phi_p)\sin(\gamma-\phi_h)\dot{\phi_p}-\sin(\phi_p)\cos(\gamma-\phi_h)\dot{\phi_p}-\sin(\beta_h)\sin(\phi_p)\sin(\gamma-\phi_h)\dot{\beta_h}-\sin(\phi_p)\cos(\beta_h)\cos(\gamma-\phi_h)(\dot{\phi_h}-\dot{\gamma}))+((\sin(\beta_p)\cos(\beta_h)+\sin(\beta_h)\cos(\beta_p)\cos(\phi_p))\dot{\phi_h}-\sin(\gamma)(\sin(\beta_h)\sin(\beta_p)\sin(\gamma-\phi_h)+\cos(\beta_p)(\sin(\phi_p)\cos(\gamma-\phi_h)-\cos(\beta_h)\cos(\phi_p)\sin(\gamma-\phi_h)))(\dot{\alpha}+\dot{\theta})-\cos(\gamma)(\sin(\beta_h)\sin(\beta_p)\cos(\gamma-\phi_h)-\cos(\beta_p)(\sin(\phi_p)\sin(\gamma-\phi_h)+\cos(\beta_h)\cos(\phi_p)\cos(\gamma-\phi_h)))(\dot{\alpha}+\dot{\theta})(\cos(\beta_p)\dot{\phi_p}+\sin(\beta_p)\sin(\phi_p)\dot{\beta_h}+(\cos(\beta_h)\cos(\beta_p)-\sin(\beta_h)\sin(\beta_p)\cos(\phi_p))\dot{\phi_h}-\cos(\gamma)(\sin(\beta_h)\cos(\beta_p)\cos(\gamma-\phi_h)+\sin(\beta_p)(\sin(\phi_p)\sin(\gamma-\phi_h)+\cos(\beta_h)\cos(\phi_p)\cos(\gamma-\phi_h)))(\dot{\alpha}+\dot{\theta})-\sin(\gamma)(\sin(\beta_h)\cos(\beta_p)\sin(\gamma-\phi_h)-\sin(\beta_p)(\sin(\phi_p)\cos(\gamma-\phi_h)-\cos(\beta_h)\cos(\phi_p)\sin(\gamma-\phi_h)))(\dot{\alpha}+\dot{\theta}))+\sin(\gamma)(\cos(\phi_p)\cos(\gamma-\phi_h)+\sin(\phi_p)\cos(\beta_h)\sin(\gamma-\phi_h))(\ddot{\alpha}+\ddot{\theta})-\sin(\phi_p)\dot{\beta_h}\dot{\phi_p}-\sin(\phi_h)\sin(\phi_p)\cos(\beta_h)\dot{\gamma}(\dot{\alpha}+\dot{\theta})-\cos(\gamma)(\dot{\alpha}+\dot{\theta})(\sin(\beta_h)\sin(\phi_p)\cos(\gamma-\phi_h)\dot{\beta_h}-\sin(\phi_p)\sin(\gamma-\phi_h)\dot{\phi_p}-$$

$$\cos(\phi_p)\cos(\gamma-\phi_h)\dot{\phi_h}-\cos(\beta_h)\cos(\phi_p)\cos(\gamma-\phi_h)\dot{\phi_p}-\sin(\phi_p)\cos(\beta_h)\sin(\gamma-\phi_h)(\dot{\phi_h}-\dot{\gamma}))-\cos(\gamma)(\cos(\phi_p)\sin(\gamma-\phi_h)-\sin(\phi_p)\cos(\beta_h)\cos(\gamma-\phi_h))(\ddot{\alpha}+\ddot{\theta}))-2\ell_h\ell_p\sin(\beta_h)\sin(\phi_p)(\sin(\beta_h)\cos(\beta_p)+\sin(\beta_p)\cos(\beta_h)\cos(\phi_p))(\dot{\phi_h}-\dot{\gamma})(\cos(\beta_h)\dot{\phi_h}-\sin(\beta_h)\cos(\phi_h)(\dot{\alpha}+\dot{\theta}))-2\ell_h\ell_p\sin(\phi_p)\cos(\beta_h)(\cos(\beta_h)\cos(\beta_p)-\sin(\beta_h)\sin(\beta_p)\cos(\phi_p))(\dot{\phi_h}-\dot{\gamma})(\cos(\beta_h)\dot{\phi_h}-\sin(\beta_h)\cos(\phi_h)(\dot{\alpha}+\dot{\theta}))-2\ell_{boom}\ell_p\sin(\beta_h)\sin(\phi_p)(\sin(\beta_p)\sin(\phi_p)\cos(\gamma-\phi_h)-\sin(\gamma-\phi_h)(\sin(\beta_h)\cos(\beta_p)+\sin(\beta_p)\cos(\beta_h)\cos(\phi_p)))(\dot{\gamma}^2+\cos(\gamma)^2(\dot{\alpha}+\dot{\theta})^2)-2x_{luff}\ell_p\sin(\beta_h)\sin(\phi_p)(\sin(\gamma)(\sin(\beta_p)\sin(\phi_p)\sin(\gamma-\phi_h)+\cos(\gamma-\phi_h)(\sin(\beta_h)\cos(\beta_p)+\sin(\beta_p)\cos(\beta_h)\cos(\phi_p)))+\cos(\gamma)(\sin(\beta_p)\sin(\phi_p)\cos(\gamma-\phi_h)-\sin(\gamma-\phi_h)(\sin(\beta_h)\cos(\beta_p)+\sin(\beta_p)\cos(\beta_h)\cos(\phi_p))))(\dot{\alpha}+\dot{\theta})^2-2\ell_p^2\sin(\beta_h)\sin(\beta_p)\sin(\phi_p)\dot{\phi_p}(\cos(\beta_p)\dot{\phi_p}+\sin(\beta_p)\sin(\phi_p)\dot{\beta_h}+(\cos(\beta_h)\cos(\beta_p)-\sin(\beta_h)\sin(\beta_p)\cos(\phi_p))\dot{\phi_h}-\cos(\gamma)(\sin(\beta_h)\cos(\beta_p)\cos(\gamma-\phi_h)+\sin(\beta_p)(\sin(\phi_p)\sin(\gamma-\phi_h)+\cos(\beta_h)\cos(\phi_p)\cos(\gamma-\phi_h)))(\dot{\alpha}+\dot{\theta})-\sin(\gamma)(\sin(\beta_h)\cos(\beta_p)\sin(\gamma-\phi_h)-\sin(\beta_p)(\sin(\phi_p)\cos(\gamma-\phi_h)-\cos(\beta_h)\cos(\phi_p)\sin(\gamma-\phi_h)))(\dot{\alpha}+\dot{\theta}))-2\ell_h\cos(\beta_h)\cos(\phi_h)\sin(\alpha+\theta)\ddot{y}-2\ell_h\cos(\beta_h)\cos(\phi_h)\cos(\alpha+\theta)\ddot{x}-2\ell_p\sin(\beta_h)\sin(\beta_p)\sin(\phi_p)\cos(\phi_p)(\ell_h(\dot{\beta_h}+\sin(\phi_h)(\dot{\alpha}+\dot{\theta}))^2+\ell_h\cos(\beta_h)\dot{\gamma}(\cos(\beta_h)\dot{\phi_h}-\sin(\beta_h)\cos(\phi_h)(\dot{\alpha}+\dot{\theta}))-\ddot{\ell_h})-2\ell_{boom}\ell_p\sin(\beta_h)\sin(\phi_p)(\sin(\beta_p)\sin(\phi_p)\sin(\gamma-\phi_h)+\cos(\gamma-\phi_h)(\sin(\beta_h)\cos(\beta_p)+\sin(\beta_p)\cos(\beta_h)\cos(\phi_p)))(\sin(\gamma)\cos(\gamma)(\dot{\alpha}+\dot{\theta})^2+\ddot{\gamma})-2\ell_p\sin(\phi_p)(\cos(\beta_h)\cos(\beta_p)-\sin(\beta_h)\sin(\beta_p)\cos(\phi_p))(\ell_h(\dot{\beta_h}+\sin(\phi_h)(\dot{\alpha}+\dot{\theta}))^2+\ell_h\cos(\beta_h)\dot{\gamma}(\cos(\beta_h)\dot{\phi_h}-\sin(\beta_h)\cos(\phi_h)(\dot{\alpha}+\dot{\theta}))-\ddot{\ell_h})-\ell_p(\cos(\beta_h)\cos(\beta_p)-\sin(\beta_h)\sin(\beta_p)\cos(\phi_p))(\sin(\beta_h)\sin(\phi_p)\cos(\theta)-\sin(\theta)(\cos(\gamma)(\cos(\phi_p)\cos(\gamma-\phi_h)+\sin(\phi_p)\cos(\beta_h)\sin(\gamma-\phi_h))+\sin(\gamma)(\cos(\phi_p)\sin(\gamma-\phi_h)-\sin(\phi_p)\cos(\beta_h)\cos(\gamma-\phi_h))))(2y_{slew}\dot{\alpha}^2-(\ell_{axle}+2x_{slew})\ddot{\alpha})-2\ell_p\sin(\beta_h)\sin(\beta_p)\sin(\phi_p)^2(\ell_h(\dot{\beta_h}+\sin(\phi_h)(\dot{\alpha}+\dot{\theta}))(\sin(\beta_h)\dot{\phi_h}+\cos(\beta_h)\cos(\phi_h)(\dot{\alpha}+\dot{\theta}))-2\dot{\ell_h}(\cos(\beta_h)\dot{\phi_h}-\sin(\beta_h)\cos(\phi_h)(\dot{\alpha}+\dot{\theta}))-\ell_h(\sin(\beta_h)\sin(\phi_h)\dot{\phi_h}(\dot{\alpha}+\dot{\theta})-\sin(\beta_h)\dot{\beta_h}\dot{\phi_h}-\cos(\beta_h)\cos(\phi_h)\dot{\beta_h}(\dot{\alpha}+\dot{\theta})-\sin(\beta_h)\cos(\phi_h)(\ddot{\alpha}+\ddot{\theta})))-\ell_p\sin(\beta_h)\sin(\phi_p)(\sin(\theta)(\cos(\beta_h)\cos(\beta_p)-\sin(\beta_h)\sin(\beta_p)\cos(\phi_p))+\cos(\theta)(\sin(\gamma)(\sin(\beta_p)\sin(\phi_p)\sin(\gamma-\phi_h)+\cos(\gamma-\phi_h)(\sin(\beta_h)\cos(\beta_p)+\sin(\beta_p)\cos(\beta_h)\cos(\phi_p)))+\cos(\gamma)(\sin(\beta_p)\sin(\phi_p)\cos(\gamma-\phi_h)-\sin(\gamma-\phi_h)(\sin(\beta_h)\cos(\beta_p)+\sin(\beta_p)\cos(\beta_h)\cos(\phi_p)))))((\ell_{axle}+2x_{slew})\dot{\alpha}^2+2y_{slew}\ddot{\alpha})-2\ell_p(\cos(\beta_h)\cos(\beta_p)-\sin(\beta_h)\sin(\beta_p)\cos(\phi_p))(\cos(\alpha)(\sin(\beta_h)\sin(\phi_p)\sin(\theta)+\cos(\theta)(\cos(\gamma)(\cos(\phi_p)\cos(\gamma-\phi_h)+\sin(\phi_p)\cos(\beta_h)\sin(\gamma-\phi_h))+\sin(\gamma)(\cos(\phi_p)\sin(\gamma-\phi_h)-\sin(\phi_p)\cos(\beta_h)\cos(\gamma-\phi_h))))+\sin(\alpha)(\sin(\beta_h)\sin(\phi_p)\cos(\theta)-\sin(\theta)(\cos(\gamma)(\cos(\phi_p)\cos(\gamma-\phi_h)+\sin(\phi_p)\cos(\beta_h)\sin(\gamma-\phi_h))+\sin(\gamma)(\cos(\phi_p)\sin(\gamma-\phi_h)-\sin(\phi_p)\cos(\beta_h)\cos(\gamma-\phi_h)))))\ddot{x}-2\ell_p(\cos(\beta_h)\cos(\beta_p)-\sin(\beta_h)\sin(\beta_p)\cos(\phi_p))(\sin(\alpha)(\sin(\beta_h)\sin(\phi_p)\sin(\theta)+\cos(\theta)(\cos(\gamma)(\cos(\phi_p)\cos(\gamma-\phi_h)+\sin(\phi_p)\cos(\beta_h)\sin(\gamma-\phi_h))+\sin(\gamma)(\cos(\phi_p)\sin(\gamma-\phi_h)-\sin(\phi_p)\cos(\beta_h)\cos(\gamma-\phi_h))))-\cos(\alpha)(\sin(\beta_h)\sin(\phi_p)\cos(\theta)-\sin(\theta)(\cos(\gamma)(\cos(\phi_p)\cos(\gamma-\phi_h)+\sin(\phi_p)\cos(\beta_h)\sin(\gamma-\phi_h))+\sin(\gamma)(\cos(\phi_p)\sin(\gamma-\phi_h)-\sin(\phi_p)\cos(\beta_h)\cos(\gamma-\phi_h)))))\ddot{y}-2\ell_p^2\sin(\beta_h)\sin(\phi_p)(\sin(\beta_h)\cos(\phi_p)\dot{\phi_h}\dot{\phi_p}+\sin(\phi_p)\cos(\beta_h)\dot{\beta_h}\dot{\phi_h}+\sin(\gamma)(\dot{\alpha}+\dot{\theta})(\cos(\phi_p)\sin(\gamma-\phi_h)\dot{\phi_h}+\cos(\beta_h)\cos(\phi_p)\sin(\gamma-\phi_h)\dot{\phi_p}-\sin(\phi_p)\cos(\gamma-\phi_h)\dot{\phi_p}-\sin(\beta_h)\sin(\phi_p)\sin(\gamma-\phi_h)\dot{\beta_h}-\sin(\phi_p)\cos(\beta_h)\cos(\gamma-\phi_h)(\dot{\phi_h}-\dot{\gamma}))+((\sin(\beta_p)\cos(\beta_h)+\sin(\beta_h)\cos(\beta_p)\cos(\phi_p))\dot{\phi_h}-\sin(\gamma)(\sin(\beta_h)\sin(\beta_p)\sin(\gamma-\phi_h)+\cos(\beta_p)(\sin(\phi_p)\cos(\gamma-\phi_h)-\cos(\beta_h)\cos(\phi_p)\sin(\gamma-\phi_h)))(\dot{\alpha}+\dot{\theta})-\cos(\gamma)(\sin(\beta_h)\sin(\beta_p)\cos(\gamma-\phi_h)-\cos(\beta_p)(\sin(\phi_p)\sin(\gamma-\phi_h)+\cos(\beta_h)\cos(\phi_p)\cos(\gamma-\phi_h)))(\dot{\alpha}+\dot{\theta}))(\cos(\beta_p)\dot{\phi_p}+\sin(\beta_p)\sin(\phi_p)\dot{\beta_h}+(\cos(\beta_h)\cos(\beta_p)-\sin(\beta_h)\sin(\beta_p)\cos(\phi_p))\dot{\phi_h}-\cos(\gamma)(\sin(\beta_h)\cos(\beta_p)\cos(\gamma-\phi_h)+\sin(\beta_p)(\sin(\phi_p)\sin(\gamma-\phi_h)+\cos(\beta_h)\cos(\phi_p)\cos(\gamma-\phi_h)))(\dot{\alpha}+\dot{\theta})-\sin(\gamma)(\sin(\beta_h)\cos(\beta_p)\sin(\gamma-\phi_h)-\sin(\beta_p)(\sin(\phi_p)\cos(\gamma-\phi_h)-\cos(\beta_h)\cos(\phi_p)\sin(\gamma-\phi_h)))(\dot{\alpha}+\dot{\theta}))+\sin(\gamma)(\cos(\phi_p)\cos(\gamma-\phi_h)+\sin(\phi_p)\cos(\beta_h)\sin(\gamma-\phi_h))(\ddot{\alpha}+\ddot{\theta})-\sin(\phi_p)\dot{\beta_h}\dot{\phi_p}-\sin(\phi_h)\sin(\phi_p)\cos(\beta_h)\dot{\gamma}(\dot{\alpha}+\dot{\theta})-\cos(\gamma)(\dot{\alpha}+\dot{\theta})(\sin(\beta_h)\sin(\phi_p)\cos(\gamma-\phi_h)\dot{\beta_h}-\sin(\phi_p)\sin(\gamma-\phi_h)\dot{\phi_p}-\cos(\phi_p)\cos(\gamma-\phi_h)\dot{\phi_h}-\cos(\beta_h)\cos(\phi_p)\cos(\gamma-\phi_h)\dot{\phi_p}-\sin(\phi_p)\cos(\beta_h)\sin(\gamma-\phi_h)(\dot{\phi_h}-\dot{\gamma}))-\cos(\gamma)(\cos(\phi_p)\sin(\gamma-\phi_h)-\sin(\phi_p)\cos(\beta_h)\cos(\gamma-\phi_h))(\ddot{\alpha}+\ddot{\theta}))-2\ell_h\ell_p\cos(\beta_h)\cos(\phi_p)(\sin(\beta_p)\cos(\phi_p)\dot{\beta_h}\dot{\phi_p}+\sin(\phi_p)\cos(\beta_p)\dot{\beta_h}\dot{\beta_p}+\dot{\phi_h}(\sin(\beta_h)\sin(\beta_p)\sin(\phi_p)\dot{\phi_p}-\sin(\beta_h)\cos(\beta_p)\dot{\beta_h}-\sin(\beta_p)\cos(\beta_h)\dot{\beta_p}-\sin(\beta_h)\cos(\beta_p)\cos(\phi_p)\dot{\beta_p}-\sin(\beta_p)\cos(\beta_h)\cos(\phi_p)\dot{\beta_h})+\sin(\beta_p)\sin(\phi_h)\cos(\beta_h)\cos(\phi_p)\dot{\gamma}(\dot{\alpha}+\dot{\theta})-\sin(\beta_p)\dot{\beta_p}\dot{\phi_p}-\cos(\gamma)(\dot{\alpha}+\dot{\theta})(\sin(\beta_h)\cos(\beta_p)\sin(\gamma-\phi_h)\dot{\phi_h}+\cos(\beta_h)\cos(\beta_p)\cos(\gamma-\phi_h)\dot{\beta_h}+\cos(\beta_p)(\sin(\phi_p)\sin(\gamma-\phi_h)+\cos(\beta_h)\cos(\phi_p)\cos(\gamma-\phi_h))\dot{\beta_p}-\sin(\beta_h)\sin(\beta_p)\cos(\gamma-\phi_h)\dot{\beta_p}-\sin(\beta_p)(\sin(\phi_p)\cos(\gamma-\phi_h)\dot{\phi_h}+\sin(\beta_h)\cos(\beta_p)\cos(\gamma-\phi_h)\dot{\beta_h}+\sin(\phi_p)\cos(\beta_h)\sin(\gamma-\phi_h)\dot{\phi_p}+\cos(\beta_h)\cos(\phi_p)\cos(\gamma-\phi_h)(\dot{\phi_h}-\dot{\gamma})))-(\dot{\beta_p}+\cos(\phi_p)\dot{\beta_h}+\sin(\beta_h)\sin(\phi_p)\dot{\phi_h}+\sin(\gamma)(\cos(\phi_p)\cos(\gamma-\phi_h)+\sin(\phi_p)\cos(\beta_h)\sin(\gamma-\phi_h))(\dot{\alpha}+\dot{\theta})-\cos(\gamma)(\cos(\phi_p)\sin(\gamma-\phi_h)-\sin(\phi_p)\cos(\beta_h)\cos(\gamma-\phi_h))(\dot{\alpha}+\dot{\theta}))(\sin(\beta_p)\dot{\phi_p}+(\sin(\beta_p)\cos(\beta_h)+\sin(\beta_h)\cos(\beta_p)\cos(\phi_p))\dot{\phi_h}-\sin(\phi_p)\cos(\beta_p)\dot{\beta_h}-\sin(\gamma)(\sin(\beta_h)\sin(\beta_p)\sin(\gamma-\phi_h)+\cos(\beta_p)(\sin(\phi_p)\cos(\gamma-\phi_h)-\cos(\beta_h)\cos(\phi_p)\sin(\gamma-\phi_h)))(\dot{\alpha}+\dot{\theta})-\cos(\gamma)(\sin(\beta_h)\sin(\beta_p)\cos(\gamma-\phi_h)-\cos(\beta_p)(\sin(\phi_p)\sin(\gamma-\phi_h)+\cos(\beta_h)\cos(\phi_p)\cos(\gamma-\phi_h)))(\dot{\alpha}+\dot{\theta}))-\cos(\gamma)(\sin(\beta_h)\cos(\beta_p)\cos(\gamma-\phi_h)+\sin(\beta_p)(\sin(\phi_p)\sin(\gamma-\phi_h)+\cos(\beta_h)\cos(\phi_p)\cos(\gamma-\phi_h)))(\ddot{\alpha}+\ddot{\theta})-\sin(\gamma)(\sin(\beta_h)\cos(\beta_p)\sin(\gamma-\phi_h)-\sin(\beta_p)(\sin(\phi_p)\cos(\gamma-\phi_h)-\cos(\beta_h)\cos(\phi_p)\sin(\gamma-\phi_h)))(\ddot{\alpha}+\ddot{\theta}))-2\ell_p^2(\cos(\beta_h)\cos(\beta_p)-\sin(\beta_h)\sin(\beta_p)\cos(\phi_p))(\sin(\beta_p)\cos(\phi_p)\dot{\beta_h}\dot{\phi_p}+\sin(\phi_p)\cos(\beta_p)\dot{\beta_h}\dot{\beta_p}+\dot{\phi_h}(\sin(\beta_h)\sin(\beta_p)\sin(\phi_p)\dot{\phi_p}-\sin(\beta_h)\cos(\beta_p)\dot{\beta_h}-\sin(\beta_p)\cos(\beta_h)\dot{\beta_p}-\sin(\beta_h)\cos(\beta_p)\cos(\phi_p)\dot{\beta_p}-\sin(\beta_p)\cos(\beta_h)\cos(\phi_p)\dot{\beta_h})+\sin(\beta_p)\sin(\phi_h)\cos(\beta_h)\cos(\phi_p)\dot{\gamma}(\dot{\alpha}+\dot{\theta})-\sin(\beta_p)\dot{\beta_p}\dot{\phi_p}-\cos(\gamma)(\dot{\alpha}+\dot{\theta})(\sin(\beta_h)\cos(\beta_p)\sin(\gamma-\phi_h)\dot{\phi_h}+\cos(\beta_h)\cos(\beta_p)\cos(\gamma-\phi_h)\dot{\beta_h}+\cos(\beta_p)(\sin(\phi_p)\sin(\gamma-\phi_h)+\cos(\beta_h)\cos(\phi_p)\cos(\gamma-\phi_h))\dot{\beta_p}-\sin(\beta_h)\sin(\beta_p)\cos(\gamma-\phi_h)\dot{\beta_p}-\sin(\beta_p)(\sin(\phi_p)\cos(\gamma-\phi_h)\dot{\phi_h}+\sin(\beta_h)\cos(\beta_p)\cos(\gamma-\phi_h)\dot{\beta_h}+\sin(\phi_p)\cos(\beta_h)\cos(\gamma-\phi_h)\dot{\phi_p}-\cos(\phi_p)\sin(\gamma-\phi_h)\dot{\phi_p}-\cos(\beta_h)\cos(\phi_p)\sin(\gamma-\phi_h)(\dot{\phi_h}-\dot{\gamma})))-\sin(\gamma)(\dot{\alpha}+\dot{\theta})(\cos(\beta_h)\cos(\beta_p)\sin(\gamma-\phi_h)\dot{\beta_h}-\sin(\beta_h)\sin(\beta_p)\sin(\gamma-\phi_h)\dot{\beta_p}-\sin(\beta_h)\cos(\beta_p)\cos(\gamma-\phi_h)\dot{\phi_h}-\cos(\beta_p)(\sin(\phi_p)\cos(\gamma-\phi_h)-\cos(\beta_h)\cos(\phi_p)\sin(\gamma-\phi_h))\dot{\beta_p}-\sin(\beta_p)(\sin(\phi_p)\sin(\gamma-\phi_h)\dot{\phi_h}+\cos(\phi_p)\cos(\gamma-\phi_h)\dot{\phi_p}+\sin(\beta_h)\cos(\phi_p)\sin(\gamma-\phi_h)\dot{\beta_h}+\sin(\phi_p)\cos(\beta_h)\cos(\gamma-\phi_h)\dot{\phi_p}+\cos(\beta_h)\cos(\phi_p)\cos(\gamma-\phi_h)(\dot{\phi_h}-\dot{\gamma})))-(\dot{\beta_p}+\cos(\phi_p)\dot{\beta_h}+\sin(\beta_h)\sin(\phi_p)\dot{\phi_h}+\sin(\gamma)(\cos(\phi_p)\cos(\gamma-\phi_h)+\sin(\phi_p)\cos(\beta_h)\sin(\gamma-\phi_h))(\dot{\alpha}+\dot{\theta})-\cos(\gamma)(\cos(\phi_p)\sin(\gamma-\phi_h)-\sin(\phi_p)\cos(\beta_h)\cos(\gamma-\phi_h))(\dot{\alpha}+\dot{\theta}))(\sin(\beta_p)\dot{\phi_p}+(\sin(\beta_p)\cos(\beta_h)+\sin(\beta_h)\cos(\beta_p)\cos(\phi_p))\dot{\phi_h}-\sin(\phi_p)\cos(\beta_p)\dot{\beta_h}-\sin(\gamma)(\sin(\beta_h)\sin(\beta_p)\sin(\gamma-\phi_h)+\cos(\beta_p)(\sin(\phi_p)\cos(\gamma-\phi_h)-\cos(\beta_h)\cos(\phi_p)\sin(\gamma-\phi_h)))(\dot{\alpha}+\dot{\theta})-\cos(\gamma)(\sin(\beta_h)\sin(\beta_p)\cos(\gamma-\phi_h)-\cos(\beta_p)(\sin(\phi_p)\sin(\gamma-\phi_h)+\cos(\beta_h)\cos(\phi_p)\cos(\gamma-\phi_h)))(\dot{\alpha}+\dot{\theta}))-\cos(\gamma)(\sin(\beta_h)\cos(\beta_p)\cos(\gamma-\phi_h)+\sin(\beta_p)(\sin(\phi_p)\sin(\gamma-\phi_h)+\cos(\beta_h)\cos(\phi_p)\cos(\gamma-\phi_h)))(\ddot{\alpha}+\ddot{\theta})-\sin(\gamma)(\sin(\beta_h)\cos(\beta_p)\sin(\gamma-\phi_h)-\sin(\beta_p)(\sin(\phi_p)\cos(\gamma-\phi_h)-\cos(\beta_h)\cos(\phi_p)\sin(\gamma-\phi_h)))(\ddot{\alpha}+\ddot{\theta}))-2\ell_p^2(\cos(\beta_h)\cos(\beta_p)-\sin(\beta_h)\sin(\beta_p)\cos(\phi_p))(\sin(\beta_p)\cos(\phi_p)\dot{\beta_h}\dot{\phi_p}+\sin(\phi_p)\cos(\beta_p)\dot{\beta_h}\dot{\beta_p}+\dot{\phi_h}(\sin(\beta_h)\sin(\beta_p)\sin(\phi_p)\dot{\phi_p}-\sin(\beta_h)\cos(\beta_p)\dot{\beta_h}-\sin(\beta_p)\cos(\beta_h)\dot{\beta_p}-\sin(\beta_h)\cos(\beta_p)\cos(\phi_p)\dot{\beta_p}-\sin(\beta_p)\cos(\beta_h)\cos(\phi_p)\dot{\beta_h})+\sin(\beta_p)\sin(\phi_h)\cos(\beta_h)\cos(\phi_p)\dot{\gamma}(\dot{\alpha}+\dot{\theta})-\sin(\beta_p)\dot{\beta_p}\dot{\phi_p}-\cos(\gamma)(\dot{\alpha}+\dot{\theta})(\sin(\beta_h)\cos(\beta_p)\sin(\gamma-\phi_h)\dot{\phi_h}+\cos(\beta_h)\cos(\beta_p)\cos(\gamma-\phi_h)\dot{\beta_h}+\cos(\beta_p)(\sin(\phi_p)\sin(\gamma-\phi_h)+\cos(\beta_h)\cos(\phi_p)\cos(\gamma-\phi_h))\dot{\beta_p}-\sin(\beta_h)\sin(\beta_p)\cos(\gamma-\phi_h)\dot{\beta_p}-\sin(\beta_p)(\sin(\phi_p)\cos(\gamma-\phi_h)\dot{\phi_h}+\sin(\beta_h)\cos(\phi_p)\cos(\gamma-\phi_h)\dot{\beta_h}+\sin(\phi_p)\cos(\beta_h)\cos(\gamma-\phi_h)\dot{\phi_p}-\cos(\phi_p)\sin(\gamma-\phi_h)\dot{\phi_p}-\cos(\beta_h)\cos(\phi_p)\sin(\gamma-\phi_h)(\dot{\phi_h}-\dot{\gamma})))-\sin(\gamma)(\dot{\alpha}+\dot{\theta})(\cos(\beta_h)\cos(\beta_p)\sin(\gamma-\phi_h)\dot{\beta_h}-\sin(\beta_h)\sin(\beta_p)\sin(\gamma-\phi_h)\dot{\beta_p}-\sin(\beta_h)\cos(\beta_p)\cos(\gamma-\phi_h)\dot{\phi_h}-\cos(\beta_p)(\sin(\phi_p)\cos(\gamma-\phi_h)-\cos(\beta_h)\cos(\phi_p)\sin(\gamma-\phi_h))\dot{\beta_p}-\sin(\beta_p)(\sin(\phi_p)\sin(\gamma-\phi_h)\dot{\phi_h}+\cos(\phi_p)\cos(\gamma-\phi_h)\dot{\phi_p}+\sin(\beta_h)\cos(\phi_p)\sin(\gamma-\phi_h)\dot{\beta_h}+\sin(\phi_p)\cos(\beta_h)\cos(\gamma-\phi_h)\dot{\phi_p}-\cos(\phi_p)\sin(\gamma-\phi_h)\dot{\phi_p}-\cos(\beta_h)\cos(\phi_p)\sin(\gamma-\phi_h)(\dot{\phi_h}-\dot{\gamma})))-(\dot{\beta_p}+\cos(\phi_p)\dot{\beta_h}+\sin(\beta_h)\sin(\phi_p)\dot{\phi_h}+\sin(\gamma)(\cos(\phi_p)\cos(\gamma-\phi_h)+\sin(\phi_p)\cos(\beta_h)\sin(\gamma-\phi_h))(\dot{\alpha}+\dot{\theta})-\cos(\gamma)(\cos(\phi_p)\sin(\gamma-\phi_h)-\sin(\phi_p)\cos(\beta_h)\cos(\gamma-\phi_h))(\dot{\alpha}+\dot{\theta}))(\sin(\beta_p)\dot{\phi_p}+(\sin(\beta_p)\cos(\beta_h)+\sin(\beta_h)\cos(\beta_p)\cos(\phi_p))\dot{\phi_h}-\sin(\phi_p)\cos(\beta_p)\dot{\beta_h}-\sin(\gamma)(\sin(\beta_h)\sin(\beta_p)\sin(\gamma-\phi_h)+\cos(\beta_p)(\sin(\phi_p)\cos(\gamma-\phi_h)-\cos(\beta_h)\cos(\phi_p)\sin(\gamma-\phi_h)))(\dot{\alpha}+\dot{\theta})-\cos(\gamma)(\sin(\beta_h)\sin(\beta_p)\cos(\gamma-\phi_h)-\cos(\beta_p)(\sin(\phi_p)\sin(\gamma-\phi_h)+\cos(\beta_h)\cos(\phi_p)\cos(\gamma-\phi_h)))(\dot{\alpha}+\dot{\theta}))-\cos(\gamma)(\sin(\beta_h)\cos(\beta_p)\cos(\gamma-\phi_h)+\sin(\beta_p)(\sin(\phi_p)\sin(\gamma-\phi_h)$$

$$+\cos(\beta_h)\cos(\phi_p)\cos(\gamma-\phi_h)))(\ddot{\alpha}+\ddot{\theta})-\sin(\gamma)(\sin(\beta_h)\cos(\beta_p)\sin(\gamma-\phi_h)-\sin(\beta_p)(\sin(\phi_p)\cos(\gamma-\phi_h)-\cos(\beta_h)\cos(\phi_p)\sin(\gamma-\phi_h)))(\ddot{\alpha}+\ddot{\theta}))-gm_{hook}\ell_h\sin(\phi_h)\cos(\beta_h)-gm_{pay}(\ell_h\sin(\phi_h)\cos(\beta_h)+\ell_p(\cos(\beta_h)\cos(\beta_p)-\sin(\beta_h)\sin(\beta_p)\cos(\phi_p))(\sin(\gamma)(\cos(\phi_p)\cos(\gamma-\phi_h)+\sin(\phi_p)\cos(\beta_h)\sin(\gamma-\phi_h))-\cos(\gamma)(\cos(\phi_p)\sin(\gamma-\phi_h)-\sin(\phi_p)\cos(\beta_h)\cos(\gamma-\phi_h)))+\ell_p\sin(\beta_h)\sin(\phi_p)(\cos(\gamma)(\sin(\beta_p)\sin(\phi_p)\sin(\gamma-\phi_h)+\cos(\gamma-\phi_h)(\sin(\beta_h)\cos(\beta_p)+\sin(\beta_p)\cos(\beta_h)\cos(\phi_p)))-\sin(\gamma)(\sin(\beta_p)\sin(\phi_p)\cos(\gamma-\phi_h)-\sin(\gamma-\phi_h)(\sin(\beta_h)\cos(\beta_p)+\sin(\beta_p)\cos(\beta_h)\cos(\phi_p)))))-\ell_p m_{pay}\sin(\phi_p)(\ell_p\sin(\beta_h)-\ell_h\sin(\beta_p)\cos(\beta_h))\ddot{\beta_p}-\ell_p m_{pay}\cos(\beta_p)(\ell_h\cos(\beta_h)\cos(\phi_p)+\ell_p(\cos(\beta_h)\cos(\beta_p)-\sin(\beta_h)\sin(\beta_p)\cos(\phi_p)))\ddot{\phi_p}-\ell_p m_{pay}\sin(\phi_p)(\ell_p\sin(\beta_h)\cos(\phi_p)+\ell_h\sin(\beta_h)\cos(\beta_p)+\ell_p\sin(\beta_p)(\cos(\beta_h)\cos(\beta_p)-\sin(\beta_h)\sin(\beta_p)\cos(\phi_p)))\ddot{\beta_h}-(m_{hook}\ell_h^2\cos(\beta_h)^2-m_{pay}(2\ell_h\ell_p\sin(\beta_h)\sin(\beta_p)\cos(\beta_h)+\sin(\beta_h)^2(\ell_h^2-\ell_p^2\sin(\phi_p)^2)-\ell_h^2-2\ell_h\ell_p\cos(\beta_p)\cos(\phi_p)\cos(\beta_h)^2-\ell_p^2(\cos(\beta_h)\cos(\beta_p)-\sin(\beta_h)\sin(\beta_p)\cos(\phi_p))^2))\ddot{\phi_h}=0$$

$$0.5\ell_p m_{pay}\cos(\beta_p)(2\ell_{boom}(\cos(\phi_p)\cos(\gamma-\phi_h)+\sin(\phi_p)\cos(\beta_h)\sin(\gamma-\phi_h))(\dot{\gamma}^2+\cos(\gamma)^2(\dot{\alpha}+\dot{\theta})^2)+2x_{luff}(\cos(\gamma)(\cos(\phi_p)\cos(\gamma-\phi_h)+\sin(\phi_p)\cos(\beta_h)\sin(\gamma-\phi_h))+\sin(\gamma)(\cos(\phi_p)\sin(\gamma-\phi_h)-\sin(\phi_p)\cos(\beta_h)\cos(\gamma-\phi_h)))(\dot{\alpha}+\dot{\theta})^2+2x_{luff}\sin(\beta_h)\sin(\phi_p)(\ddot{\alpha}+\ddot{\theta})+2\ell_{boom}(\cos(\phi_p)\sin(\gamma-\phi_h)-\sin(\phi_p)\cos(\beta_h)\cos(\gamma-\phi_h))(\sin(\gamma)\cos(\gamma)(\dot{\alpha}+\dot{\theta})^2+\ddot{\gamma})+(\sin(\beta_h)\sin(\phi_p)\sin(\theta)+\cos(\theta)(\cos(\gamma)(\cos(\phi_p)\cos(\gamma-\phi_h)+\sin(\phi_p)\cos(\beta_h)\sin(\gamma-\phi_h))+\sin(\gamma)(\cos(\phi_p)\sin(\gamma-\phi_h)-\sin(\phi_p)\cos(\beta_h)\cos(\gamma-\phi_h))))((\ell_{axle}+2x_{slew})\dot{\alpha}^2+2y_{slew}\ddot{\alpha})+2\cos(\phi_p)(\ell_h(\dot{\beta_h}+\sin(\phi_h)(\dot{\alpha}+\dot{\theta}))(\sin(\beta_h)\dot{\phi_h}+\cos(\beta_h)\cos(\phi_h)(\dot{\alpha}+\dot{\theta}))-2\dot{\ell_h}(\cos(\beta_h)\dot{\phi_h}-\sin(\beta_h)\cos(\phi_h)(\dot{\alpha}+\dot{\theta}))-\ell_h(\sin(\beta_h)\sin(\phi_h)\dot{\phi_h}(\dot{\alpha}+\dot{\theta})-\sin(\beta_h)\dot{\beta_h}\dot{\phi_h}-\cos(\beta_h)\cos(\phi_h)\dot{\beta_h}(\dot{\alpha}+\dot{\theta})-\sin(\beta_h)\cos(\phi_h)(\ddot{\alpha}+\ddot{\theta}))-2g(\sin(\gamma)(\cos(\phi_p)\cos(\gamma-\phi_h)+\sin(\phi_p)\cos(\beta_h)\sin(\gamma-\phi_h))-\cos(\gamma)(\cos(\phi_p)\sin(\gamma-\phi_h)-\sin(\phi_p)\cos(\beta_h)\cos(\gamma-\phi_h)))-2\ell_h\sin(\phi_p)\cos(\beta_h)\dot{\phi_h}(\cos(\beta_h)\dot{\phi_h}-2\sin(\beta_h)\cos(\phi_h)(\dot{\alpha}+\dot{\theta}))-2\ell_p\cos(\beta_p)\dot{\phi_p}-2\ell_p\sin(\beta_p)\sin(\phi_p)\dot{\beta_h}-2(\ell_h\cos(\beta_h)\cos(\phi_p)+\ell_p(\cos(\beta_h)\cos(\beta_p)-\sin(\beta_h)\sin(\beta_p)\cos(\phi_p)))\ddot{\phi_h}-2\sin(\phi_p)(\ell_h(\dot{\beta_h}+\sin(\phi_h)(\dot{\alpha}+\dot{\theta}))^2-\ddot{\ell_h})-2\sin(\beta_h)\sin(\phi_p)(2\ell_{boom}\sin(\gamma)\dot{\gamma}(\dot{\alpha}+\dot{\theta})+\ell_h\sin(\beta_h)\cos(\phi_h)^2(\dot{\alpha}+\dot{\theta})^2-\ell_{boom}\cos(\gamma)(\ddot{\alpha}+\ddot{\theta}))-(\sin(\beta_h)\sin(\phi_p)\cos(\theta)-\sin(\theta)(\cos(\gamma)(\cos(\phi_p)\cos(\gamma-\phi_h)+\sin(\phi_p)\cos(\beta_h)\sin(\gamma-\phi_h))+\sin(\gamma)(\cos(\phi_p)\sin(\gamma-\phi_h)-\sin(\phi_p)\cos(\beta_h)\cos(\gamma-\phi_h))))(2y_{slew}\dot{\alpha}^2-(\ell_{axle}+2x_{slew})\ddot{\alpha})-2(\cos(\alpha)(\sin(\beta_h)\sin(\phi_p)\sin(\theta)+\cos(\theta)(\cos(\gamma)(\cos(\phi_p)\cos(\gamma-\phi_h)+\sin(\phi_p)\cos(\beta_h)\sin(\gamma-\phi_h))+\sin(\gamma)(\cos(\phi_p)\sin(\gamma-\phi_h)-\sin(\phi_p)\cos(\beta_h)\cos(\gamma-\phi_h))))+\sin(\alpha)(\sin(\beta_h)\sin(\phi_p)\cos(\theta)-\sin(\theta)(\cos(\gamma)(\cos(\phi_p)\cos(\gamma-\phi_h)+\sin(\phi_p)\cos(\beta_h)\sin(\gamma-\phi_h))+\sin(\gamma)(\cos(\phi_p)\sin(\gamma-\phi_h)-\sin(\phi_p)\cos(\beta_h)\cos(\gamma-\phi_h))))\ddot{x}-2(\sin(\alpha)(\sin(\beta_h)\sin(\phi_p)\sin(\theta)+\cos(\theta)(\cos(\gamma)(\cos(\phi_p)\cos(\gamma-\phi_h)+\sin(\phi_p)\cos(\beta_h)\sin(\gamma-\phi_h))+\sin(\gamma)(\cos(\phi_p)\sin(\gamma-\phi_h)-\sin(\phi_p)\cos(\beta_h)\cos(\gamma-\phi_h))))-\cos(\alpha)(\sin(\beta_h)\sin(\phi_p)\cos(\theta)-\sin(\theta)(\cos(\gamma)(\cos(\phi_p)\cos(\gamma-\phi_h)+\sin(\phi_p)\cos(\beta_h)\sin(\gamma-\phi_h))+\sin(\gamma)(\cos(\phi_p)\sin(\gamma-\phi_h)-\sin(\phi_p)\cos(\beta_h)\cos(\gamma-\phi_h))))\ddot{y}-2\ell_p(\sin(\beta_p)\cos(\phi_p)\dot{\beta_h}\dot{\phi_p}+\sin(\phi_p)\cos(\beta_p)\dot{\beta_h}\dot{\beta_p}+\dot{\phi_h}(\sin(\beta_h)\sin(\beta_p)\sin(\phi_p)\dot{\phi_p}-\sin(\beta_h)\cos(\beta_p)\dot{\beta_h}-\sin(\beta_p)\cos(\beta_h)\dot{\beta_p}-\sin(\beta_h)\cos(\beta_p)\cos(\phi_p)\dot{\beta_p}-\sin(\beta_p)\cos(\beta_h)\cos(\phi_p)\dot{\beta_h})+\sin(\beta_p)\sin(\phi_h)\cos(\beta_h)\cos(\phi_p)\dot{\gamma}(\dot{\alpha}+\dot{\theta})-\sin(\beta_p)\dot{\beta_p}\dot{\phi_p}-\cos(\gamma)(\dot{\alpha}+\dot{\theta})(\sin(\beta_h)\cos(\beta_p)\sin(\gamma-\phi_h)\dot{\phi_h}+\cos(\beta_h)\cos(\beta_p)\cos(\gamma-\phi_h)\dot{\beta_h}+\cos(\beta_p)(\sin(\phi_p)\sin(\gamma-\phi_h)+\cos(\beta_h)\cos(\phi_p)\cos(\gamma-\phi_h))\dot{\beta_p}-\sin(\beta_h)\sin(\beta_p)\cos(\gamma-\phi_h)\dot{\beta_p}-\sin(\beta_p)(\sin(\phi_p)\cos(\gamma-\phi_h)\dot{\phi_h}+\sin(\beta_h)\cos(\phi_p)\cos(\gamma-\phi_h)\dot{\beta_h}+\sin(\phi_p)\cos(\beta_h)\cos(\gamma-\phi_h)\dot{\phi_p}-\cos(\phi_p)\sin(\gamma-\phi_h)\dot{\phi_p}-\cos(\beta_h)\cos(\phi_p)\sin(\gamma-\phi_h)(\dot{\phi_h}-\dot{\gamma})))-\sin(\gamma)(\dot{\alpha}+\dot{\theta})(\cos(\beta_h)\cos(\beta_p)\sin(\gamma-\phi_h)\dot{\beta_h}-\sin(\beta_h)\sin(\beta_p)\sin(\gamma-\phi_h)\dot{\beta_p}-\sin(\beta_h)\cos(\beta_p)\cos(\gamma-\phi_h)\dot{\phi_h}-\cos(\beta_p)(\sin(\phi_p)\cos(\gamma-\phi_h)-\cos(\beta_h)\cos(\phi_p)\sin(\gamma-\phi_h))\dot{\beta_p}-\sin(\beta_p)(\sin(\phi_p)\sin(\gamma-\phi_h)\dot{\phi_h}+\cos(\phi_p)\cos(\gamma-\phi_h)\dot{\phi_p}+\sin(\beta_h)\cos(\phi_p)\sin(\gamma-\phi_h)\dot{\beta_h}+\sin(\phi_p)\cos(\beta_h)\sin(\gamma-\phi_h)\dot{\phi_p}+\cos(\beta_h)\cos(\phi_p)\cos(\gamma-\phi_h)(\dot{\phi_h}-\dot{\gamma})))-(\dot{\beta_p}+\cos(\phi_p)\dot{\beta_h}+\sin(\beta_h)\sin(\phi_p)\dot{\phi_h}+\sin(\gamma)(\cos(\phi_p)\cos(\gamma-\phi_h)+\sin(\phi_p)\cos(\beta_h)\sin(\gamma-\phi_h))(\dot{\alpha}+\dot{\theta})-\cos(\gamma)(\cos(\phi_p)\sin(\gamma-\phi_h)-\sin(\phi_p)\cos(\beta_h)\cos(\gamma-\phi_h))(\dot{\alpha}+\dot{\theta}))(\sin(\beta_p)\dot{\phi_p}+(\sin(\beta_p)\cos(\beta_h)+\sin(\beta_h)\cos(\beta_p)\cos(\phi_p))\dot{\phi_h}-\sin(\phi_p)\cos(\beta_p)\dot{\beta_h}-\sin(\gamma)(\sin(\beta_h)\sin(\beta_p)\sin(\gamma-\phi_h)+\cos(\beta_p)(\sin(\phi_p)\cos(\gamma-\phi_h)-\cos(\beta_h)\cos(\phi_p)\sin(\gamma-\phi_h)))(\dot{\alpha}+\dot{\theta})-\cos(\gamma)(\sin(\beta_h)\sin(\beta_p)\cos(\gamma-\phi_h)-\cos(\beta_p)(\sin(\phi_p)\sin(\gamma-\phi_h)+\cos(\beta_h)\cos(\phi_p)\cos(\gamma-\phi_h)))(\dot{\alpha}+\dot{\theta}))-\cos(\gamma)(\sin(\beta_h)\cos(\beta_p)\cos(\gamma-\phi_h)+\sin(\beta_p)(\sin(\phi_p)\sin(\gamma-\phi_h)+\cos(\beta_h)\cos(\phi_p)\cos(\gamma-\phi_h)))(\ddot{\alpha}+\ddot{\theta})-\sin(\gamma)(\sin(\beta_h)\cos(\beta_p)\sin(\gamma-\phi_h)-\sin(\beta_p)(\sin(\phi_p)\cos(\gamma-\phi_h)-\cos(\beta_h)\cos(\phi_p)\sin(\gamma-\phi_h)))(\ddot{\alpha}+\ddot{\theta}))=0$$

$$-gm_{hook}\ell_h\sin(\beta_h)\cos(\phi_h)-gm_{pay}\cos(\phi_h)(\ell_h\sin(\beta_h)+\ell_p\sin(\beta_p)\cos(\beta_h)+\ell_p\sin(\beta_h)\cos(\beta_p)\cos(\phi_p))-\ell_p m_{pay}(\ell_p\cos(\phi_p)+\ell_h\cos(\beta_p))\ddot{\beta_p}-\ell_p^2 m_{pay}\sin(\beta_p)\sin(\phi_p)\cos(\beta_p)\ddot{\phi_p}-(m_{hook}\ell_h^2+m_{pay}(\ell_p^2+\ell_h^2+2\ell_h\ell_p\cos(\beta_p)\cos(\phi_p)-\ell_p^2\sin(\phi_p)^2\cos(\beta_p)^2))\ddot{\beta_h}-\ell_p m_{pay}\sin(\phi_p)(\ell_p\sin(\beta_h)\cos(\phi_p)+\ell_h\sin(\beta_h)\cos(\beta_p)+\ell_p\sin(\beta_p)(\cos(\beta_h)\cos(\beta_p)-\sin(\beta_h)\sin(\beta_p)\cos(\phi_p)))\ddot{\phi_h}-0.5m_{hook}\ell_h(4\dot{\ell_h}(\dot{\beta_h}+\sin(\phi_h)(\dot{\alpha}+\dot{\theta}))+2x_{luff}\sin(\beta_h)\sin(\phi_h)(\dot{\alpha}+\dot{\theta})^2+2\ell_h\sin(\beta_h)\dot{\phi_h}(\cos(\beta_h)\dot{\phi_h}-\sin(\beta_h)\cos(\phi_h)(\dot{\alpha}+\dot{\theta}))+2x_{luff}\cos(\beta_h)(\ddot{\alpha}+\ddot{\theta})+2\ell_h(\cos(\phi_h)\dot{\phi_h}(\dot{\alpha}+\dot{\theta})+\sin(\phi_h)(\ddot{\alpha}+\ddot{\theta}))+2\ell_{boom}\sin(\beta_h)\cos(\gamma-\phi_h)(\sin(\gamma)\cos(\gamma)(\dot{\alpha}+\dot{\theta})^2+\ddot{\gamma})+(\sin(\theta)\cos(\beta_h)+\sin(\beta_h)\sin(\phi_h)\cos(\theta))((\ell_{axle}+2x_{slew})\dot{\alpha}^2+2y_{slew}\ddot{\alpha})-2\ell_{boom}\sin(\beta_h)\sin(\gamma-\phi_h)(\dot{\gamma}^2+\cos(\gamma)^2(\dot{\alpha}+\dot{\theta})^2)-(\cos(\beta_h)\cos(\theta)-\sin(\beta_h)\sin(\phi_h)\sin(\theta))(2y_{slew}\dot{\alpha}^2-(\ell_{axle}+2x_{slew})\ddot{\alpha})-2(\cos(\alpha)(\sin(\theta)\cos(\beta_h)+\sin(\beta_h)\sin(\phi_h)\cos(\theta))+\sin(\alpha)(\cos(\beta_h)\cos(\theta)-\sin(\beta_h)\sin(\phi_h)\sin(\theta)))\ddot{x}-2(\sin(\alpha)(\sin(\theta)\cos(\beta_h)+\sin(\beta_h)\sin(\phi_h)\cos(\theta))-\cos(\alpha)(\cos(\beta_h)\cos(\theta)-\sin(\beta_h)\sin(\phi_h)\sin(\theta)))\ddot{y}-2\cos(\beta_h)(2\ell_{boom}\sin(\gamma)\dot{\gamma}(\dot{\alpha}+\dot{\theta})-\ell_h\cos(\phi_h)(\dot{\alpha}+\dot{\theta})(\cos(\beta_h)\dot{\phi_h}-\sin(\beta_h)\cos(\phi_h)(\dot{\alpha}+\dot{\theta}))-\ell_{boom}\cos(\gamma)(\ddot{\alpha}+\ddot{\theta})))-0.5m_{pay}(2x_{luff}\ell_h\sin(\beta_h)\sin(\phi_h)(\dot{\alpha}+\dot{\theta})^2+2\ell_h^2\sin(\beta_h)(\dot{\phi_h}-\dot{\gamma})(\cos(\beta_h)\dot{\phi_h}-\sin(\beta_h)\cos(\phi_h)(\dot{\alpha}+\dot{\theta}))+2\ell_h\ell_p\cos(\phi_p)(\sin(\beta_h)\cos(\beta_p)+\sin(\beta_p)\cos(\beta_h)\cos(\phi_p))(\dot{\phi_h}-\dot{\gamma})(\cos(\beta_h)\dot{\phi_h}-\sin(\beta_h)\cos(\phi_h)(\dot{\alpha}+\dot{\theta}))+2\ell_{boom}\ell_p\cos(\phi_p)(\sin(\beta_p)\sin(\phi_p)\cos(\gamma-\phi_h)-\sin(\gamma-\phi_h)(\sin(\beta_h)\cos(\beta_p)+\sin(\beta_p)\cos(\beta_h)\cos(\phi_p)))(\dot{\gamma}^2+\cos(\gamma)^2(\dot{\alpha}+\dot{\theta})^2)+2x_{luff}\ell_p\cos(\phi_p)(\sin(\gamma)(\sin(\beta_p)\sin(\phi_p)\sin(\gamma-\phi_h)+\cos(\gamma-\phi_h)(\sin(\beta_h)\cos(\beta_p)+\sin(\beta_p)\cos(\beta_h)\cos(\phi_p)))+\cos(\gamma)(\sin(\beta_p)\sin(\phi_p)\cos(\gamma-\phi_h)-\sin(\gamma-\phi_h)(\sin(\beta_h)\cos(\beta_p)+\sin(\beta_p)\cos(\beta_h)\cos(\phi_p))))(\dot{\alpha}+\dot{\theta})^2+2\ell_p^2\sin(\beta_p)\cos(\phi_p)\dot{\phi_p}(\cos(\beta_p)\dot{\phi_p}+\sin(\beta_p)\sin(\phi_p)\dot{\beta_h}+(\cos(\beta_h)\cos(\beta_p)-\sin(\beta_h)\sin(\beta_p)\cos(\phi_p))\dot{\phi_h}-\cos(\gamma)(\sin(\beta_h)\cos(\beta_p)\cos(\gamma-\phi_h)+\sin(\beta_p)(\sin(\phi_p)\sin(\gamma-\phi_h)+\cos(\beta_h)\cos(\phi_p)\cos(\gamma-\phi_h)))(\dot{\alpha}+\dot{\theta})-\sin(\gamma)(\sin(\beta_h)\cos(\beta_p)\sin(\gamma-\phi_h)-\sin(\beta_p)(\sin(\phi_p)\cos(\gamma-\phi_h)-\cos(\beta_h)\cos(\phi_p)\sin(\gamma-\phi_h)))(\dot{\alpha}+\dot{\theta}))+2x_{luff}\ell_h\cos(\beta_h)(\ddot{\alpha}+\ddot{\theta})+2\ell_{boom}\ell_h\sin(\beta_h)\cos(\gamma-\phi_h)(\sin(\gamma)\cos(\gamma)(\dot{\alpha}+\dot{\theta})^2+\ddot{\gamma})+2x_{luff}\ell_p\cos(\phi_p)(\cos(\beta_h)\cos(\beta_p)-\sin(\beta_h)\sin(\beta_p)\cos(\phi_p))(\ddot{\alpha}+\ddot{\theta})+\ell_h(\sin(\theta)\cos(\beta_h)+\sin(\beta_h)\sin(\phi_h)\cos(\theta))((\ell_{axle}+2x_{slew})\dot{\alpha}^2+2y_{slew}\ddot{\alpha})+2\ell_p\sin(\beta_p)(\ell_h(\dot{\beta_h}+\sin(\phi_h)$$

$$(\dot{\alpha} + \dot{\theta}))^2 + \ell_h \cos(\beta_h)\dot{\gamma}(\cos(\beta_h)\dot{\phi_h} - \sin(\beta_h)\cos(\phi_h)(\dot{\alpha} + \dot{\theta})) - \ddot{\ell_h}) + 2\ell_{boom}\ell_p \cos(\phi_p)(\sin(\beta_p)\sin(\phi_p)\sin(\gamma - \phi_h) + \cos(\gamma - \phi_h)(\sin(\beta_h)\cos(\beta_p) + \sin(\beta_p)\cos(\beta_h)\cos(\phi_p)))(\sin(\gamma)\cos(\gamma)(\dot{\alpha}+\dot{\theta})^2 + \ddot{\gamma}) + \ell_p \cos(\phi_p)(\sin(\theta)(\cos(\beta_h)\cos(\beta_p) - \sin(\beta_h)\sin(\beta_p)\cos(\phi_p)) + \cos(\theta)(\sin(\gamma)(\sin(\beta_p)\sin(\phi_p)\sin(\gamma - \phi_h) + \cos(\gamma - \phi_h)(\sin(\beta_h)\cos(\beta_p) + \sin(\beta_p)\cos(\beta_h)\cos(\phi_p))) + \cos(\gamma)(\sin(\beta_p)\sin(\phi_p)\cos(\gamma - \phi_h) - \sin(\gamma - \phi_h)(\sin(\beta_h)\cos(\beta_p) + \sin(\beta_p)\cos(\beta_h)\cos(\phi_p)))))((\ell_{axle} + 2x_{slew})\dot{\alpha}^2 + 2y_{slew}\ddot{\alpha}) + 2\ell_h\ell_p \cos(\beta_p)(\sin(\beta_h)\cos(\phi_p)\dot{\phi_h}\dot{\phi_p} + \sin(\phi_p)\cos(\beta_h)\dot{\beta_h}\dot{\phi_h} + \sin(\gamma)(\dot{\alpha} + \dot{\theta})(\cos(\phi_p)\sin(\gamma - \phi_h)\dot{\phi_h} + \cos(\beta_h)\cos(\phi_p)\sin(\gamma - \phi_h)\dot{\phi_p} - \sin(\phi_p)\cos(\gamma - \phi_h)\dot{\phi_p} - \sin(\beta_h)\sin(\phi_p)\sin(\gamma - \phi_h)\dot{\beta_h} - \sin(\phi_p)\cos(\beta_h)\cos(\gamma - \phi_h)(\dot{\phi_h} - \dot{\gamma})) + ((\sin(\beta_p)\cos(\beta_h) + \sin(\beta_h)\cos(\beta_p)\cos(\phi_p))\dot{\phi_h} - \sin(\gamma)(\sin(\beta_h)\sin(\beta_p)\sin(\gamma - \phi_h) + \cos(\beta_p)(\sin(\phi_p)\cos(\gamma - \phi_h) - \cos(\beta_h)\cos(\phi_p)\sin(\gamma - \phi_h)))(\dot{\alpha} + \dot{\theta}) - \cos(\gamma)(\sin(\beta_h)\sin(\beta_p)\cos(\gamma - \phi_h) - \cos(\beta_p)(\sin(\phi_p)\sin(\gamma - \phi_h) + \cos(\beta_h)\cos(\phi_p)\cos(\gamma - \phi_h)))(\dot{\alpha} + \dot{\theta}))(\cos(\beta_p)\dot{\phi_p} + \sin(\beta_p)\sin(\phi_p)\dot{\beta_h} + (\cos(\beta_h)\cos(\beta_p) - \sin(\beta_h)\sin(\beta_p)\cos(\phi_p))\dot{\phi_h} - \cos(\gamma)(\sin(\beta_h)\cos(\beta_p)\cos(\gamma - \phi_h) + \sin(\beta_p)(\sin(\phi_p)\sin(\gamma - \phi_h) + \cos(\beta_h)\cos(\phi_p)\cos(\gamma - \phi_h)))(\dot{\alpha} + \dot{\theta}) - \sin(\gamma)(\sin(\beta_h)\cos(\beta_p)\sin(\gamma - \phi_h) - \sin(\beta_p)(\sin(\phi_p)\cos(\gamma - \phi_h) - \cos(\beta_h)\cos(\phi_p)\sin(\gamma - \phi_h)))(\dot{\alpha} + \dot{\theta})) + \sin(\gamma)(\cos(\phi_p)\cos(\gamma - \phi_h) + \sin(\phi_p)\cos(\beta_h)\sin(\gamma - \phi_h))(\ddot{\alpha} + \ddot{\theta}) - \sin(\phi_p)\dot{\beta_h}\dot{\phi_p} - \sin(\phi_h)\sin(\phi_p)\cos(\beta_h)\dot{\gamma}(\dot{\alpha} + \dot{\theta}) - \cos(\gamma)(\dot{\alpha} + \dot{\theta})(\sin(\beta_h)\sin(\phi_p)\cos(\gamma - \phi_h)\dot{\beta_h} - \sin(\phi_p)\sin(\gamma - \phi_h)\dot{\phi_p} - \cos(\phi_p)\cos(\gamma - \phi_h)\dot{\phi_h} - \cos(\beta_h)\cos(\phi_p)\cos(\gamma - \phi_h)\dot{\phi_p} - \sin(\phi_p)\cos(\beta_h)\sin(\gamma - \phi_h)(\dot{\phi_h} - \dot{\gamma})) - \cos(\gamma)(\cos(\phi_p)\sin(\gamma - \phi_h) - \sin(\phi_p)\cos(\beta_h)\cos(\gamma - \phi_h))(\ddot{\alpha} + \ddot{\theta})) + 2\ell_p^2 \cos(\phi_p)(\sin(\beta_h)\cos(\phi_p)\dot{\phi_h}\dot{\phi_p} + \sin(\phi_p)\cos(\beta_h)\dot{\beta_h}\dot{\phi_h} + \sin(\gamma)(\dot{\alpha} + \dot{\theta})(\cos(\phi_p)\sin(\gamma - \phi_h)\dot{\phi_h} + \cos(\beta_h)\cos(\phi_p)\sin(\gamma - \phi_h)\dot{\phi_p} - \sin(\phi_p)\cos(\gamma - \phi_h)\dot{\phi_p} - \sin(\beta_h)\sin(\phi_p)\sin(\gamma - \phi_h)\dot{\beta_h} - \sin(\phi_p)\cos(\beta_h)\cos(\gamma - \phi_h)(\dot{\phi_h} - \dot{\gamma})) + ((\sin(\beta_p)\cos(\beta_h) + \sin(\beta_h)\cos(\beta_p)\cos(\phi_p))\dot{\phi_h} - \sin(\gamma)(\sin(\beta_h)\sin(\beta_p)\sin(\gamma - \phi_h) + \cos(\beta_p)(\sin(\phi_p)\cos(\gamma - \phi_h) - \cos(\beta_h)\cos(\phi_p)\sin(\gamma - \phi_h)))(\dot{\alpha} + \dot{\theta}) - \cos(\gamma)(\sin(\beta_h)\sin(\beta_p)\cos(\gamma - \phi_h) - \cos(\beta_p)(\sin(\phi_p)\sin(\gamma - \phi_h) + \cos(\beta_h)\cos(\phi_p)\cos(\gamma - \phi_h)))(\dot{\alpha} + \dot{\theta}))(\cos(\beta_p)\dot{\phi_p} + \sin(\beta_p)\sin(\phi_p)\dot{\beta_h} + (\cos(\beta_h)\cos(\beta_p) - \sin(\beta_h)\sin(\beta_p)\cos(\phi_p))\dot{\phi_h} - \cos(\gamma)(\sin(\beta_h)\cos(\beta_p)\cos(\gamma - \phi_h) + \sin(\beta_p)(\sin(\phi_p)\sin(\gamma - \phi_h) + \cos(\beta_h)\cos(\phi_p)\cos(\gamma - \phi_h)))(\dot{\alpha} + \dot{\theta}) - \sin(\gamma)(\sin(\beta_h)\cos(\beta_p)\sin(\gamma - \phi_h) - \sin(\beta_p)(\sin(\phi_p)\cos(\gamma - \phi_h) - \cos(\beta_h)\cos(\phi_p)\sin(\gamma - \phi_h)))(\dot{\alpha} + \dot{\theta})) + \sin(\gamma)(\cos(\phi_p)\cos(\gamma - \phi_h) + \sin(\phi_p)\cos(\beta_h)\sin(\gamma - \phi_h))(\ddot{\alpha} + \ddot{\theta}) - \sin(\phi_p)\dot{\beta_h}\dot{\phi_p} - \sin(\phi_h)\sin(\phi_p)\cos(\beta_h)\dot{\gamma}(\dot{\alpha} + \dot{\theta}) - \cos(\gamma)(\dot{\alpha} + \dot{\theta})(\sin(\beta_h)\sin(\phi_p)\cos(\gamma - \phi_h)\dot{\beta_h} - \sin(\phi_p)\sin(\gamma - \phi_h)\dot{\phi_p} - \cos(\phi_p)\cos(\gamma - \phi_h)\dot{\phi_h} - \cos(\beta_h)\cos(\phi_p)\cos(\gamma - \phi_h)\dot{\phi_p} - \sin(\phi_p)\cos(\beta_h)\sin(\gamma - \phi_h)(\dot{\phi_h} - \dot{\gamma})) - \cos(\gamma)(\cos(\phi_p)\sin(\gamma - \phi_h) - \sin(\phi_p)\cos(\beta_h)\cos(\gamma - \phi_h))(\ddot{\alpha} + \ddot{\theta})) - 2\ell_{boom}\ell_h \sin(\beta_h)\sin(\gamma - \phi_h)(\dot{\gamma}^2 + \cos(\gamma)^2(\dot{\alpha} + \dot{\theta})^2) - 2\ell_h\ell_p \sin(\beta_p)((\beta_p + \cos(\phi_p)\dot{\beta_h} + \sin(\beta_h)\sin(\phi_p)\dot{\phi_h} + \sin(\gamma)(\cos(\phi_p)\cos(\gamma - \phi_h) + \sin(\phi_p)\cos(\beta_h)\sin(\gamma - \phi_h))(\dot{\alpha} + \dot{\theta}) - \cos(\gamma)(\cos(\phi_p)\sin(\gamma - \phi_h) - \sin(\phi_p)\cos(\beta_h)\cos(\gamma - \phi_h))(\dot{\alpha} + \dot{\theta}))^2 + ((\cos(\beta_h)\cos(\beta_p) - \sin(\beta_h)\sin(\beta_p)\cos(\phi_p))\dot{\phi_h} - \cos(\gamma)(\sin(\beta_h)\cos(\beta_p)\cos(\gamma - \phi_h) + \sin(\beta_p)(\sin(\phi_p)\sin(\gamma - \phi_h) + \cos(\beta_h)\cos(\phi_p)\cos(\gamma - \phi_h)))(\dot{\alpha} + \dot{\theta}) - \sin(\gamma)(\sin(\beta_h)\sin(\beta_p)\cos(\gamma - \phi_h) - \cos(\beta_p)(\sin(\phi_p)\sin(\gamma - \phi_h) - \cos(\beta_h)\cos(\phi_p)\cos(\gamma - \phi_h)))(\dot{\alpha} + \dot{\theta}))(\cos(\beta_p)\dot{\phi_p} + \sin(\beta_p)\sin(\phi_p)\dot{\beta_h} + (\cos(\beta_h)\cos(\beta_p) - \sin(\beta_h)\sin(\beta_p)\cos(\phi_p))\dot{\phi_h} - \cos(\gamma)(\sin(\beta_h)\cos(\beta_p)\cos(\gamma - \phi_h) + \sin(\beta_p)(\sin(\phi_p)\sin(\gamma - \phi_h) + \cos(\beta_h)\cos(\phi_p)\cos(\gamma - \phi_h)))(\dot{\alpha} + \dot{\theta}) - \sin(\gamma)(\sin(\beta_h)\cos(\beta_p)\sin(\gamma - \phi_h) - \sin(\beta_p)(\sin(\phi_p)\cos(\gamma - \phi_h) - \cos(\beta_h)\cos(\phi_p)\sin(\gamma - \phi_h)))(\dot{\alpha} + \dot{\theta}))) - \ell_h(\cos(\beta_h)\cos(\theta) - \sin(\beta_h)\sin(\phi_h)\sin(\theta))(2y_{slew}\dot{\alpha}^2 - (\ell_{axle} + 2x_{slew})\ddot{\alpha}) - 2\ell_h(\cos(\alpha)(\sin(\theta)\cos(\beta_h) + \sin(\beta_h)\sin(\phi_h)\cos(\theta)) + \sin(\alpha)(\cos(\beta_h)\cos(\theta) - \sin(\beta_h)\sin(\phi_h)\sin(\theta)))\ddot{x} - 2\ell_h(\sin(\alpha)(\sin(\theta)\cos(\beta_h) + \sin(\beta_h)\sin(\phi_h)\cos(\theta)) - \cos(\alpha)(\cos(\beta_h)\cos(\theta) - \sin(\beta_h)\sin(\phi_h)\sin(\theta)))\ddot{y} - 2\ell_h\cos(\beta_h)(2\ell_{boom}\sin(\gamma)\dot{\gamma}(\dot{\alpha} + \dot{\theta}) - \ell_h\cos(\phi_h)(\dot{\alpha} + \dot{\theta})(\cos(\beta_h)\dot{\phi_h} - \sin(\beta_h)\cos(\phi_h)(\dot{\alpha}+\dot{\theta})) - \ell_{boom}\cos(\gamma)(\ddot{\alpha}+\ddot{\theta})) - 2\ell_p\cos(\phi_p)(\cos(\beta_h)\cos(\beta_p) - \sin(\beta_h)\sin(\beta_p)\cos(\phi_p))(2\ell_{boom}\sin(\gamma)\dot{\gamma}(\dot{\alpha} + \dot{\theta}) - \ell_h\cos(\phi_h)(\dot{\alpha} + \dot{\theta})(\cos(\beta_h)\dot{\phi_h} - \sin(\beta_h)\cos(\phi_h)(\dot{\alpha} + \dot{\theta})) - \ell_{boom}\cos(\gamma)(\ddot{\alpha} + \ddot{\theta})) - \ell_p\cos(\phi_p)(\cos(\theta)(\cos(\beta_h)\cos(\beta_p) - \sin(\beta_h)\sin(\beta_p)\cos(\phi_p)) - \sin(\theta)(\sin(\gamma)(\sin(\beta_p)\sin(\phi_p)\sin(\gamma - \phi_h) + \cos(\gamma - \phi_h)(\sin(\beta_h)\cos(\beta_p) + \sin(\beta_p)\cos(\beta_h)\cos(\phi_p))) + \cos(\gamma)(\sin(\beta_p)\sin(\phi_p)\cos(\gamma - \phi_h) - \sin(\gamma - \phi_h)(\sin(\beta_h)\cos(\beta_p) + \sin(\beta_p)\cos(\beta_h)\cos(\phi_p)))))(2y_{slew}\dot{\alpha}^2 - (\ell_{axle} + 2x_{slew})\ddot{\alpha}) - 2\ell_h(\ell_p\sin(\phi_p)\dot{\beta_h}(\cos(\beta_p)\dot{\phi_p} + \sin(\beta_p)\sin(\phi_p)\dot{\beta_h} + (\cos(\beta_h)\cos(\beta_p) - \sin(\beta_h)\sin(\beta_p)\cos(\phi_p))\dot{\phi_h} - \cos(\gamma)(\sin(\beta_h)\cos(\beta_p)\cos(\gamma - \phi_h) + \sin(\beta_p)(\sin(\phi_p)\sin(\gamma - \phi_h) + \cos(\beta_h)\cos(\phi_p)\cos(\gamma - \phi_h)))(\dot{\alpha} + \dot{\theta}) - \sin(\gamma)(\sin(\beta_h)\cos(\beta_p)\sin(\gamma - \phi_h) - \sin(\beta_p)(\sin(\phi_p)\cos(\gamma - \phi_h) - \cos(\beta_h)\cos(\phi_p)\sin(\gamma - \phi_h)))(\dot{\alpha} + \dot{\theta})) - 2\dot{\ell_h}(\dot{\beta_h} + \sin(\phi_h)(\dot{\alpha} + \dot{\theta})) - \ell_h\sin(\beta_h)\dot{\gamma}(\cos(\beta_h)\dot{\phi_h} - \sin(\beta_h)\cos(\phi_h)(\dot{\alpha} + \dot{\theta})) - \ell_h(\cos(\phi_h)\dot{\phi_h}(\dot{\alpha} + \dot{\theta}) + \sin(\phi_h)(\ddot{\alpha} + \ddot{\theta}))) - 2\ell_p\cos(\beta_p)\cos(\phi_p)(\ell_p\sin(\phi_p)\dot{\beta_h}(\cos(\beta_p)\dot{\phi_p} + \sin(\beta_p)\sin(\phi_p)\dot{\beta_h} + (\cos(\beta_h)\cos(\beta_p) - \sin(\beta_h)\sin(\beta_p)\cos(\phi_p))\dot{\phi_h} - \cos(\gamma)(\sin(\beta_h)\cos(\beta_p)\cos(\gamma - \phi_h) + \sin(\beta_p)(\sin(\phi_p)\sin(\gamma - \phi_h) + \cos(\beta_h)\cos(\phi_p)\cos(\gamma - \phi_h)))(\dot{\alpha} + \dot{\theta}) - \sin(\gamma)(\sin(\beta_h)\cos(\beta_p)\sin(\gamma - \phi_h) - \sin(\beta_p)(\sin(\phi_p)\cos(\gamma - \phi_h) - \cos(\beta_h)\cos(\phi_p)\sin(\gamma - \phi_h)))(\dot{\alpha} + \dot{\theta})) - 2\dot{\ell_h}(\dot{\beta_h} + \sin(\phi_h)(\dot{\alpha} + \dot{\theta})) - \ell_h\sin(\beta_h)\dot{\gamma}(\cos(\beta_h)\dot{\phi_h} - \sin(\beta_h)\cos(\phi_h)(\dot{\alpha} + \dot{\theta})) - \ell_h(\cos(\phi_h)\dot{\phi_h}(\dot{\alpha} + \dot{\theta}) + \sin(\phi_h)(\ddot{\alpha} + \ddot{\theta}))) - 2\ell_p\cos(\phi_p)(\cos(\alpha)(\sin(\theta)(\cos(\beta_h)\cos(\beta_p) - \sin(\beta_h)\sin(\beta_p)\cos(\phi_p)) + \cos(\theta)(\sin(\gamma)(\sin(\beta_p)\sin(\phi_p)\sin(\gamma - \phi_h) + \cos(\gamma - \phi_h)(\sin(\beta_h)\cos(\beta_p) + \sin(\beta_p)\cos(\beta_h)\cos(\phi_p))) + \cos(\gamma)(\sin(\beta_p)\sin(\phi_p)\cos(\gamma - \phi_h) - \sin(\gamma - \phi_h)(\sin(\beta_h)\cos(\beta_p) + \sin(\beta_p)\cos(\beta_h)\cos(\phi_p)))) + \sin(\alpha)(\cos(\theta)(\cos(\beta_h)\cos(\beta_p) - \sin(\beta_h)\sin(\beta_p)\cos(\phi_p)) - \sin(\theta)(\sin(\gamma)(\sin(\beta_p)\sin(\phi_p)\sin(\gamma - \phi_h) + \cos(\gamma - \phi_h)(\sin(\beta_h)\cos(\beta_p) + \sin(\beta_p)\cos(\beta_h)\cos(\phi_p))) + \cos(\gamma)(\sin(\beta_p)\sin(\phi_p)\cos(\gamma - \phi_h) - \sin(\gamma - \phi_h)(\sin(\beta_h)\cos(\beta_p) + \sin(\beta_p)\cos(\beta_h)\cos(\phi_p)))))\ddot{x} - 2\ell_p\cos(\phi_p)(\sin(\alpha)(\sin(\theta)(\cos(\beta_h)\cos(\beta_p) - \sin(\beta_h)\sin(\beta_p)\cos(\phi_p)) + \cos(\theta)(\sin(\gamma)(\sin(\beta_p)\sin(\phi_p)\sin(\gamma - \phi_h) + \cos(\gamma - \phi_h)(\sin(\beta_h)\cos(\beta_p) + \sin(\beta_p)\cos(\beta_h)\cos(\phi_p))) + \cos(\gamma)(\sin(\beta_p)\sin(\phi_p)\cos(\gamma - \phi_h) - \sin(\gamma - \phi_h)(\sin(\beta_h)\cos(\beta_p) + \sin(\beta_p)\cos(\beta_h)\cos(\phi_p)))) - \cos(\alpha)(\cos(\theta)(\cos(\beta_h)\cos(\beta_p) - \sin(\beta_h)\sin(\beta_p)\cos(\phi_p)) - \sin(\theta)(\sin(\gamma)(\sin(\beta_p)\sin(\phi_p)\sin(\gamma - \phi_h) + \cos(\gamma - \phi_h)(\sin(\beta_h)\cos(\beta_p) + \sin(\beta_p)\cos(\beta_h)\cos(\phi_p))) + \cos(\gamma)(\sin(\beta_p)\sin(\phi_p)\cos(\gamma - \phi_h) - \sin(\gamma - \phi_h)(\sin(\beta_h)\cos(\beta_p) + \sin(\beta_p)\cos(\beta_h)\cos(\phi_p))))\ddot{y} - \ell_p\sin(\beta_p)\sin(\phi_p)(2\ell_{boom}(\cos(\phi_p)\cos(\gamma - \phi_h) + \sin(\phi_p)\cos(\beta_h)\sin(\gamma - \phi_h))(\dot{\gamma}^2 + \cos(\gamma)^2(\dot{\alpha} + \dot{\theta})^2) + 2x_{luff}(\cos(\gamma)(\cos(\phi_p)\cos(\gamma - \phi_h) + \sin(\phi_p)\cos(\beta_h)\sin(\gamma - \phi_h)) + \sin(\gamma)(\cos(\phi_p)\sin(\gamma - \phi_h) - \sin(\phi_p)\cos(\beta_h)\cos(\gamma - \phi_h)))(\dot{\alpha} + \dot{\theta})^2 + 2x_{luff}\sin(\beta_h)\sin(\phi_p)(\ddot{\alpha} + \ddot{\theta}) + 2\ell_{boom}(\cos(\phi_p)\sin(\gamma - \phi_h) - \sin(\phi_p)\cos(\beta_h)\cos(\gamma - \phi_h))(\sin(\gamma)\cos(\gamma)(\dot{\alpha} + \dot{\theta})^2 + \ddot{\gamma}) + (\sin(\beta_h)\sin(\phi_p)\sin(\theta) + \cos(\theta)(\cos(\gamma)(\cos(\phi_p)\cos(\gamma - \phi_h) + \sin(\phi_p)\cos(\beta_h)\sin(\gamma - \phi_h)) + \sin(\gamma)(\cos(\phi_p)\sin(\gamma - \phi_h) - \sin(\phi_p)\cos(\beta_h)\cos(\gamma - \phi_h))))((\ell_{axle} + 2x_{slew})\dot{\alpha}^2 + 2y_{slew}\ddot{\alpha}) - 2\ell_h\sin(\phi_p)\cos(\beta_h)(\dot{\phi_h} - \dot{\gamma})(\cos(\beta_h)\dot{\phi_h} - \sin(\beta_h)\cos(\phi_h)(\dot{\alpha} + \dot{\theta})) - 2\sin(\beta_h)\sin(\phi_p)(2\ell_{boom}\sin(\gamma)\dot{\gamma}(\dot{\alpha} + \dot{\theta}) - \ell_h\cos(\phi_h)(\dot{\alpha} + \dot{\theta})(\cos(\beta_h)\dot{\phi_h} - \sin(\beta_h)\cos(\phi_h)(\dot{\alpha} + \dot{\theta})) - \ell_{boom}\cos(\gamma)(\ddot{\alpha} + \ddot{\theta})) - (\sin(\beta_h)\sin(\phi_p)\cos(\theta) - \sin(\theta)(\cos(\gamma)(\cos(\phi_p)\cos(\gamma - \phi_h) + \sin(\phi_p)\cos(\beta_h)\sin(\gamma - \phi_h)) + \sin(\gamma)(\cos(\phi_p)\sin(\gamma - \phi_h) - \sin(\phi_p)\cos(\beta_h)\cos(\gamma - \phi_h))))(2y_{slew}\dot{\alpha}^2 - (\ell_{axle} + 2x_{slew})\ddot{\alpha}) - 2(\cos(\alpha)(\sin(\beta_h)\sin(\phi_p)\sin(\theta) + \cos(\theta)(\cos(\gamma)(\cos(\phi_p)\cos(\gamma - \phi_h) +$$

$$\sin(\phi_p)\cos(\beta_h)\sin(\gamma - \phi_h)) + \sin(\gamma)(\cos(\phi_p)\sin(\gamma - \phi_h) - \sin(\phi_p)\cos(\beta_h)\cos(\gamma - \phi_h)))) + \sin(\alpha)(\sin(\beta_h)\sin(\phi_p)\cos(\theta) - \sin(\theta)(\cos(\gamma)(\cos(\phi_p)\cos(\gamma - \phi_h) + \sin(\phi_p)\cos(\beta_h)\sin(\gamma - \phi_h)) + \sin(\gamma)(\cos(\phi_p)\sin(\gamma - \phi_h) - \sin(\phi_p)\cos(\beta_h)\cos(\gamma - \phi_h)))))\ddot{x} - 2(\sin(\alpha)(\sin(\beta_h)\sin(\phi_p)\sin(\theta) + \cos(\theta)(\cos(\gamma)(\cos(\phi_p)\cos(\gamma - \phi_h) + \sin(\phi_p)\cos(\beta_h)\sin(\gamma - \phi_h)) + \sin(\gamma)(\cos(\phi_p)\sin(\gamma - \phi_h) - \sin(\phi_p)\cos(\beta_h)\cos(\gamma - \phi_h)))) - \cos(\alpha)(\sin(\beta_h)\sin(\phi_p)\cos(\theta) - \sin(\theta)(\cos(\gamma)(\cos(\phi_p)\cos(\gamma - \phi_h) + \sin(\phi_p)\cos(\beta_h)\sin(\gamma - \phi_h)) + \sin(\gamma)(\cos(\phi_p)\sin(\gamma - \phi_h) - \sin(\phi_p)\cos(\beta_h)\cos(\gamma - \phi_h)))))\ddot{y} - 2\ell_p(\sin(\beta_p)\cos(\phi_p)\dot{\beta_h}\dot{\phi_p} + \sin(\phi_p)\cos(\beta_p)\dot{\beta_h}\dot{\beta_p} + \dot{\phi_h}(\sin(\beta_h)\sin(\beta_p)\sin(\phi_p)\dot{\phi_p} - \sin(\beta_h)\cos(\beta_p)\dot{\beta_h} - \sin(\beta_p)\cos(\beta_h)\dot{\beta_p} - \sin(\beta_h)\cos(\beta_p)\cos(\phi_p)\dot{\beta_p} - \sin(\beta_p)\cos(\beta_h)\cos(\phi_p)\dot{\beta_h}) + \sin(\beta_p)\sin(\phi_h)\cos(\beta_h)\cos(\phi_p)\dot{\gamma}(\dot{\alpha} + \dot{\theta}) - \sin(\beta_p)\dot{\beta_p}\dot{\phi_p} - \cos(\gamma)(\dot{\alpha} + \dot{\theta})(\sin(\beta_h)\cos(\beta_p)\sin(\gamma - \phi_h)\dot{\phi_h} + \cos(\beta_h)\cos(\beta_p)\cos(\gamma - \phi_h)\dot{\beta_h} + \cos(\beta_p)(\sin(\phi_p)\sin(\gamma - \phi_h) + \cos(\beta_h)\cos(\phi_p)\cos(\gamma - \phi_h))\dot{\beta_p} - \sin(\beta_h)\sin(\beta_p)\cos(\gamma - \phi_h)\dot{\beta_p} - \sin(\beta_p)(\sin(\phi_p)\cos(\gamma - \phi_h)\dot{\phi_h} + \sin(\beta_h)\cos(\phi_p)\cos(\gamma - \phi_h)\dot{\beta_h} + \sin(\phi_p)\cos(\beta_h)\cos(\gamma - \phi_h)\dot{\phi_p} - \cos(\phi_p)\sin(\gamma - \phi_h)\dot{\phi_p} - \cos(\beta_h)\cos(\phi_p)\sin(\gamma - \phi_h)(\dot{\phi_h} - \dot{\gamma}))) - \sin(\gamma)(\dot{\alpha} + \dot{\theta})(\cos(\beta_h)\cos(\beta_p)\sin(\gamma - \phi_h)\dot{\beta_h} - \sin(\beta_h)\sin(\beta_p)\sin(\gamma - \phi_h)\dot{\beta_p} - \sin(\beta_h)\cos(\beta_p)\cos(\gamma - \phi_h)\dot{\phi_h} - \cos(\beta_p)(\sin(\phi_p)\cos(\gamma - \phi_h) - \cos(\beta_h)\cos(\phi_p)\sin(\gamma - \phi_h))\dot{\beta_p} - \sin(\beta_p)(\sin(\phi_p)\sin(\gamma - \phi_h)\dot{\phi_h} + \cos(\phi_p)\cos(\gamma - \phi_h)\dot{\phi_p} + \sin(\beta_h)\cos(\phi_p)\sin(\gamma - \phi_h)\dot{\beta_h} + \sin(\phi_p)\cos(\beta_h)\sin(\gamma - \phi_h)\dot{\phi_p} + \cos(\beta_h)\cos(\phi_p)\cos(\gamma - \phi_h)(\dot{\phi_h} - \dot{\gamma}))) - (\dot{\beta_p} + \cos(\phi_p)\dot{\beta_h} + \sin(\beta_h)\sin(\phi_p)\dot{\phi_h} + \sin(\gamma)(\cos(\phi_p)\cos(\gamma - \phi_h) + \sin(\phi_p)\cos(\beta_h)\sin(\gamma - \phi_h))(\dot{\alpha} + \dot{\theta}))(\sin(\beta_p)\dot{\phi_p} + (\sin(\beta_p)\cos(\beta_h) + \sin(\beta_h)\cos(\beta_p)\cos(\phi_p))\dot{\phi_h} - \sin(\phi_p)\cos(\beta_p)\dot{\beta_h} - \sin(\gamma)(\sin(\beta_h)\sin(\beta_p)\sin(\gamma - \phi_h) + \cos(\beta_p)(\sin(\phi_p)\cos(\gamma - \phi_h) - \cos(\beta_h)\cos(\phi_p)\sin(\gamma - \phi_h)))(\dot{\alpha} + \dot{\theta}) - \cos(\gamma)(\sin(\beta_h)\cos(\beta_p)\sin(\gamma - \phi_h) - \cos(\beta_p)(\sin(\phi_p)\sin(\gamma - \phi_h) + \cos(\beta_h)\cos(\phi_p)\cos(\gamma - \phi_h)))(\dot{\alpha} + \dot{\theta})) - \cos(\gamma)(\sin(\beta_h)\cos(\beta_p)\cos(\gamma - \phi_h) + \sin(\beta_p)(\sin(\phi_p)\sin(\gamma - \phi_h) + \cos(\beta_h)\cos(\phi_p)\cos(\gamma - \phi_h)))(\ddot{\alpha} + \ddot{\theta}) - \sin(\gamma)(\sin(\beta_h)\cos(\beta_p)\sin(\gamma - \phi_h) - \sin(\beta_p)(\sin(\phi_p)\cos(\gamma - \phi_h) - \cos(\beta_h)\cos(\phi_p)\sin(\gamma - \phi_h)))(\ddot{\alpha} + \ddot{\theta})))) = 0$$

$$0.5\ell_p m_{pay}(2(\cos(\beta_h)\cos(\beta_p) - \sin(\beta_h)\sin(\beta_p)\cos(\phi_p))(2\ell_{boom}\sin(\gamma)\dot{\gamma}(\dot{\alpha} + \dot{\theta}) - \ell_h\cos(\phi_h)(\dot{\alpha} + \dot{\theta})(\cos(\beta_h)\dot{\phi_h} - \sin(\beta_h)\cos(\phi_h)(\dot{\alpha} + \dot{\theta})) - \ell_{boom}\cos(\gamma)(\ddot{\alpha} + \ddot{\theta})) + (\cos(\theta)(\cos(\beta_h)\cos(\beta_p) - \sin(\beta_h)\sin(\beta_p)\cos(\phi_p)) - \sin(\theta)(\sin(\gamma)(\sin(\beta_p)\sin(\phi_p)\sin(\gamma - \phi_h) + \cos(\gamma - \phi_h)(\sin(\beta_h)\cos(\beta_p) + \sin(\beta_p)\cos(\beta_h)\cos(\phi_p))) + \cos(\gamma)(\sin(\beta_p)\sin(\phi_p)\cos(\gamma - \phi_h) - \sin(\gamma - \phi_h)(\sin(\beta_h)\cos(\beta_p) + \sin(\beta_p)\cos(\beta_h)\cos(\phi_p)))))(2y_{slew}\dot{\alpha}^2 - (\ell_{axle} + 2x_{slew})\ddot{\alpha}) + 2\cos(\beta_p)(\ell_p\sin(\phi_p)\dot{\beta_h}(\cos(\beta_p)\dot{\phi_p} + \sin(\beta_p)\sin(\phi_p)\dot{\beta_h} + (\cos(\beta_h)\cos(\beta_p) - \sin(\beta_h)\sin(\beta_p)\cos(\phi_p))\dot{\phi_h} - \cos(\gamma)(\sin(\beta_h)\cos(\beta_p)\cos(\gamma - \phi_h) + \sin(\beta_p)(\sin(\phi_p)\sin(\gamma - \phi_h) + \cos(\beta_h)\cos(\phi_p)\cos(\gamma - \phi_h)))(\dot{\alpha} + \dot{\theta}) - \sin(\gamma)(\sin(\beta_h)\cos(\beta_p)\sin(\gamma - \phi_h) - \sin(\beta_p)(\sin(\phi_p)\cos(\gamma - \phi_h) - \cos(\beta_h)\cos(\phi_p)\sin(\gamma - \phi_h)))(\dot{\alpha} + \dot{\theta})) - 2\dot{\ell_h}(\dot{\beta_h} + \sin(\phi_h)(\dot{\alpha} + \dot{\theta})) - \ell_h\sin(\beta_h)\dot{\gamma}(\cos(\beta_h)\dot{\phi_h} - \sin(\beta_h)\cos(\phi_h)(\dot{\alpha} + \dot{\theta})) - \ell_h(\cos(\phi_h)\dot{\phi_h}(\dot{\alpha} + \dot{\theta}) + \sin(\phi_h)(\ddot{\alpha} + \ddot{\theta}))) + 2(\cos(\alpha)(\sin(\theta)(\cos(\beta_h)\cos(\beta_p) - \sin(\beta_h)\sin(\beta_p)\cos(\phi_p)) + \cos(\theta)(\sin(\gamma)(\sin(\beta_p)\sin(\phi_p)\sin(\gamma - \phi_h) + \cos(\gamma - \phi_h)(\sin(\beta_h)\cos(\beta_p) + \sin(\beta_p)\cos(\beta_h)\cos(\phi_p))) + \cos(\gamma)(\sin(\beta_p)\sin(\phi_p)\cos(\gamma - \phi_h) - \sin(\gamma - \phi_h)(\sin(\beta_h)\cos(\beta_p) + \sin(\beta_p)\cos(\beta_h)\cos(\phi_p)))) + \sin(\alpha)(\cos(\theta)(\cos(\beta_h)\cos(\beta_p) - \sin(\beta_h)\sin(\beta_p)\cos(\phi_p)) - \sin(\theta)(\sin(\gamma)(\sin(\beta_p)\sin(\phi_p)\sin(\gamma - \phi_h) + \cos(\gamma - \phi_h)(\sin(\beta_h)\cos(\beta_p) + \sin(\beta_p)\cos(\beta_h)\cos(\phi_p))) + \cos(\gamma)(\sin(\beta_p)\sin(\phi_p)\cos(\gamma - \phi_h) - \sin(\gamma - \phi_h)(\sin(\beta_h)\cos(\beta_p) + \sin(\beta_p)\cos(\beta_h)\cos(\phi_p))))))\ddot{x} + 2(\sin(\alpha)(\sin(\theta)(\cos(\beta_h)\cos(\beta_p) - \sin(\beta_h)\sin(\beta_p)\cos(\phi_p)) + \cos(\theta)(\sin(\gamma)(\sin(\beta_p)\sin(\phi_p)\sin(\gamma - \phi_h) + \cos(\gamma - \phi_h)(\sin(\beta_h)\cos(\beta_p) + \sin(\beta_p)\cos(\beta_h)\cos(\phi_p))) + \cos(\gamma)(\sin(\beta_p)\sin(\phi_p)\cos(\gamma - \phi_h) - \sin(\gamma - \phi_h)(\sin(\beta_h)\cos(\beta_p) + \sin(\beta_p)\cos(\beta_h)\cos(\phi_p)))) - \cos(\alpha)(\cos(\theta)(\cos(\beta_h)\cos(\beta_p) - \sin(\beta_h)\sin(\beta_p)\cos(\phi_p)) - \sin(\theta)(\sin(\gamma)(\sin(\beta_p)\sin(\phi_p)\sin(\gamma - \phi_h) + \cos(\gamma - \phi_h)(\sin(\beta_h)\cos(\beta_p) + \sin(\beta_p)\cos(\beta_h)\cos(\phi_p))) + \cos(\gamma)(\sin(\beta_p)\sin(\phi_p)\cos(\gamma - \phi_h) - \sin(\gamma - \phi_h)(\sin(\beta_h)\cos(\beta_p) + \sin(\beta_p)\cos(\beta_h)\cos(\phi_p)))))\ddot{y} - 2g(\cos(\gamma)(\sin(\beta_p)\sin(\phi_p)\sin(\gamma - \phi_h) + \cos(\gamma - \phi_h)(\sin(\beta_h)\cos(\beta_p) + \sin(\beta_p)\cos(\beta_h)\cos(\phi_p))) - \sin(\gamma)(\sin(\beta_p)\sin(\phi_p)\cos(\gamma - \phi_h) - \sin(\gamma - \phi_h)(\sin(\beta_h)\cos(\beta_p) + \sin(\beta_p)\cos(\beta_h)\cos(\phi_p)))) - 2\ell_h(\sin(\beta_h)\cos(\beta_p) + \sin(\beta_p)\cos(\beta_h)\cos(\phi_p))(\dot{\phi_h} - \dot{\gamma})(\cos(\beta_h)\dot{\phi_h} - \sin(\beta_h)\cos(\phi_h)(\dot{\alpha} + \dot{\theta})) - 2\ell_{boom}(\sin(\beta_p)\sin(\phi_p)\cos(\gamma - \phi_h) - \sin(\gamma - \phi_h)(\sin(\beta_h)\cos(\beta_p) + \sin(\beta_p)\cos(\beta_h)\cos(\phi_p)))(\dot{\gamma}^2 + \cos(\gamma)^2(\dot{\alpha} + \dot{\theta})^2) - 2x_{luff}(\sin(\gamma)(\sin(\beta_p)\sin(\phi_p)\sin(\gamma - \phi_h) + \cos(\gamma - \phi_h)(\sin(\beta_h)\cos(\beta_p) + \sin(\beta_p)\cos(\beta_h)\cos(\phi_p))) + \cos(\gamma)(\sin(\beta_p)\sin(\phi_p)\cos(\gamma - \phi_h) - \sin(\gamma - \phi_h)(\sin(\beta_h)\cos(\beta_p) + \sin(\beta_p)\cos(\beta_h)\cos(\phi_p))))(\dot{\alpha} + \dot{\theta})^2 - 2\ell_p\sin(\beta_p)\dot{\phi_p}(\cos(\beta_p)\dot{\phi_p} + \sin(\beta_p)\sin(\phi_p)\dot{\beta_h} + (\cos(\beta_h)\cos(\beta_p) - \sin(\beta_h)\sin(\beta_p)\cos(\phi_p))\dot{\phi_h} - \cos(\gamma)(\sin(\beta_h)\cos(\beta_p)\cos(\gamma - \phi_h) + \sin(\beta_p)(\sin(\phi_p)\sin(\gamma - \phi_h) + \cos(\beta_h)\cos(\phi_p)\cos(\gamma - \phi_h)))(\dot{\alpha} + \dot{\theta}) - \sin(\gamma)(\sin(\beta_h)\cos(\beta_p)\sin(\gamma - \phi_h) - \sin(\beta_p)(\sin(\phi_p)\cos(\gamma - \phi_h) - \cos(\beta_h)\cos(\phi_p)\sin(\gamma - \phi_h)))(\dot{\alpha} + \dot{\theta})) - 2\ell_p\ddot{\beta_p} - 2(\ell_p\cos(\phi_p) + \ell_h\cos(\beta_p))\ddot{\beta_h} - 2\sin(\phi_p)(\ell_p\sin(\beta_h) - \ell_h\sin(\beta_p)\cos(\beta_h))\ddot{\phi_h} - 2x_{luff}(\cos(\beta_h)\cos(\beta_p) - \sin(\beta_h)\sin(\beta_p)\cos(\phi_p))(\ddot{\alpha} + \ddot{\theta}) - 2\sin(\beta_p)\cos(\phi_p)(\ell_h(\dot{\beta_h} + \sin(\phi_h)(\dot{\alpha} + \dot{\theta}))^2 + \ell_h\cos(\beta_h)\dot{\gamma}(\cos(\beta_h)\dot{\phi_h} - \sin(\beta_h)\cos(\phi_h)(\dot{\alpha} + \dot{\theta})) - \dot{\ell_h}) - 2\ell_{boom}(\sin(\beta_p)\sin(\phi_p)\sin(\gamma - \phi_h) + \cos(\gamma - \phi_h)(\sin(\beta_h)\cos(\beta_p) + \sin(\beta_p)\cos(\beta_h)\cos(\phi_p)))(\sin(\gamma)\cos(\gamma)(\dot{\alpha} + \dot{\theta})^2 + \ddot{\gamma}) - 2\sin(\beta_p)\sin(\phi_p)(\ell_h(\dot{\beta_h} + \sin(\phi_h)(\dot{\alpha} + \dot{\theta}))(\sin(\beta_h)\dot{\phi_h} + \cos(\beta_h)\cos(\phi_h)(\dot{\alpha} + \dot{\theta})) - 2\dot{\ell_h}(\cos(\beta_h)\dot{\phi_h} - \sin(\beta_h)\cos(\phi_h)(\dot{\alpha} + \dot{\theta})) - \ell_h(\sin(\beta_h)\sin(\phi_h)\dot{\phi_h}(\dot{\alpha} + \dot{\theta}) - \sin(\beta_h)\dot{\beta_h}\dot{\phi_h} - \cos(\beta_h)\cos(\phi_h)\dot{\beta_h}(\dot{\alpha} + \dot{\theta}) - \sin(\beta_h)\cos(\phi_h)(\ddot{\alpha} + \ddot{\theta}))) - (\sin(\theta)(\cos(\beta_h)\cos(\beta_p) - \sin(\beta_h)\sin(\beta_p)\cos(\phi_p)) + \cos(\theta)(\sin(\gamma)(\sin(\beta_p)\sin(\phi_p)\sin(\gamma - \phi_h) + \cos(\gamma - \phi_h)(\sin(\beta_h)\cos(\beta_p) + \sin(\beta_p)\cos(\beta_h)\cos(\phi_p))) + \cos(\gamma)(\sin(\beta_p)\sin(\phi_p)\cos(\gamma - \phi_h) - \sin(\gamma - \phi_h)(\sin(\beta_h)\cos(\beta_p) + \sin(\beta_p)\cos(\beta_h)\cos(\phi_p))))((\ell_{axle} + 2x_{slew})\dot{\alpha}^2 + 2y_{slew}\ddot{\alpha}) - 2\ell_p(\sin(\beta_h)\cos(\phi_p)\dot{\phi_h}\dot{\phi_p} + \sin(\phi_p)\cos(\beta_h)\dot{\beta_h}\dot{\phi_h} + \sin(\gamma)(\dot{\alpha} + \dot{\theta})(\cos(\phi_p)\sin(\gamma - \phi_h)\dot{\phi_h} + \cos(\beta_h)\cos(\phi_p)\sin(\gamma - \phi_h)\dot{\phi_p} - \sin(\phi_p)\cos(\gamma - \phi_h)\dot{\phi_p} - \sin(\beta_h)\sin(\phi_p)\sin(\gamma - \phi_h)\dot{\beta_h} - \sin(\phi_p)\cos(\beta_h)\cos(\gamma - \phi_h)(\dot{\phi_h} - \dot{\gamma})) + ((\sin(\beta_p)\cos(\beta_h) + \sin(\beta_h)\cos(\beta_p)\cos(\phi_p))\dot{\phi_h} - \sin(\gamma)(\sin(\beta_h)\sin(\beta_p)\sin(\gamma - \phi_h) + \cos(\beta_p)(\sin(\phi_p)\cos(\gamma - \phi_h) - \cos(\beta_h)\cos(\phi_p)\sin(\gamma - \phi_h)))(\dot{\alpha} + \dot{\theta}) - \cos(\gamma)(\sin(\beta_h)\sin(\beta_p)\cos(\gamma - \phi_h) - \cos(\beta_p)(\sin(\phi_p)\sin(\gamma - \phi_h) + \cos(\beta_h)\cos(\phi_p)\cos(\gamma - \phi_h)))(\dot{\alpha} + \dot{\theta}))(\cos(\beta_p)\dot{\phi_p} + \sin(\beta_p)\sin(\phi_p)\dot{\beta_h} + (\cos(\beta_h)\cos(\beta_p) - \sin(\beta_h)\sin(\beta_p)\cos(\phi_p))\dot{\phi_h} - \cos(\gamma)(\sin(\beta_h)\cos(\beta_p)\cos(\gamma - \phi_h) + \sin(\beta_p)(\sin(\phi_p)\sin(\gamma - \phi_h) + \cos(\beta_h)\cos(\phi_p)\cos(\gamma - \phi_h)))(\dot{\alpha} + \dot{\theta}) - \sin(\gamma)(\sin(\beta_h)\cos(\beta_p)\sin(\gamma - \phi_h) - \sin(\beta_p)(\sin(\phi_p)\cos(\gamma - \phi_h) - \cos(\beta_h)\cos(\phi_p)\sin(\gamma - \phi_h)))(\dot{\alpha} + \dot{\theta})) + \sin(\gamma)(\cos(\phi_p)\cos(\gamma - \phi_h) + \sin(\phi_p)\cos(\beta_h)\sin(\gamma - \phi_h))(\ddot{\alpha} + \ddot{\theta}) - \sin(\phi_p)\dot{\beta_h}\dot{\phi_p} - \sin(\phi_h)\sin(\phi_p)\cos(\beta_h)\dot{\gamma}(\dot{\alpha} + \dot{\theta}) - \cos(\gamma)(\dot{\alpha} + \dot{\theta})(\sin(\beta_h)\sin(\phi_p)\cos(\gamma - \phi_h)\dot{\beta_h} - \sin(\phi_p)\sin(\gamma - \phi_h)\dot{\phi_p} - \cos(\phi_p)\cos(\gamma - \phi_h)\dot{\phi_h} - \cos(\beta_h)\cos(\phi_p)\cos(\gamma - \phi_h)\dot{\phi_p} - \sin(\phi_p)\cos(\beta_h)\sin(\gamma - \phi_h)(\dot{\phi_h} - \dot{\gamma})) - \cos(\gamma)(\cos(\phi_p)\sin(\gamma - \phi_h) - \sin(\phi_p)\cos(\beta_h)\cos(\gamma - \phi_h))(\ddot{\alpha} + \ddot{\theta}))) = 0$$

REFERENCES

[1] Abdel-Rahman, E. M. and Nayfeh, A. H., "Pendulation reduction in boom cranes using cable length manipulation," *Journal of Nonlinear Dynamics*, vol. 27, pp. 255–269, 2002.

[2] Abdel-Rahman, E. M., Nayfeh, A. H., and Masoud, Z. N., "Dynamics and control of cranes: A review," *Journal of Vibration and Control*, vol. 9, no. 7, pp. 863–908, 2003.

[3] Ahmad, M., Raja Ismail, R., Ramli, M., Abd Ghani, N., and Hambali, N., "Investigations of feed-forward techniques for anti-sway control of 3-d gantry crane system," in *IEEE Symposium on Industrial Electronics and Applications*, pp. 265–270, 2009.

[4] Bartolini, G., Pisano, A., and Usai, E., "Output-feedback control of container cranes: A comparative analysis," *Asian Journal of Control*, vol. 5, no. 4, pp. 578 – 593, 2003.

[5] Blackburn, D., Lawrence, J., Danielson, J., Singhose, W., Kamoi, T., and Taura, A., "Radial-motion assisted command shapers for nonlinear tower crane rotational slewing," *Control Engineering Practice*, vol. 18, pp. 523–531, May 2010.

[6] Blackburn, D. F., Singhose, W., Kitchen, J. P., Petrangenaru, V. P., Lawrence, J., Kamoi, T., and Taura, A., "Command shaping for nonlinear crane dynamics," *Journal of Vibration and Control*, vol. 16, pp. 477 – 501, April 2010.

[7] Blevins, R., *Formulas for Natural Frequency and Mode Shape*. New York, NY: Van Nostrand Reinhold Co., 1979.

[8] Bockstedte, A. and Kreuzer, E., "Crane dynamics with modulated hoisting," *Proceedings in Applied Mathematics and Mechanics*, vol. 5, pp. 83–84, 2005.

[9] Fujioka, D. D., Rauch, A., and Singhose, W. E., "Tip-over stability analysis of mobile boom cranes with double pendulum payloads," in *American Control Conference*, 2009.

[10] Fukushima, E. F., Kitamura, N., and Hirose, S., "Development of tethered autonomous mobile robot for field works," *Advanced Robotics*, vol. 15, pp. 481–496, 2001.

[11] Henry, R. J., Masoud, Z. N., Nayfeh, A. H., and Mook, D. T., "Cargo pendulation reduction on ship-mounted cranes via boom-luff angle actuation," *Journal of Vibration and Control*, vol. 7, pp. 1253–1264, 2001.

[12] Hong, K.-T. and Hong, K.-S., "Input shaping and vsc of container cranes," in *IEEE International Conference on Control Applications*, (Taipei, Taiwan), pp. 1570–1575, 2004.

[13] Huey, J. and Singhose, W., "Effect of vertical acceleration on the frequency of a pendulum: Impact on input shaping," in *IEEE Conference on Control Applications*, (Istanbul, Turkey), pp. 532–537, 2003.

[14] Khalid, A., Huey, J., Singhose, W., Lawrence, J., and Frakes, D., "Human operator performance testing using an input-shaped bridge crane," *Journal of Dynamic Systems, Measurement and Control, Transactions of the ASME*, vol. 128, no. 4, pp. 835 – 841, 2006.

[15] Kim, D. and Singhose, W., "Performance studies of human operators driving double-pendulum bridge cranes," *Control Engineering Practice*, vol. 18, pp. 567–576, 2010.

[16] Kim, D. and Singhose, W., "Human operator learning on double-pendulum bridge cranes," in *ASME International Mechanical Engineering Congress and Exposition*, (Seattle, WA), pp. 1959–1965, November 2007.

[17] Kim, D. and Singhose, W., "Manipulation with tower cranes exhibiting double-pendulum oscillations," in *Proceeding of 2007 IEEE International Conference on Robotics and Automation*, (Rome, Italy), pp. 4550 – 4555, 10-14 April 2007.

[18] LaValle, S. M., *Planning Algorithms*. Cambridge University Press, 2006.

[19] Lawrence, J. and Singhose, W., "Command shaping slewing motions for tower cranes," *ASME J. of Vibration and Acoustics*, vol. 132, pp. 011002–1–11, February 2010.

[20] Lawrence, J., Singhose, W., Weiss, R., Erb, A., and Glauser, U., "An internet-driven tower crane for dynamics and controls education," in *7th IFAC Symposium on Advances in Control Education*, (Madrid, Spain), 2006.

[21] Magee, D. P. and Book, W. J., "Filtering schilling manipulator commands to prevent flexible structure vibration," in *American Control Conference*, vol. 2, (Baltimore, MD), pp. 474–479, IEEE, 1994.

[22] Maleki, E., Elahmadi, Z., and Singhose, W., "Operator performance studies on a small-scale mobile boom crane," in *The 17th International Congress on Sound and Vibration*, (Cairo, Egypt), 2010.

[23] Maleki, E. and Singhose, W., "Dynamics and control of a small-scale boom crane," *Submitted to the Journal of Computational and Nonlinear Dynamics*, 2010.

[24] Maleki, E. and Singhose, W., "Dynamics and zero vibration input shaping control of a small-scale boom crane," in *American Control Conference*, (Baltimore, MD), 2010.

[25] Maleki, E., Singhose, W., and Srinivasan, S., "Positioning and control of boom crane luffing with double-pendulum payloads," in *IEEE Conference on Control Applications*, (Yokohama, Japan), 2010.

[26] Maleki, E., Singhose, W., and Vaughan, J., "Initial experiments with a small-scale mobile boom crane," in *Proceedings of the IASTED Conference on Robotics and Applications*, (Cambridge, MA), pp. 664–059, 2009.

[27] Manning, R., Clement, J., Kim, D., and Singhose, W., "Dynamics and control of bridge cranes transporting distributed-mass payloads," *Journal of Dynamic Systems, Measurement, and Control*, vol. 132, no. 014505, 2010.

[28] Masoud, Z., Nayfeh, A., Henry, R., and Mook, D., "Cargo pendulation reduction on ship-mounted cranes via boom-luff and slew angles actuation," in *Structures, Structural Dynamics, and Materials Conference*, (Atlanta, GA), pp. AIAA–2000–1543, 2000.

[29] Mitiguy, P. and Reckdahl, K., *Autolev Tutorial*. OnLine Dynamics, Inc., Sunnyvale, CA, 2005.

[30] Neupert, J., Arnold, E., Schneider, K., and Sawodny, O., "Tracking and anti-sway control for boom cranes," *Control Engineering Practice*, vol. 18, pp. 31–44, 2010.

[31] Omar, H. M. and Nayfeh, A. H., "A simple adaptive feedback controller for tower cranes," in *ASME Design Engineering Technical Conferences*, (Pittsburgh, PA), pp. DETC2001/VIB–21606, 2001.

[32] Parker, G. G., Groom, K., Hurtado, J. E., Feddema, J., Robinett, R. D., and Leban, F., "Experimental verification of a command shaping boom crane control system," in *American Control Conference*, pp. 86–90, 1999.

[33] Rauch, A. and Singhose, W., "Stability analysis of mobile boom crane," in *International Conference on Motion and Vibration Control*, 2008.

[34] Rhim, S. and Book, W. J., "Adaptive command shaping using adaptive filter approach in time domain," in *American Control Conference*, (San Diego, CA), pp. 81–85, 1999.

[35] Sawodny, O., Aschemann, H., Kumpel, J., Tarin, C., and Schneider, K., "Anti-sway control for boom cranes," in *American Control Conference*, vol. 1, (Anchorage, AK, United states), pp. 244 – 249, 2002.

[36] Sawodny, O., Aschemann, H., and Lahres, S., "An automated gantry crane as a large workspace robot," *Control Engineering Practice*, vol. 10, no. 12, pp. 1323 – 1338, 2002.

[37] Singer, N., Singhose, W., and Kriikku, E., "An input shaping controller enabling cranes to move without sway," in *ANS 7th Topical Meeting on Robotics and Remote Systems*, vol. 1, (Augusta, GA), pp. 225–31, 1997.

[38] Singer, N. C. and Seering, W. P., "Preshaping command inputs to reduce system vibration," *J. of Dynamic Sys., Measurement, and Control*, vol. 112, no. March, pp. 76–82, 1990.

[39] Singhose, W., "Command shaping for flexible systems: A review of the first 50 years," *International Journal of Precision Engineering and Manufacturing*, vol. 10, no. 4, pp. 153–168, 2009.

[40] Singhose, W., Kim, D., and Kenison, M., "Input shaping control of double-pendulum bridge crane oscillations," *Journal of Dynamic Systems, Measurement, and Control*, vol. 130, no. 034504, 2008.

[41] Singhose, W., Porter, L., Kenison, M., and Kriikku, E., "Effects of hoisting on the input shaping control of gantry cranes," *Control Engineering Practice*, vol. 8, no. 10, pp. 1159–1165, 2000.

[42] Singhose, W., Seering, W., and Singer, N., "Residual vibration reduction using vector diagrams to generate shaped inputs," *ASME J. of Mechanical Design*, vol. 116, no. June, pp. 654–659, 1994.

[43] Singhose, W., Seering, W., and Singer, N., "Input shaping for vibration reduction with specified insensitivity to modeling errors," in *Japan-USA Sym. on Flexible Automation*, vol. 1, (Boston, MA), pp. 307–13, 1996.

[44] Smith, O. J. M., "Posicast control of damped oscillatory systems," *Proceedings of the IRE*, vol. 45, no. 9, pp. 1249–1255, 1957.

[45] Sorensen, K., Singhose, W., and Dickerson, S., "A controller enabling precise positioning and sway reduction in bridge and gantry cranes," *Control Engineering Practice*, vol. 15, pp. 825–837, July 2007.

[46] Souissi, R. and Koivo, A. J., "Modeling and control of a rotary crane for swing-free transport of payloads," in *IEEE Conference on Control Applications*, (Dayton, OH), pp. 782–787, 1992.

[47] Starr, G. P., "Swing-free transport of suspended objects with a path-controlled robot manipulator.," *Journal of Dynamic Systems, Measurement and Control*, vol. 107, no. 1, pp. 97 – 100, 1985.

[48] Tzes, A. and Yurkovich, S., "An adaptive input shaping control scheme for vibration suppression in slewing flexible structures," *IEEE Transactions on Control Systems Technology*, vol. 1, no. June, pp. 114–121, 1993.

[49] Valera, J., Irigoyen, E., Gomez-Garay, V., and Artaza, F., "Application of neuro-genetic techniques in solving industrial crane kinematic control problem," in *IEEE International Conference on Mechatronics*, (Malaga, Spain), p. 10.1109/ICMECH.2009.4957204, 2009.

[50] Vaughan, J., Kim, D., and Singhose, W., "Control of tower cranes with double-pendulum dynamics," *Accepted to IEEE Trans. on Control Systems Technology*, 2010.